

DUAL SCALE ROUGHNESS DRIVEN PERFECTLY  
HYDROPHOBIC SURFACES PREPARED BY  
ELECTROSPRAYING A POLYMER IN GOOD  
SOLVENT-POOR SOLVENT SYSTEMS

by  
EREN ŞİMŞEK

Submitted to the Graduate School of Engineering and Natural Sciences  
in partial fulfillment of  
the requirements for the degree of  
Doctor of Philosophy

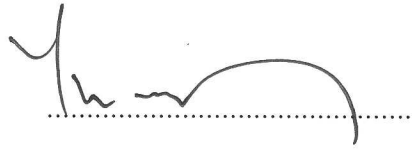
Sabancı University

July 2012

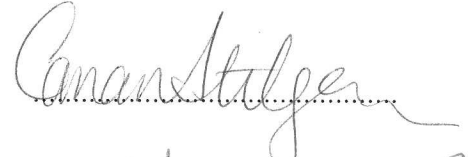
DUAL SCALE ROUGHNESS DRIVEN PERFECTLY HYDROPHOBIC SURFACES  
PREPARED BY ELECTROSPRAYING A POLYMER IN GOOD SOLVENT-POOR  
SOLVENT SYSTEMS

APPROVED BY

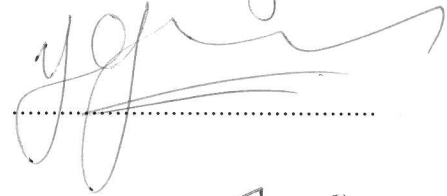
Prof. Dr. YUSUF Z. MENCELOĞLU  
(Thesis Supervisor)



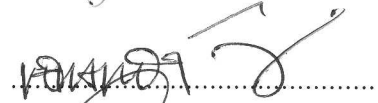
Prof. Dr. CANAN ATILGAN



Prof. Dr. YAŞAR GÜRBÜZ



Assoc. Prof. Dr. MEHMET YILDIZ



Assoc. Prof. Dr. MUSTAFA M. DEMİR



DATE OF APPROVAL: ...20.07.2012...

babama...

©Eren Şimşek 2012  
All Rights Reserved



## Acknowledgments

The groundwork of this dissertation dates back to my undergraduate years; however, the printed pages hold far more than the culmination of years of study. These pages also reflect the relationships with many generous and inspiring people I have met since I started research as a part of Polymer Synthesis undergraduate course. The list is long, but I cherish each contribution to my development as a scientist.

It is with immense gratitude that I acknowledge the neverending support and help of my thesis advisor Dr. Yusuf Z. Mencilođlu, with whom I have been working for about ten years with great honor and pleasure. My excitement towards scientific work is only a minor reflection of his constant conveying a spirit of adventure in regard to research. The intimacy he showed has been the factor that made it all easy. I always wonder how much more, professionally and personally, I could gain from a person in my life. I will always feel indebted to him.

I would like to thank my professors Dr. Ali Rana Atılgan, Dr. Canan Atılgan, Dr. Mehmet Ali Gülgün, Dr. Cleve Ow-Yang, Dr. Melih Papila, Dr. Alpay Taralp and Dr. Mehmet Yıldız for conveying their priceless knowledge and experience during the courses and collaborative works. I also acknowledge Dr. Kazım Acatay who pioneered the superhydrophobicity subject in Sabancı University and drew me into the subject as his co-worker.

I owe much to my dearest friends, Özge Batu, Dr. Emre Heves and Dr. Deniz Turgut, with whom I have wonderful memories of joyful time together during my Ph.D. education. My colleagues Mustafa Baysal, Kaan Bilge, Ođuzhan Ođuz, Erim Ülkümen and Melike M. Yıldızhan have tremendous amount of contribution to this thesis. I feel lucky to have friends with such beautiful personalities. In addition to our enjoyable friendship, I acknowledge Elif Ö. Yenigün and Dr. İbrahim İnanç for their contributions in the computational and experimental parts, respectively. I also thank all other MAT grad. colleagues for their overall generous aid and respectful attitude towards me.

And thanks to my family, for their support, trust and understanding.

DUAL SCALE ROUGHNESS DRIVEN PERFECTLY HYDROPHOBIC SURFACES  
PREPARED BY ELECTROSPRAYING A POLYMER IN GOOD SOLVENT-POOR  
SOLVENT SYSTEMS

EREN ŞİMŞEK

MAT, Ph.D. Thesis, 2012

Thesis Supervisor: Yusuf Z. Menceloğlu

**Keywords:** Superhydrophobic, Lotus effect, contact angle hysteresis, phase separation, dissipative particle dynamics

## Abstract

A facile method to produce perfectly hydrophobic surfaces (advancing and receding water contact angles both  $180^\circ$ ) via electrospaying is demonstrated. When a copolymer of styrene and a perfluoroalkyl acrylate monomer was electrospayed in good solvents, surfaces composed of micron size beads were formed and fairly low threshold sliding angles could be achieved. Addition of high boiling point poor solvents to the solutions resulted nanoscale roughness on the beads. However, even the nanoscale roughness dominated topographies achieved by this method exhibited contact angle hysteresis although deducted to be relatively small. On the other hand, when the electrospaying process parameters were set such that micron size hills of nanoscopically rough beads were formed,  $0^\circ$  sliding angles, implying zero contact angle hysteresis, were measured. Videos of droplets recorded and the adhesive forces measured during a contact and release experiment revealed that these dual scale rough surfaces were indeed perfectly hydrophobic. Application of the method with other binary good solvent-poor solvent systems also resulted in perfect hydrophobicity. Overall results showed how the differences in surface topology affected the wettability of surfaces within a very narrow range between perfect and extreme hydrophobicity (advancing and receding water contact angles both close to  $180^\circ$ ).

In order to interpret the formation of different surface topographies achieved by electrospraying the corresponding copolymer in good, poor and binary solvent systems, dissipative particle dynamics simulations and dynamic light scattering analysis were performed. Simulations of the polymer in good solvent revealed relatively homogeneous solutions at all concentrations, whereas phase separation was observed in the poor solvent even at low concentrations. Light scattering experiments yielded useful information about the hydrodynamics of the real chains in the corresponding solvent systems in the dilute regime. It was found that the polymer forms stable aggregates in the poor solvent due to weak interaction with the solvent. Overall results indicated that formation of smooth bead morphologies is due to homogeneous drying of the polymer from the good solvent. On the other hand, polymer aggregates lead to nanoscopic features in the regions where the solidification occurs mainly in the poor solvent environment.

İYİ ÇÖZÜCÜ-ZAYIF ÇÖZÜCÜ KARIŞIMI İÇERİSİNDE ÇÖZÜNMÜŞ  
POLİMERİN ELEKTROSPREYLENMESİ YOLUYLA ELDE EDİLMİŞ, ÇİFTE  
SEVİYE PÜRÜZLÜLÜĞE SAHİP MÜKEMMEL HİDROFOBİKLİKTE YÜZEYLER

EREN ŞİMŞEK

MAT, Doktora Tezi, 2012

Tez Danışmanı: Yuzuf Z. Menceloğlu

**Anahtar Kelimeler:** Süperhidrofobik, Lotus etkisi, temas açısı histeresisi, faz ayrımı, dağıtıcı parçacık dinamiği

## Özet

Bu çalışmada, mükemmel hidrofobikliğe (ilerleyen ve gerileyen su temas açılarının her ikisi de  $180^\circ$ ) sahip yüzeylerin elektrospreyleme yoluyla üretilmesine dair kolay bir yöntem takdim edilmiştir. Bir stiren ve perfloroalkil akrilat kopolimerinin iyi çözücü içerisinde elektrospreylemesiyle, mikrometre seviyesinde büyüklüğe sahip polimer boncukların oluşturduğu yüzeyler elde edilmiş, yüzeylerin oldukça küçük eşik su kayma açlarına sahip olduğu belirlenmiştir. Çözeltilere zayıf çözücü eklenmesi, polimer boncuklar üzerinde nanometre seviyesinde pürüz oluşumu ile sonuçlanmıştır. Ancak, üretilen çeşitli yüzeylerden, baskın olarak nanometre seviyesinde pürüzlülüğe sahip olanların dahi, çok küçük olduğu çıkarımı yapılsa da, temas açısı histeresisine sahip oldukları gözlemlenmiştir. Diğer yandan, elektrospreyleme işlem parametrelerinin ayarlanmasıyla, ‘yüzeyleri nanoskopik pürüz ihtiva eden mikron boncuk tepelikleri’ şeklinde elde edilen yüzeylerde  $0^\circ$  eşik kayma açısı ölçülmüştür ki bu sonuç yüzeylerde histeresis değerinin de sıfır olduğunu ima etmektedir. Su damlaları ve yüzeyler arasında gerçekleştirilen temas ettirme-ayırma işlemi videoları, ve damla-yüzey arası yapışma kuvveti ölçümleri, bu çifte seviye pürüze sahip yüzeylerin aslında mükemmel hidrofobiklikte olduklarını göstermiştir. Bu yöntemin, aynı polimer ile diğer iyi solvent-zayıf solvent sistemlerine uygulanması yine mükemmel hidrofobiklik ile sonuçlanmıştır. Sonuçlar genel çerçevede,

topografyadaki deęişikliklerin yüzeylerin ıslanabilirliğine mükemmel ve aşırı hidrofobiklik (ilerleyen ve gerileyen temas açıları  $180^\circ$ 'ye yakın) gibi dar bir aralıkta nasıl etki edebildiğine dair önemli bilgiler açığa çıkarmıştır.

Kopolimerin iyi, zayıf ve karışım solvent sistemlerinde elektrospreylenmesi yoluyla elde edilen yüzey topografyalarındaki farklılıkları açıklamak için, dağıtıcı parçacık dinamięi simülasyonları ve dinamik ışık saçılımı analizleri gerçekleştirilmiştir. İyi çözücüde gerçekleştirilen simülasyonlarda solusyonların tüm konsantrasyonlarda görece homojen olduğu, ancak polimerin zayıf çözücü içerisinde düşük konsantrasyonlarda dahi faz ayırımına gittięi görülmüştür. Işık saçılımı deneyleri, gerçek zincirlerin ilgili solvent sistemlerinde seyreltik rejimdeki hidrodinamikleri ile ilgili faydalı bilgiler vermiştir. Polimerin zayıf çözücü içerisinde stabil birikintiler oluşturduğuna dair bulgular elde edilmiştir. Bütün halinde sonuçlar vurgulamıştır ki düzgün yüzeyli boncukların oluşumu polimerin iyi çözücünden homojen kuruması sayesinde gerçekleşmektedir. Diğer taraftan, polimer zayıf çözücü içerisinde faz ayırımına gitmekte, düzensiz kuruma sonucu nanoskopik yapıların oluşumuna sebebiyet vermektedir.

# Table of Contents

<b>Acknowledgments</b>	<b>v</b>
<b>Abstract</b>	<b>vi</b>
<b>Özet</b>	<b>viii</b>
<b>1 Introduction</b>	<b>1</b>
1.1 The Origin of Interfacial Tension . . . . .	1
1.2 Fluorinated Polymers as Hydrophobic Materials . . . . .	3
1.3 Introduction to Wettability . . . . .	4
1.4 The Famous Wenzel and Cassie-Baxter Equations are Indeed Wrong . .	8
1.5 Three Phase Contact Lines: All Wetting Phenomena is Indeed a One Dimensional Issue . . . . .	9
1.6 Measurement of Dynamic Contact Angles . . . . .	12
1.7 On the Delusion Created by High Static Contact Angles . . . . .	13
1.8 Dual Length Scales of Topography is the Route to Zero Hysteresis . . .	14
1.9 New Definitions Related to Wettability . . . . .	16
1.10 Perfectly Hydrophobic Surfaces . . . . .	17
1.11 Introduction to Electrospraying . . . . .	19
1.12 Dissipative Particle Dynamics . . . . .	21
1.13 The Scope of the Study . . . . .	22
<b>2 Materials and Methods</b>	<b>25</b>
2.1 Materials . . . . .	25
2.2 Synthesis and Bulk Characterization of Poly(St-co-Perfluoroalkyl ethy- lacrylate) . . . . .	25
2.3 Electrospraying of the Copolymer Solutions . . . . .	26
2.4 Characterization of Surface Topographies . . . . .	26
2.5 Wettability Analysis . . . . .	26
2.6 Particle Size Measurements . . . . .	27
2.7 Atomistic Simulations for DPD Parametrization . . . . .	27
2.8 Parametrization of Interactions for the Coarse-Grained DPD Methodology	28
2.9 DPD Simulations . . . . .	29

<b>3</b>	<b>Results and Discussion</b>	<b>30</b>
3.1	Bulk and Surface Properties of the Copolymer . . . . .	30
3.2	A Foreword on the Wettability Measurements . . . . .	31
3.3	Electrospraying the Copolymer in a Good Solvent . . . . .	31
3.4	Electrospraying the Copolymer in a Poor Solvent . . . . .	32
3.5	Electrospraying the Copolymer in a Binary Good Solvent-Poor Solvent System . . . . .	33
3.6	The Route to Zero Hysteresis . . . . .	39
3.7	Contact and Release Experiment: Proof of Perfect Hydrophobicity . . .	42
3.8	Some Remarks on the Described Method . . . . .	49
3.9	Computational Analysis . . . . .	50
<b>4</b>	<b>Summary and Conclusions</b>	<b>58</b>
<b>A</b>	<b>Appendix</b>	<b>60</b>
A.1	Contact and Release Experiments Performed with Other Surfaces . . .	60
A.2	Examples of Surfaces from Other Polymers or Systems . . . . .	64
	 <b>Bibliography</b>	 <b>67</b>

## List of Figures

1.1	The difference in the net forces acting on molecules at the bulk and surface.	2
1.2	Three idealized states of wetting. . . . .	5
1.3	Surfaces that exhibit (a) a rough spot in a smooth field, and (b) a smooth spot in a rough field. Images labelled as I and II are the depictions of the surfaces and the wettability experiments, respectively, shown in frames labelled as III. . . . .	9
1.4	Physical events that occur during movement of a droplet. (a) Advancing and receding contact angles of a droplet moving on a tilted surface. Movement of three phase contact line during receding (b), and advancing (c). . . . .	10
1.5	Pictorial representations of surfaces with three different roughness topologies. The darker lines describe possible three-phase contact lines for a drop of water in contact with these surfaces: (a) A screen on which a fairly continuous contact line can form, (b) separated ridges on which a discontinuous but substantial contact line can form, and (c) separated posts on which a very discontinuous contact line must form. . . . .	11
1.6	Pictorial representations of (a) advancing contact angle, and (b) receding contact angle measurement. Numbers indicate the order of experimental steps. . . . .	12
1.7	Dynamics of static droplet formation. . . . .	13
1.8	(a) SEM micrograph of the <i>Nelumbo nucifera</i> (Lotus) leaf surface, (b) water droplets on the Lotus leaves, and (c) connection between roughening and self-cleaning. . . . .	14



1.9	(a) Scanning electron microscopy (SEM) image of a surface containing staggered 4 x 8 x 40 $\mu\text{m}$ rhombus posts, (b) SEM image of the surface shown in panel a after introducing nano scale roughness, and (c) receding event on micron (top) and dual scale (bottom) surface. . . . .	15
1.10	(a) Frames of a videotape of a droplet (8.5 $\mu\text{L}$ ) of water being placed onto a thin film of Teflon ( $\approx 3.7 \mu\text{m}$ thick), and (b) differences between shear and tensile hydrophobicity. . . . .	17
1.11	(a) First ever reported perfectly hydrophobic surface, and (b) SEM micrograph of the compressed sample of tetrafluoroethylene oligomer. . .	18
1.12	SEM micrograph of the hexagonal nanoneedle array. . . . .	19
1.13	(a) Schematic representation of electro spraying, and (b) high-speed photographs of electro spraying process where jet breaks up into separate droplets. . . . .	19
1.14	Physical representation of three solution regimes. . . . .	20
1.15	Various bead shapes that may occur during electro spraying. . . . .	21
2.1	Synthesis of Poly(St- <i>co</i> -Perfluoroalkyl ethylacrylate). . . . .	26
2.2	Partitioning of the beads for coarse-grained simulations. . . . .	28
3.1	Typical SEM images of the electro sprayed surfaces from solutions having (a) 7 wt%, (b) 1 wt%, and (c) 0.4 wt% polymer concentration in THF. Applied voltage and solution feed rate were 8 kV and 2 $\mu\text{L}/\text{min}$ for all samples, respectively. (d) Sliding angle vs. polymer concentration in THF for a 10 $\mu\text{L}$ water droplet. . . . .	33
3.2	Typical SEM images of the electro sprayed surfaces from solutions having 0.15 wt% polymer in DMF. . . . .	34
3.3	Depictions of different roughness scales related to wettability. (a) Micron scale roughness, (b) nano scale roughness, and (c) dual scale roughness. . . . .	35

3.4	Typical SEM images of the electrosprayed surfaces from 1 wt% polymer solutions in 75/25 (wt/wt) THF/DMF mixture. (a) 8 kV and 2 $\mu\text{L}/\text{min}$ , (b) 15 kV and 15 $\mu\text{L}/\text{min}$ , and (c) 15 kV and 15 $\mu\text{L}/\text{min}$ applied voltage and solution feed rate, respectively. Coating time is shorter (30 seconds) for (c). . . . .	36
3.5	High magnification images of the flower-like structures shown in (a) Fig. 3.1(c), and (b) Fig. 3.4(a). . . . .	37
3.6	Schematic demonstration of bead formation during electrospraying of polymer solutions at different conditions. Light and dark regions represent solvent and polymer rich phases, respectively. . . . .	37
3.7	Typical SEM images of the electrosprayed surfaces from 1 wt% polymer solutions in (a) Chloroform (8 kV applied voltage and 2 $\mu\text{L}/\text{min}$ solution feed rate), and (b) 75/25 (wt/wt) chloroform/DMF mixture (15 kV applied voltage, 15 $\mu\text{L}/\text{min}$ solution feed rate, 30 seconds coating time). . . . .	40
3.8	Typical SEM images of the electrosprayed surfaces from 1 wt% polymer solutions in (a) 75/25, and (b) 50/50 (wt/wt) THF/DMSO mixture. Process parameters are 8 kV applied voltage, 2 $\mu\text{L}/\text{min}$ solution feed rate and 30 seconds coating time for both samples. . . . .	41
3.9	Selected frames of the contact and release experiment performed with the surface having nanoscale roughness dominated topography shown in Fig. 3.4(b). . . . .	43
3.10	Selected frames of the contact and release experiment performed with the surface having dual scale rough topography shown in Fig. 3.4(c). . . . .	44
3.11	Selected frames of the contact and release experiment performed with the surface having micron scale roughness dominated topography shown in Fig. 3.8(a). . . . .	45
3.12	Selected frames of the contact and release experiment performed with the surface having micron scale roughness dominated topography shown in Fig. 3.8(b). . . . .	46

3.13	Pictorial presentation of the experiment performed to measure the adhesive forces during the release of a droplet from a superhydrophobic surface. (a) A previously pressed droplet is being released, (b) adhesion (if exist) causes deformation of the droplet from its thermodynamical shape, and (c) droplet and the surface are separated. . . . .	48
3.14	Force required to separate a superhydrophobic surface from a droplet for samples having micro, nano and dual scale roughness during the experiment depicted in Fig. 3.13. 0 mm distance refers to the position when the droplet and the surface were in contact for the first time. Negative and positive distances correspond to raising and lowering the lower plate from this 0 displacement, respectively. . . . .	48
3.15	Partitioning of the beads for coarse-grained simulations. Replication of Fig. 2.2. . . . .	50
3.16	Mesoscopic morphologies of the copolymer at various concentrations in (a) THF, and (b) DMF. . . . .	53
3.17	Typical SEM images of the electrospayed copolymer from (a) 1 wt% solution in THF (the surface shown in Fig. 3.1(b)), (b) 1 wt% solution in 75/25 (wt/wt) THF/DMF mixture (electrospayed at 8 kV and 2 $\mu$ L/min, the surface shown in Fig. 3.4(a)), and (c) 0.15 wt% solution in DMF. . . . .	54
3.18	DLS analysis 0.02 wt% polymer in THF, DMF, DMF after passing the solution from a filter having 200 nm diameter pores, and THF/DMF 50/50.	56
3.19	DLS analysis 0.02 wt% polymer in DMF after passing the solution from a filter having 200 nm diameter pores, methanol, DMF after evaporation of THF from THF/DMF 50/50 (DMF*), and 0.04 wt% in DMF after evaporation of THF from THF/DMF (DMF**). . . . .	57
A.1	Selected frames of the contact and release experiment performed with the surface electrospayed from 1 wt% copolymer in THF. The SEM micrograph is the replication of Fig. 3.1(b). . . . .	61

A.2	Selected frames of the contact and release experiment performed with the surface electrospayed from 1 wt% copolymer in THF. The SEM micrograph is the replication of Fig. 3.1(a). . . . .	62
A.3	Selected frames of the contact and release experiment performed with the surface electrospayed from 1 wt% copolymer in 75/25 (w/w) THF/DMF at 8 kV applied voltage and 2 $\mu\text{L}/\text{min}$ solution feed rate. The SEM micrograph is the replication of Fig. 3.4(a). . . . .	63
A.4	Typical SEM image of the electrospayed surfaces from 2 wt% poly(st-co-PFA) solutions in 75/25 (wt/wt) THF/DMF mixture (22 kV applied voltage and 25 $\mu\text{L}/\text{min}$ solution feed rate). . . . .	65
A.5	Typical SEM image of the electrospayed surfaces from 2 wt% poly(MMA-co-PFA) solutions in 50/50 (wt/wt) THF/DMF mixture (8 kV applied voltage and 2 $\mu\text{L}/\text{min}$ solution feed rate). . . . .	65
A.6	Typical SEM image of the electrospayed surfaces from 2 wt% poly(MMA-co-PFA) solutions in 50/50 (wt/wt) THF/DMF mixture (15 kV applied voltage and 15 $\mu\text{L}/\text{min}$ solution feed rate). . . . .	66
A.7	Typical SEM image of the electrospayed surfaces from 1.5 wt% poly(st-co-PFA) solutions in 50/50 (wt/wt) THF/NMP mixture (8 kV applied voltage and 0.5 $\mu\text{L}/\text{min}$ solution feed rate). . . . .	66

## List of Tables

3.1	Various parameters of the liquids used for electrospraying. . . . .	31
3.2	Solubility parameters, $\delta$ ( $(cal/cm^3)^{1/2}$ ), and molar volume $V_m$ ( $cm^3/mol$ ) of the beads. . . . .	51
3.3	Flory-Huggins interaction parameters, $\chi_{ij}$ , and DPD interaction parameters, $a_{ij}$ . . . . .	51

# Chapter 1

## Introduction

### 1.1 The Origin of Interfacial Tension

An interface is defined as the ‘boundary between immiscible phases’ [1]. The two immiscible phases forming the interface might be solid-solid, solid-liquid, solid-gas, liquid-liquid, and liquid-gas. Gas-gas interfaces do not exist since gases mix. The interface between a gas and a solid or liquid is commonly termed as a ‘surface’. The main difference between the surface and bulk of a material is that the molecules forming the surface have unbalanced cohesive forces which pull them towards the bulk (Fig. 1.1) as Thomas Young states in his famous article, *An Essay on the Cohesion of Fluids*, which was published in 1805 [2]:

*“We may suppose the particles of liquids, and probably those of solids also, to possess that power of repulsion, which has been demonstratively shown by NEWTON to exist in aeriform fluids, and which varies in the simple inverse ratio of the distance of the particles from each other. In airs and vapours this force appears to act uncontrolled; but in liquids, it is overcome by cohesive force, while the particles still retain a power of moving freely in all directions; and in solids the same cohesion is accompanied by a stronger or weaker resistance to all lateral motion, which is perfectly independent of the cohesive force, and which must be cautiously distinguished from it. It is simplest to suppose the force of cohesion nearly or perfectly constant in its magnitude, throughout the minute distance to which it extends, and owing*

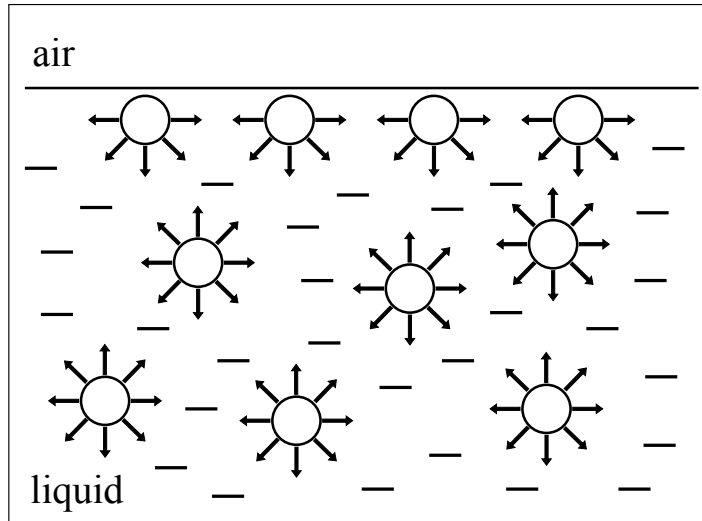


Figure 1.1: The difference in the net forces acting on molecules at the bulk and surface.

*its apparent diversity to the contrary action of the repulsive force, which varies with the distance. Now in the internal parts of a liquid these forces hold each other in a perfect equilibrium, the particles being brought so near that the repulsion becomes precisely equal to the cohesive force that urges them together; but whenever there is a curved or angular surface, it may be found by collecting the actions of the different particles, that the cohesion must necessarily prevail over the repulsion, and must urge the superficial parts inwards with a force proportionate to the curvature, and thus produce the effect of a uniform tension of the surface.”*

Young, who died at the age of 55 in 1829, obviously did not know about molecules or bonds, surface free energy or thermodynamics, but he had the wisdom to envisage molecular structure as *particles* and *forces*, and resultant unbalanced, uniform forces on the surface as *surface tension*. Surface tension is a net force per unit length. Surface energy, on the other hand, is a quantity of excess energy that emerge upon creation of a surface (basically, work must be done to break the intermolecular bonds and create a surface), and defined in terms of energy per unit area. For homogenous, uniform surfaces, surface tension and energy fundamentally become same from a scalar perspective, although their physical meanings remain different.

The strength of intermolecular forces determines the magnitude of surface tension. In general, materials of polar molecules tend to have high surface tension, whereas non-polar molecules yield relatively low surface tensions. For instance, water can form two hydrogen bonds per molecule, which has made the liquid a benchmark high surface tension material. Accordingly, terms hydrophilic and hydrophobic have been (loosely) used to refer to materials having relatively high and low surface tension, respectively. Polytetrafluoroethylene (Teflon as the trademark registered by DuPont Co. in 1945) has become a benchmark low energy, hydrophobic surface due to the non-polar nature of the  $-\text{CF}_2$  molecules forming the polymer backbone.

## 1.2 Fluorinated Polymers as Hydrophobic Materials

Fluorinated materials have attracted considerable attention due to their low surface energy, corrosion resistance, thermal stability, low refractive index, and more. Particularly, fluorocarbons have found numerous applications as hydrophobic coatings for low humidity and adhesion applications due to the non-polar nature of the  $-\text{CF}_x$  groups. Homopolymers composed of perfluorinated chains or pendant groups are preferred under conditions exhibiting high temperatures or rigorous chemicals but their low or non-solubility in common solvents limit their use in many applications. However, for surface applications focusing on hydrophobicity, copolymers of fluorinated and conventional monomers can be effectively employed since it is well understood that perfluoroalkylated monomers decrease the wettability of surfaces due to the low surface tension of the fluorinated groups. Particularly for the copolymers of perfluorinated monomers, the outermost layer of the polymers differs remarkably from the bulk composition due to the surface segregation of fluorinated segments, which yields relatively high advancing water contact angles. In addition, self assembly of fluorinated block copolymers in various environments have been successfully utilized to fabricate nano-structures having a wide range of morphologies which have found applications in emerging technologies such as nano-optics, nano-electronics, nano-biotechnology, and etc. [3–6].

All surfaces are energetically unfavorable since they have a positive energy of for-



mation. Liquids tend to reduce the amount of their surface area by forming spherical shapes in order to decrease the total surface energy (sphere has the lowest surface area per volume). Solids, on the other hand, usually perform the action of ‘surface energy minimizing’ by exposing low surface energy segments. Accordingly, the surface and bulk composition can differ remarkably. For instance, it has been shown in many reports that homopolymers of fluorinated acrylates and siloxanes, or their copolymers with conventional monomers can show very low surface energy since the fluorinated groups segregate on the outermost surface [7–18]. The contribution of fluorinated groups to surface energy decreases in the order of  $-\text{CF}_2\text{H}$ ,  $-\text{CF}_2-$ , and  $-\text{CF}_3$ , respectively [19,20]. Particularly for the copolymers of perfluorinated monomers, the outermost layer of the polymers differs remarkably from the bulk composition, and is covered with large concentrations of the fluorinated segment.

Liquid crystalline ordering of perfluoroalkyl side chains in the block and graft copolymers enhances both the density of fluorinated groups at the interface [10–12,18,21] and resistance to surface reorganizations due to environment change [9,18,22]. Except for several studies [10,12,13], random copolymers of perfluorinated acrylates have been of less interest in the wettability literature. This might be due to the susceptibility of those surfaces to reorientation of polar groups towards the liquid phase in order to decrease the interfacial energy when in contact with water.

### 1.3 Introduction to Wettability

In his famous essay Young continues:

*“We may therefore inquire into the conditions of equilibrium of the three forces acting on the angular particles, one in the direction of the surface of the fluid only, a second in that of the common surface of the solid and fluid, and the third in that of, the exposed surface of the solid. Now supposing the angle of the fluid to be obtuse, the whole superficial cohesion of the fluid being represented by the radius, the part which acts in the direction of the surface of the solid will be proportional to the cosine of the inclination; and*

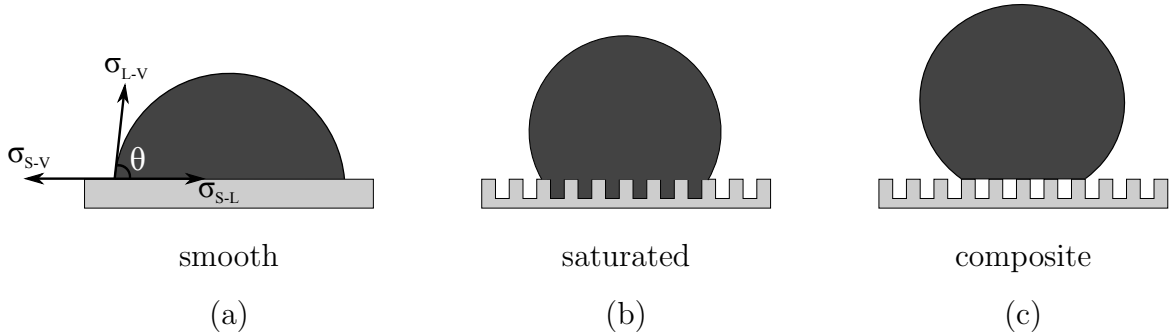


Figure 1.2: Three idealized states of wetting.

*this force, added to the force of the solid, will be equal to the force of the common surface of the solid and fluid, or to the differences of their forces...*

Although never wrote an equation, Young's statements regarding cohesion of fluids leads to the formulation of contact angle,  $\theta$ , of a liquid on a surface as [23]:

$$\cos \theta = \frac{F_{SV} - F_{SL}}{F_{LV}} \quad (1.1)$$

where  $F_{SV}$ ,  $F_{SL}$ , and  $F_{LV}$  are the forces pertained to the cohesion of superficial particles at the solid-vapor, solid-liquid, and liquid-vapor interfaces, respectively. This equation is the result of a simple force balance that must exist on a three phase contact line (the imaginary line that forms the boundary between the solid, liquid, and vapor phases) at equilibrium. On a chemically homogeneous, smooth surface, these forces would be equal to the interfacial tensions ( $\sigma$ ) as depicted in Fig. 1.2(a). However, roughness affects contact angles. Thus, for the wettability of rough solid surfaces, two models were proposed:

- A Wenzel [24] state characterized by penetration of liquid into the grooves completely and formation of a continuous solid-liquid interface: A saturated surface (Fig. 1.2(b))
- A Cassie-Baxter [25] state where the liquid sits on the protrusions and trapped air between them: A composite surface (Fig. 1.2(c))

Wenzel, while discussing the wettability of saturated rough surfaces, indicates that [24]:

*“We must, then, recognize a distinction between the total or “actual surface” of an interface and what might be called its superficial or “geometric surface”; the latter is the surface as measured in the plane of the interface. Where perfect smoothness is an acceptable assumption, as at liquid-liquid or liquid-gas interfaces, actual surface and geometric surface are identical, but at the surface of any real solid the actual surface will be greater than the geometric surface because of surface roughness. This surface ratio will be here termed the “roughness factor” and designated by  $r$ :*

$$r = \text{roughness factor} = \frac{\text{actual surface}}{\text{geometric surface}} \quad (1.2)$$

*By definition, surface tensions, like specific energy values, are related to one unit of actual surface. But when water spreads over the surface of a real solid, the forces that oppose each other along a given length of the advancing periphery of the wetted area are proportional in magnitude, not to the surface tensions of the respective interfaces but to their total energies per unit of geometric surface. This must be true if surface tensions themselves are characteristic properties, unaltered by surface roughness. For if a solid,  $M$ , of surface tensions  $x$  and water-solid interfacial tension  $y$  presents a surface so rough that its actual surface per unit geometric surface is doubled, then its energy content per unit geometric surface must also be doubled. That surface can then be no different in wetting characteristics from the smooth surface of a solid,  $N$ , of surface tension  $2x$  and water-solid interfacial tension  $2y$ . In the latter case the surface forces in vector relation with the surface tension of the liquid at the periphery of the wetted area are equal to  $2x$  and  $2y$ ; and so they must be also for the roughened surface of solid  $M$ .”*

As it is clear from his statements, Wenzel explicitly proposes that *apparent contact angle* on a saturated surface is a function of Young’s angle such that:

$$\cos\theta_{\text{rough}} = r \frac{\gamma_{SV} - \gamma_{SL}}{\gamma_{LV}} = r \cos\theta_{\text{smooth}} \quad (1.3)$$

with a significant difference that replaces ‘force’ in Young’s expressions (Eq. (1.1)) with ‘energy’. Cassie and Baxter established their theories on roughness induced wettability

on Wenzel's perception of surface energies. They formulated the apparent contact angle of a liquid on a rough surface in a composite wetting state such that:

$$\cos\theta_{rough} = f_1\cos\theta_{smooth} + f_2\cos(180) \quad (1.4)$$

where  $f_1$  and  $f_2$  are the fractions of solid-liquid and solid-vapor interfaces under the droplet, respectively (the sum of  $f_1$  and  $f_2$  is unity and 180 refers to the contact angle of the liquid in air). Transformation from Wenzel to a Cassie-Baxter state occurs at a critical hydrophobicity of the solid for a given rough surface, or at a critical roughness for a given hydrophobic polymer [26,27], where the capillary pressure (Eq. (1.5), where  $\sigma$ ,  $\theta$ , and  $r$  are the surface tension of the liquid, wetting angle of the liquid on the surface of the capillary, and effective radius of the interface, respectively) becomes higher than the Laplace pressure ( $\Delta P$  in Eq. (1.6), where  $\sigma$  and  $R$  are the surface tension and radius of the droplet, respectively) of the droplets so that the droplet stands on protrusion tops on the rough surface. For a particular liquid, capillary pressure is basically a function of the width and (advancing) contact angle of that liquid on the surface of the capillary. A composite wetting state is associated with the inability of water intrusion into indentations, when the condition that the Laplace pressure cannot overcome the negative capillary pressure is satisfied. Therefore, surfaces composed of low surface energy materials and sufficiently rough micro topology show high (advancing) water contact angles due to the existence of composite interfacial state. Such surfaces are defined as *superhydrophobic* if the measured (advancing) contact angle is larger than  $150^\circ$ . Using the term superhydrophobic would be convenient only to indicate the sphere-like shape of water droplets having reduced contact area with the surface; however, a non-wettable surface must allow easy movement of droplets, which is more complex than a definition made with a single, static contact angle value (this is also why the unexplained term *advancing* appears in brackets in the sentences above).

$$p_c = \frac{2\sigma \cos \theta}{r} \quad (1.5)$$

$$\Delta P = \frac{2\sigma}{R} \quad (1.6)$$

## 1.4 The Famous Wenzel and Cassie-Baxter Equations are Indeed Wrong

Wenzel and Cassie-Baxter theories (sometimes denoted as laws) have been extensively referred in the area of roughness induced hydrophobicity (Corresponding references [24, 25] have been cited 2,737 and 2,582 times, respectively, by July 2012). However, the two theories were proven to be wrong in 2007 by McCarthy and his coworkers [23, 28], who had also been indicating the failure of these two theories to explain the dynamic behavior of droplets until then [29–32]. They demonstrated their claim with contact angle experiments on two-component surfaces which contained a ‘spot’ in a surrounding field as shown in Fig. 1.3(a) and (b). Advancing contact angle of smooth and rough regions in this experiment were about  $117^\circ$  and  $168^\circ$ , respectively. The main scope of the experiment was to investigate whether the area under the droplet affected the contact angles as indicated by Wenzel and Cassie-Baxter equations. The experiments started by measuring the contact angles of a droplet so small that its contact perimeter is inside the inner spot of the corresponding surface. Then, the droplet size was gradually increased by injecting water, while the contact angles were measured constantly. It is apparent from the frames of this experiment (Fig. 1.3(a)-III and (b)-III) that the droplets exhibit contact angles according to the contact region at the three phase contact line (let’s say, the outermost solid-liquid contact points on the solid surface, or the perimeter of the solid-liquid contact). For instance, on a Fig. 1.3(a)-I type surface having a 1 mm inner (rough) spot diameter, two water droplets having 0.5 and 1.1 mm diameter exhibited (advancing) contact angles  $168^\circ$  and  $117^\circ$ , respectively. On the other hand, Eq. (1.4) predicts a  $152^\circ$  contact angle for the latter case. Similarly, on a Fig. 1.3(b)-I type surface having a 1 mm inner (smooth) spot diameter, two water droplets having 0.5 and 1.1 mm diameter exhibited (advancing) contact angles  $117^\circ$  and  $168^\circ$ , respectively; whereas Eq. (1.4) predicts a  $123^\circ$  contact angle for the latter case. Accordingly, this experiment indicated that contact angle behavior is determined by interactions between the liquid and the solid at the three phase contact line alone and that, the interfacial area within the contact perimeter is irrelevant [23].

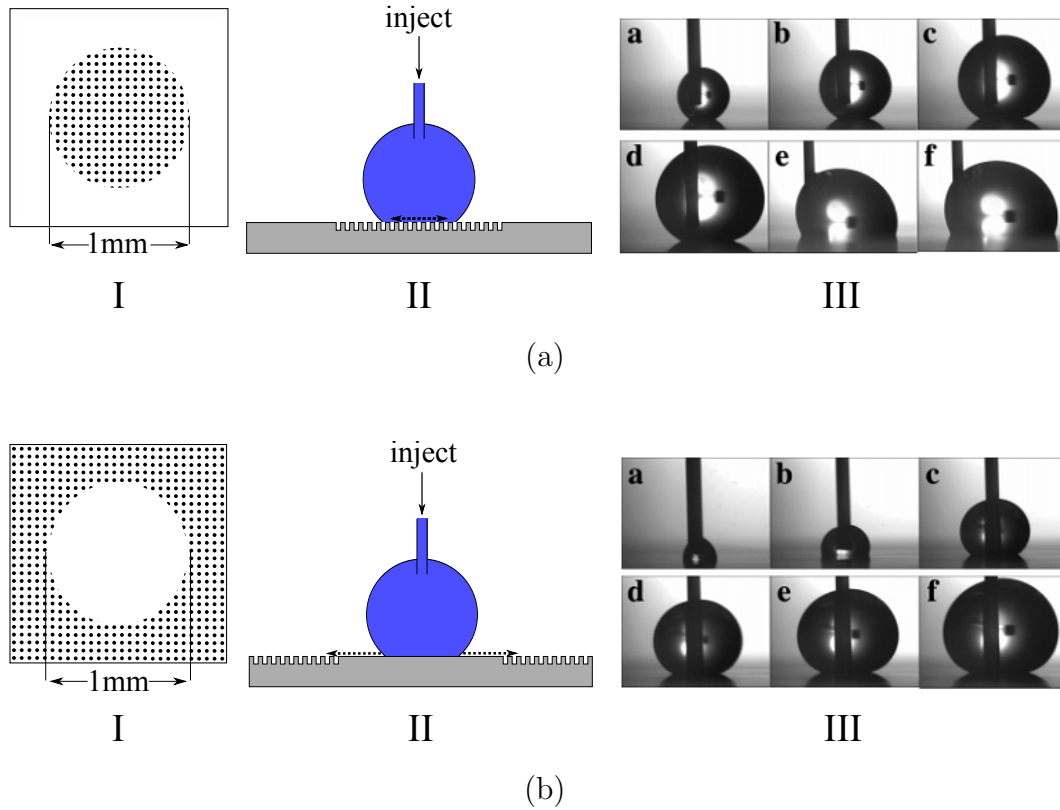


Figure 1.3: Surfaces that exhibit (a) a rough spot in a smooth field, and (b) a smooth spot in a rough field. Images labelled as I and II are the depictions of the surfaces and the wettability experiments, respectively, shown in frames labelled as III.

### 1.5 Three Phase Contact Lines: All Wetting Phenomena is Indeed a One Dimensional Issue

When a droplet moves on a surface, it advances on the front side and recedes on the rear side of the movement with two characteristic contact angles called *advancing* and *receding angles* denoted as  $\theta_A$  and  $\theta_R$ , respectively, as shown in Fig. 1.4(a). At the front side of the moving droplet, water molecules at the contact line indeed do not move but water molecules at the liquid-vapor interface near the contact line fall down onto the surface to form a new line (Fig. 1.4(c)). Thus, old contact line becomes a part of the solid-liquid interface [32]. To a what extent the liquid-vapor interface must descend to make a contact with the solid surface can be measured and quantized as the advancing contact angle,  $\theta_A$ . At the rear side of the motion, however, contact line must come off

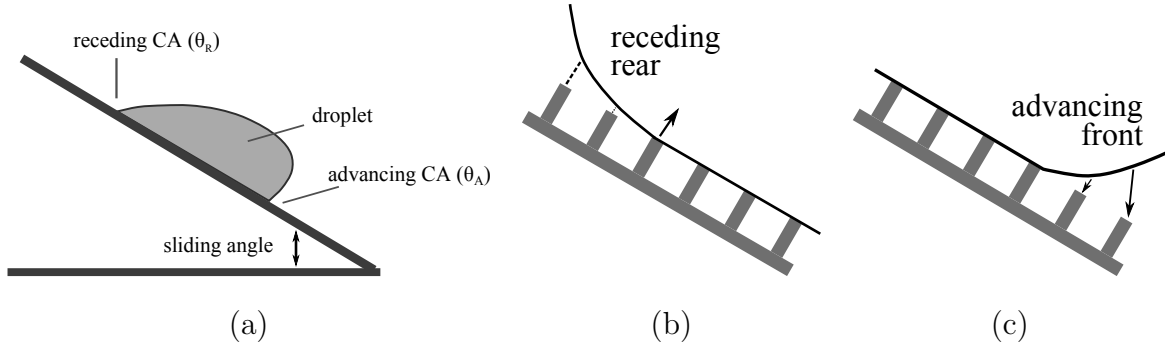


Figure 1.4: Physical events that occur during movement of a droplet. (a) Advancing and receding contact angles of a droplet moving on a tilted surface. Movement of three phase contact line during receding (b), and advancing (c).

the solid surface and recede into the liquid, while a new line is formed simultaneously by the molecules which were previously forming the solid-liquid interface near the contact line (Fig. 1.4(b)). This event requires an activation energy formed fundamentally by the adhesive forces that hold the contact line in its metastable state. For a sessile droplet, this energy barrier is overcome if the surface is tilted and droplet is distorted due to gravitational forces until the rear contact angle reaches down the critical, receding angle  $\theta_R$ , at which the component of the liquid surface tension vector parallel to direction of droplet movement ( $\sigma_{LV} \cos \theta_R$ ), becomes sufficiently large. Topographical structure and chemical composition of a surface determines a unique advancing and receding angle for a particular liquid. At a given time, a liquid cannot have a contact angle larger than  $\theta_A$  and smaller than  $\theta_R$  since any attempt would bring back the angle in between these critical values by advancing or receding the contact line. On the other hand, contact angle can take every value between  $\theta_A$  and  $\theta_R$ . Various contact angles may occur through condensation or evaporation of droplets, or might be adjusted by injecting liquid into or withdrawing liquid from a sessile droplet. If the the contact angle of a sessile droplet is close to  $\theta_A$ , droplet would readily advance by a slight tilting of the surface but cannot move until it reaches a distorted shape that exhibit  $\theta_R$  at the rear side. Similarly, if the contact angle is closer to  $\theta_R$ , the droplet would not move until the tilt angle of the surface provides a front contact angle equal to  $\theta_A$ , although the rear side would readily recede. These discussions brings out the concept of *contact angle*

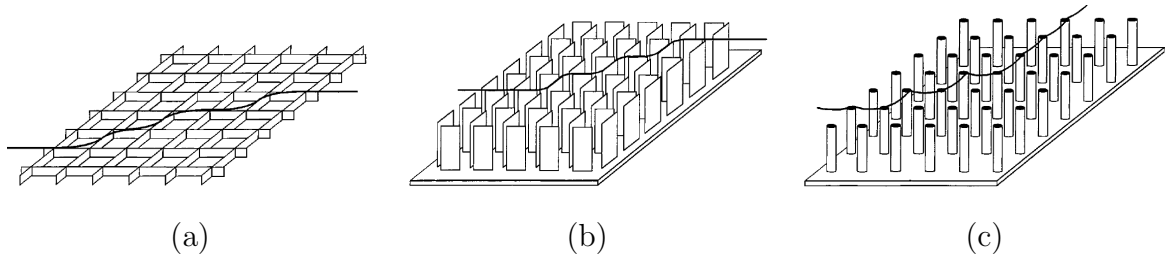


Figure 1.5: Pictorial representations of surfaces with three different roughness topologies. The darker lines describe possible three-phase contact lines for a drop of water in contact with these surfaces: (a) A screen on which a fairly continuous contact line can form, (b) separated ridges on which a discontinuous but substantial contact line can form, and (c) separated posts on which a very discontinuous contact line must form.

*hysteresis*, the difference between the advancing and receding contact angles, which is fundamental for wetting phenomena according to the equation [33]:

$$mg \frac{\sin \alpha}{w} = \gamma_{LV} (\cos \theta_r - \cos \theta_a) \quad (1.7)$$

where  $\alpha$  is the threshold angle of inclination for movement of a sessile droplet with a mass  $m$  and a width  $w$ . If a hydrophobic smooth surface is transformed into a Cassie-Baxter state by introducing sufficient roughness, the composite interface structure under the contact line leads to even higher advancing angles by effective slip on air pockets due to high capillary pressure of the cavities [34–40]. However, topographical structure of the surfaces may suggest various shapes and resultant behaviors for contact lines. Composite surfaces of fractal topographies lead to formation of discontinuous contact lines that result low hysteresis as shown in (Fig. 1.5(c)) [29]. On the other hand, contact line follows the topography continuously on composite surfaces formed by structures such like fibers, straight walls etc. (Fig. 1.5(a)), thus receding of the line requires high activation energy and droplets are pinned. These discussions indicate that the geometrical structure of the surface roughness determines the stability of the contact line, thus, dynamic behavior of droplets. Droplets are unstable on surfaces having zero contact angle hysteresis and impossible to be immobilized with any effort.



## 1.6 Measurement of Dynamic Contact Angles

As mentioned previously, a droplet can take any contact angle value that is between the advancing and receding contact angles. Thus, wettability of a surface can only be defined by these two critical angles, or by a function of them.  $\theta_A$  and  $\theta_R$  are generally measured with a conventional contact angle goniometer, preferably equipped with a drop shape analyzer software. For the measurement of  $\theta_A$ , usually a small droplet is deposited on the surface, as shown by step 1 in Fig. 1.6(a), and the contact angle is increased by continuously injecting water (steps 2, 3, and 4). At a certain droplet size, additional injection of water do not increase the contact angle but leads to the movement of three phase contact line (steps 5 and 6). A snapshot of the droplet is taken while the contact line moves, and the contact angle is measured and regarded as  $\theta_A$ . Measurement of  $\theta_R$  is performed by depositing a large droplet on the surface and decreasing the contact angle by withdrawing water from the droplet as shown by steps 1, 2, and 3 in Fig. 1.6(b). At a certain droplet size, withdrawal of water do not decrease the contact angle any more but leads to the retraction of three phase contact line (steps 4 and 5). A snapshot of the droplet is taken while the contact line moves, and the contact angle is measured and regarded as  $\theta_R$ .

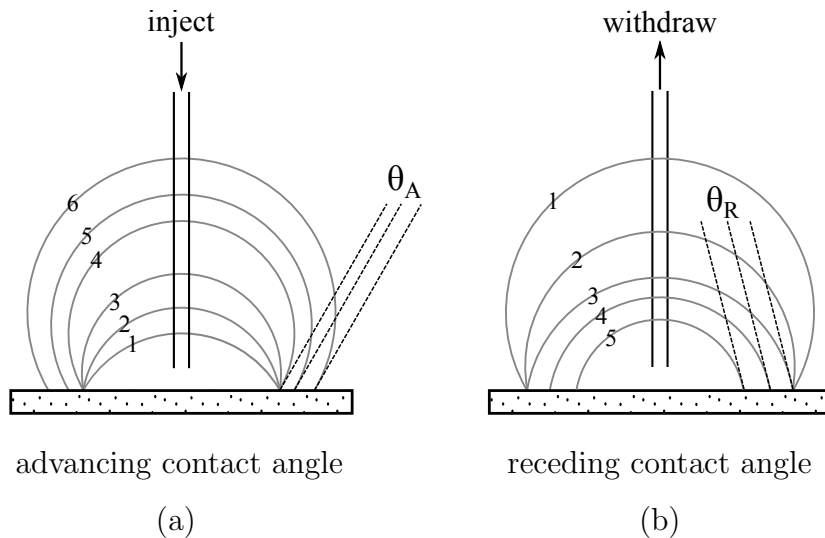


Figure 1.6: Pictorial representations of (a) advancing contact angle, and (b) receding contact angle measurement. Numbers indicate the order of experimental steps.

## 1.7 On the Delusion Created by High Static Contact Angles

One can perform a basic search in Web of Science with the keyword *superhydrophobic* as the topic to notice that superhydrophobicity has been one of the hot subjects of natural sciences in the last decade. A search spanning the time between July 2002 and 2012 returns 3,421 results, which correspond to about one paper per day on the average. One can also make a new search within these results with the keywords *advancing*, *receding*, *hysteresis* or *sliding* to realize that only about 11 % of these studies discuss the dynamic behavior of droplets. It appears that probably a single, static contact angle value is reported in most of these studies to use the term superhydrophobic (contact angles  $> 150^\circ$ ) and its irrelevancy for the ease of droplet movement is mostly ignored. The reason why high advancing contact angle values occur on superhydrophobic, rough surfaces was discussed in Section 1.5. Although a droplet can take any contact angle value between advancing and receding contact angles, common observation of high static contact angles on superhydrophobic surfaces has very simple dynamics as depicted in Fig. 1.7. When a droplet is being deposited on a superhydrophobic surface, it touches the surface with its contact angle at air:  $180^\circ$ . The three phase contact line advances

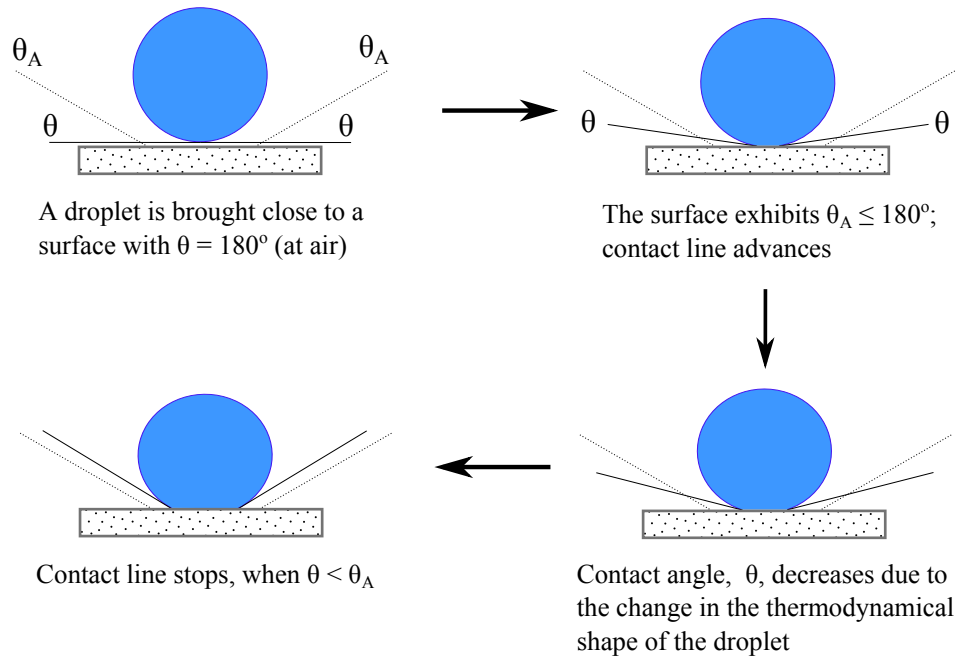


Figure 1.7: Dynamics of static droplet formation.

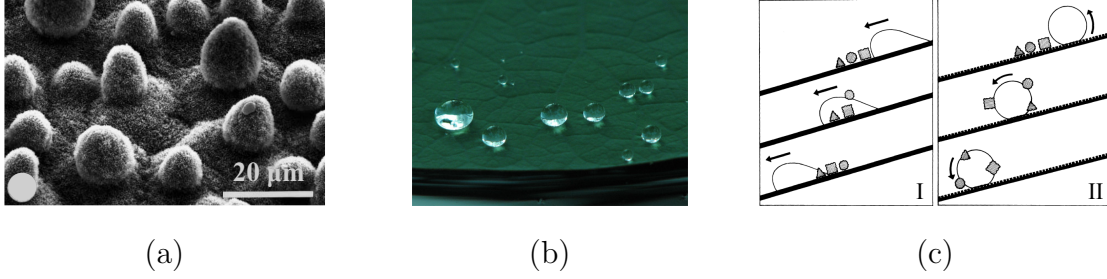


Figure 1.8: (a) SEM micrograph of the *Nelumbo nuicefera* (Lotus) leaf surface, (b) water droplets on the Lotus leaves, and (c) connection between roughening and self-cleaning.

since  $180^\circ$  would be higher than the  $\theta_A$  of the surface, while the contact angle of the droplet gets smaller due to the change in the thermodynamic shape of the droplet. The movement of the contact line continues until the contact angle of the droplet becomes just smaller than  $\theta_A$ . Accordingly, a static droplet with a contact angle very close to the  $\theta_A$  of the surface occurs. Scientists generally measure contact angles of static droplets deposited via a syringe equipped with a needle, by *sessile droplet methods* of contact angle goniometers, and report these values to characterize the wettability of their surfaces. Studies on roughness induced hydrophobicity gained much attention particularly after the relation between the *self cleaned* surfaces of the *Lotus* plant leaves and the mesoscale roughness on them was established (Fig. 1.8) [41]. On smooth surfaces, the particles are mainly redistributed by water (Fig. 1.8(c)-I, but on rough surfaces, they adhere to the droplet surface and are removed when the droplets roll off (Fig. 1.8(c)-II). This physics is indeed the underlying mechanism responsible for the ever clean surface of the leaves; however, it was the spherical shape of droplets (i.e. high static contact angles) on which scientists have mainly focused (Fig. 1.8(b)).

## 1.8 Dual Length Scales of Topography is the Route to Zero Hysteresis

Both advancing and receding events involve the movement of three phase contact line but underlying mechanisms are different for the two phenomena [32]. On most superhydrophobic surfaces, as mentioned previously, advancing contact angles are relatively high, even may be very close to  $180^\circ$ , due to large effective slip of water (contact line) over air pockets in the cavities which exhibit high capillary pressure; therefore, magni-

tude of  $\theta_R$  is usually more influential on hysteresis. One effective strategy for reducing or eliminating contact angle hysteresis was described as increasing the receding contact angle of the protrusion tops of a surface on a composite wetting state [42]. This was accomplished by introducing nanoscopic roughness on the micron scale post tops in the corresponding reference. The  $\theta_A/\theta_R$  values on the rough surface shown in Fig. 1.9(a) was  $176^\circ/156^\circ$ . The values were  $104^\circ/103^\circ$  on the smooth surface of the same material. On this rough surface, the droplet is at  $\theta_A=176^\circ$ , and the smooth tops of the posts exhibit  $\theta_A=104^\circ$ . Thus, there is obviously no kinetic barrier to advancing and water must spontaneously advance over the posts. On the other hand, the droplet is at  $\theta_R=156^\circ$ , and the smooth tops of the posts exhibit  $\theta_R=103^\circ$ . Accordingly, segments of the contact line cannot move independently on individual post tops, but must disjoin from entire post tops in concerted events in order to move. This receding contact line pinning, due to the disjoining pressure, gives rise to the  $20^\circ$  hysteresis. However, when the receding angle of the post tops was increased by introducing nano scale roughness (Fig. 1.9(b)),  $\theta_A/\theta_R$   $176^\circ/176^\circ$  (zero hysteresis) is measured. The nanoscopic roughness facilitates receding by minimizing the amount of contact on the post tops as shown in (Fig. 1.9(c)). Authors indicated that water droplets do not come to rest, and roll effortlessly on this surface containing two length scales of topography.

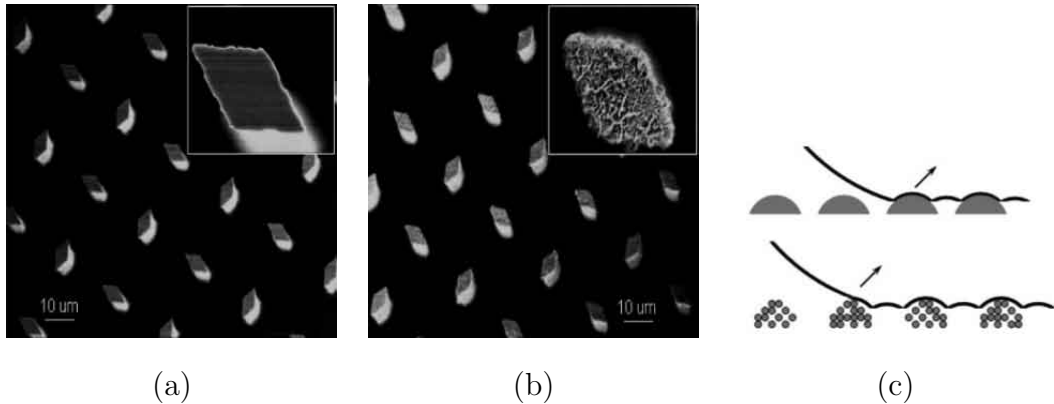


Figure 1.9: (a) Scanning electron microscopy (SEM) image of a surface containing staggered  $4 \times 8 \times 40 \mu\text{m}$  rhombus posts, (b) SEM image of the surface shown in panel a after introducing nano scale roughness, and (c) receding event on micron (top) and dual scale (bottom) surface.

## 1.9 New Definitions Related to Wettability

In order to differentiate low hysteresis *slippy* surfaces, whether having high contact angle values or not, from the high hysteresis, *sticky* superhydrophobic surfaces, the term *ultrahydrophobic* was suggested [29] upon asking the question “Which surface is non-wettable?”. In another example presented by the photographs in Fig. 1.10(a), when a droplet of water is placed on a flat Teflon film, the “benchmark” of hydrophobicity, the polymer instantaneously wraps the droplet. So, how suitable or adequate it is to label Teflon as hydrophobic? The term ultrahydrophobic is evidently a better choice to refer to non-wettable surfaces on which droplets can move easily. The fact that a droplet on a surface can take every value between  $\theta_A$  and  $\theta_R$  obviously provokes avoiding the definitions of the wettability by taking a single contact angle value into account. In addition, a definition, such as ultrahydrophobic, which fundamentally depends only on the value of hysteresis, would be inadequate to differentiate between low hysteresis surfaces of low contact angles and high contact angles. Therefore, new practical definitions taking both hysteresis and the value of contact angles were made [43]. For instance, as shown in Fig. 1.10(b), a surface with  $\theta_A/\theta_R$   $60^\circ/60^\circ$  supports a small droplet of water when held perfectly horizontal but does not if the surface is slightly tilted. Such surfaces are regarded as *shear hydrophobic* due to low hysteresis, and *tensile hydrophilic* due to low  $\theta_A$  value. On the other hand, a droplet needs to distort from a section of a sphere in order to slide on a surface, for example, with  $\theta_A/\theta_R$   $170^\circ/120^\circ$ . Such surfaces are regarded as *shear hydrophilic* due to being sticky, but *tensile hydrophobic* because of their high  $\theta_A$ . An additional definition was made for a particular extreme surface having  $\theta_A$  and  $\theta_R$  both  $180^\circ$  as *perfectly hydrophobic* [44]. The importance of such surfaces is that they exhibit the maximum water contact angle values attainable on a solid surface, and work of adhesion between water droplets and them is zero.

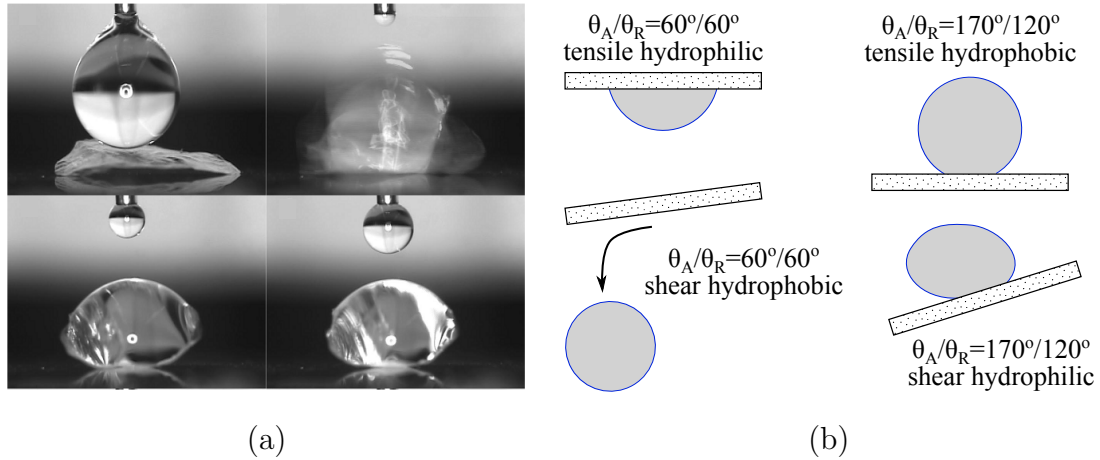


Figure 1.10: (a) Frames of a videotape of a droplet ( $8.5 \mu\text{L}$ ) of water being placed onto a thin film of Teflon ( $\approx 3.7 \mu\text{m}$  thick), and (b) differences between shear and tensile hydrophobicity.

## 1.10 Perfectly Hydrophobic Surfaces

It is fundamentally impossible to immobilize a droplet on a non-wettable surface with zero hysteresis unless the surface is hold perfectly horizontal (which would obviously extremely challenging in a physical world). The driving forces for the movement of droplets might be gravity, wind etc. which deform the droplet shape into a geometry such that advancing and receding angles are reached. However, in the absence of such driving forces, for instance in space, even zero hysteresis surfaces would exhibit adhesion towards water and work would be required to separate them from each other unless the receding angle is  $180^\circ$ , i.e. the surface is perfectly hydrophobic.

Literature data on perfectly hydrophobic surfaces is very rare (only three papers existed by July 2012). The first study that reported a perfectly hydrophobic surface was published in 2006 [44]. In this study, silicon wafers were submerged in toluene solutions of  $\text{MeSiCl}_3$  at room temperature, rinsed with toluene and extracted with ethanol at 40-65 % relative humidity. This process yielded a surface composed of a random nanofiber network as shown in Fig. 1.11(a). Wettability analysis of this surface revealed contact angles  $\theta_A$  and  $\theta_R$  both  $180^\circ$ , thus the surface was regarded as perfectly hydrophobic. The next reported perfectly hydrophobic surface was from a commercially

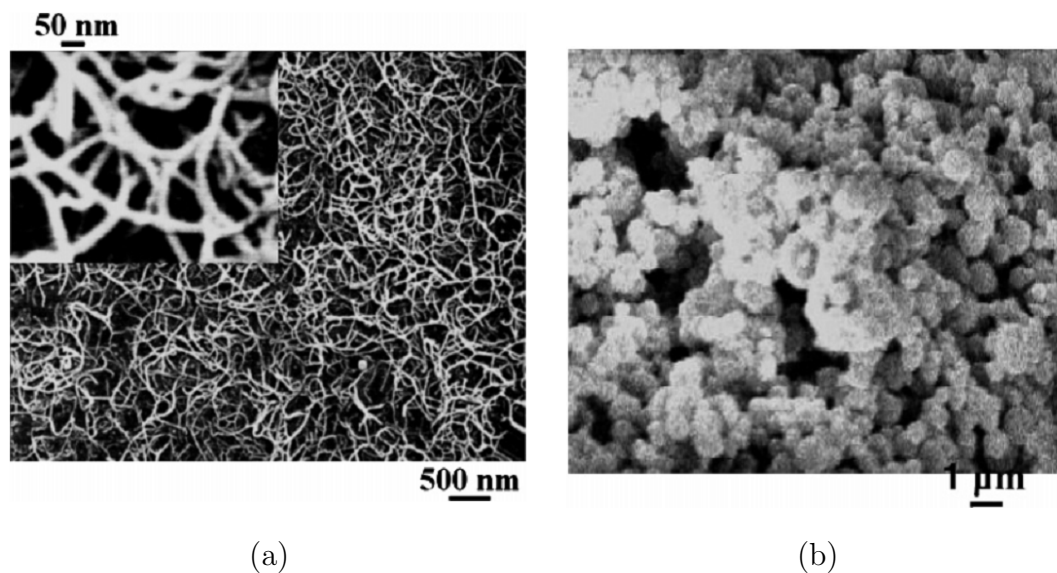


Figure 1.11: (a) First ever reported perfectly hydrophobic surface, and (b) SEM micrograph of the compressed sample of tetrafluoroethylene oligomer.

available, variable diameter submicrometer particles of tetrafluoroethylene oligomers [45], which was stated to be available in kilogram quantities. The authors prepared perfectly hydrophobic surfaces by pressing this waxy material between two flat surfaces to form a monolithic supported compressed sample. The surface is indicated to comprise at least two levels of topography; these arise from the submicrometer size spherical particles and the greater length scale roughness of the compressed sample. An SEM micrograph of the perfectly hydrophobic surface is given in Fig. 1.11(b).

The third and last published study on perfectly hydrophobic surfaces described a procedure for forming polystyrene nanoneedle arrays by utilizing the trapping of inorganic silica particles at the polystyrene/air interface via capillary wetting of a thermoplastic polystyrene polymer and  $\text{SF}_6$  reactive-ion etching [46]. A monolayer of silica microspheres was formed and trapped on the smooth PS film, and subsequent wet etching with HF and reactive-ion etching with  $\text{SF}_6$  left behind hexagonal arrays of protruding tips with tip diameters around 20 nm as shown in Fig. 1.12. The common characteristics of the three aforementioned studies is that, although not explicitly explaining the mechanism of perfect hydrophobicity, they exhibit an implication of (from SEM images or indirect statements) nanoscopic roughness distribution on micron scale

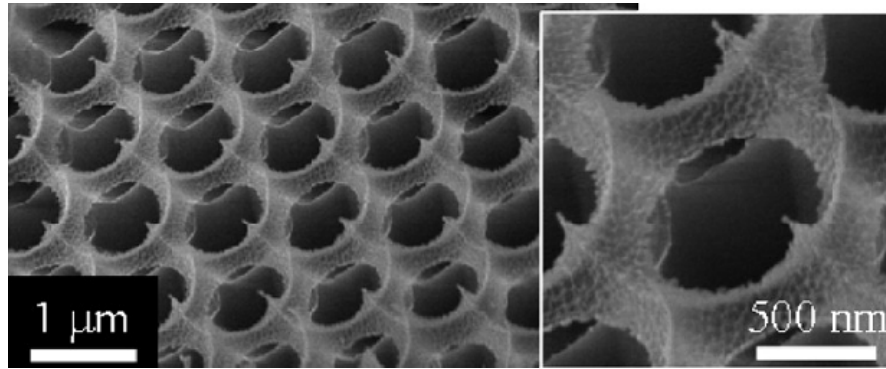


Figure 1.12: SEM micrograph of the hexagonal nanoneedle array.

features, which might be the route to perfect hydrophobicity.

### 1.11 Introduction to Electrospinning

Electrospinning is a widely known, cost efficient and versatile method to prepare polymeric nanofibers [47–49]. The process basically involves drawing an electrically charged jet of polymer solution or melt towards a grounded collector and formation of micro and nanofibers upon elongation and thinning of this jet prior to solidification, as schematically shown in Fig. 1.13(a). Several studies report the utilization of the electrospun fiber morphologies to achieve rough topographies which lead to formation of superhydrophobic surfaces [50–62]. When the solution viscosity is low, however, solution jet may break up into spherical droplets (Fig. 1.13(b)) which generally form micron size

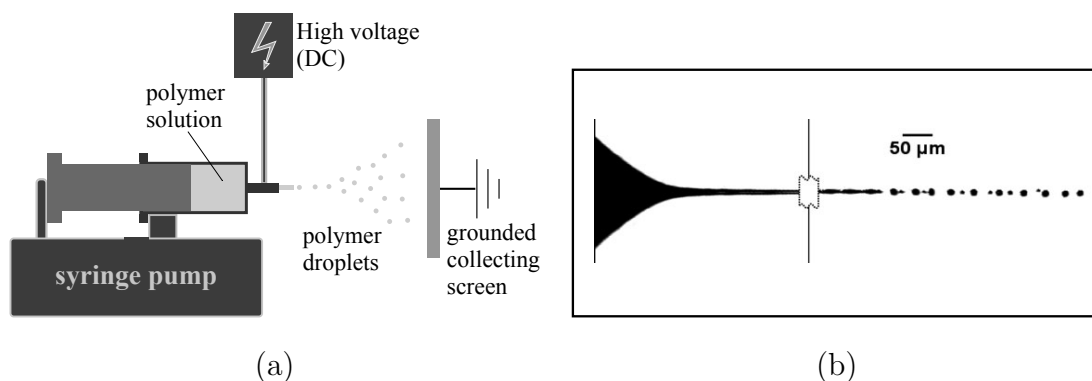


Figure 1.13: (a) Schematic representation of electrospinning, and (b) high-speed photographs of electrospinning process where jet breaks up into separate droplets.



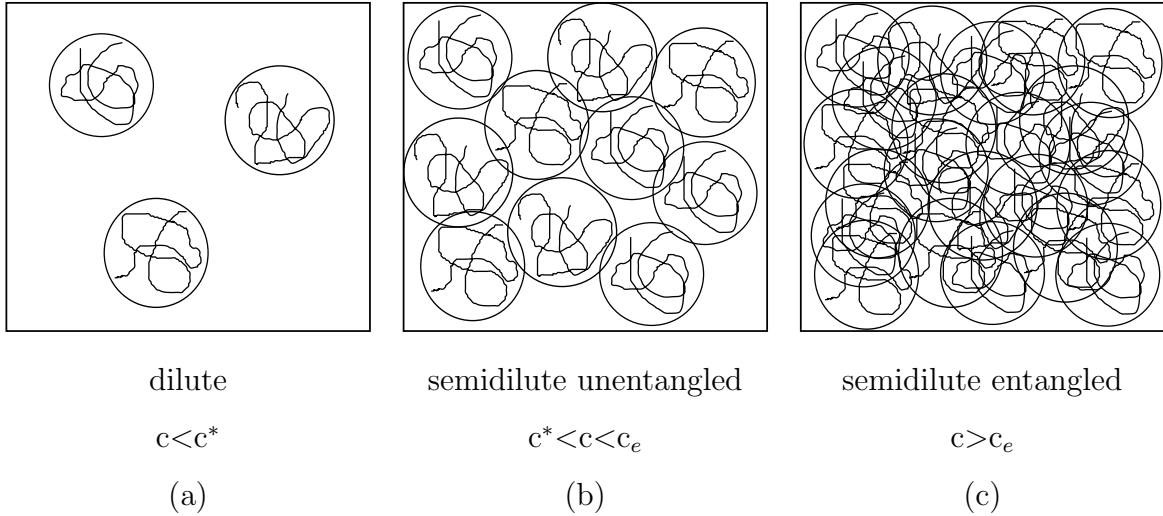


Figure 1.14: Physical representation of three solution regimes.

beads upon drying and the process is termed as *electrospraying*. Formation of beads during electrospraying is commonly attributed to the breaking up of the polymer solution jet due to deficiency of chain entanglements [63, 64] and formation of spherical droplets induced by surface tension [65]. Electrospraying may occur at a semidilute unentangled solution regime whose lower and upper limits are defined by two critical properties, chain overlap concentration ( $c^*$ ) and chain entanglement concentration ( $c_e$ ), respectively (Fig. 1.14). In fact, *electrohydrodynamics* is a complex phenomena controlled by many other parameters including permittivity, dielectric constant, density, surface tension, conductivity and the flow rate of the liquid, as well [66]. If the parameters favor electrospraying, disintegration of droplets from the charged solution jet is followed by the formation of a semi-flexible skin layer due to fast evaporation of solvent from the surface of the droplet, leaving a polymer rich phase in the surface and solvent rich phase in the core. Diffusion of solvent from core to the surface prior to complete solidification may lead to collapse of the skin layer into wrinkled, dimpled, dish shaped, cuplike, or hollow structures depending on the process conditions and polymer type [67–73] (Fig. 1.15).

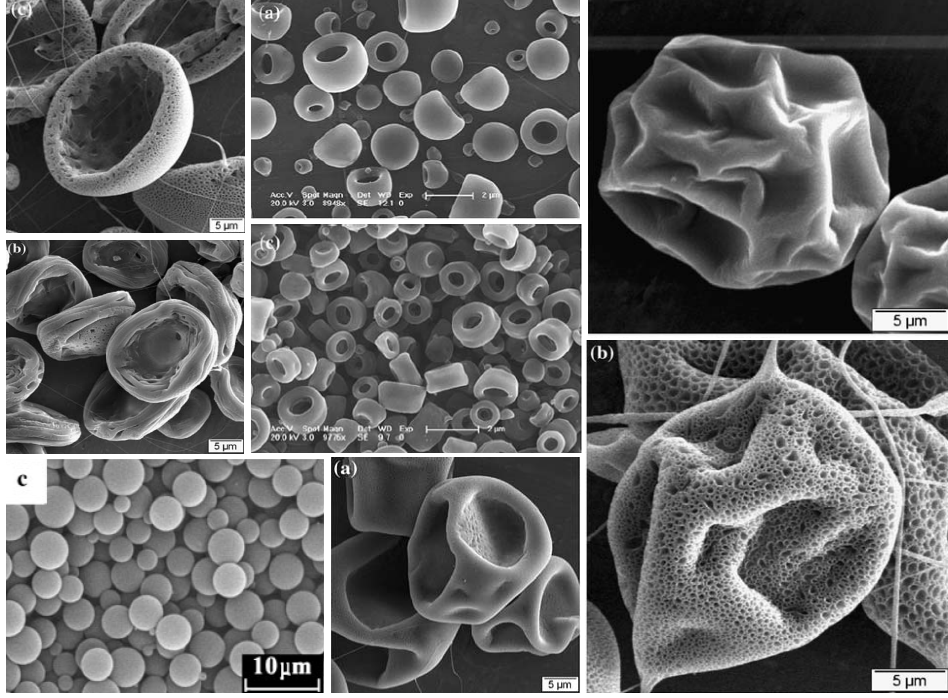


Figure 1.15: Various bead shapes that may occur during electrospraying.

## 1.12 Dissipative Particle Dynamics

Dissipative particle dynamics (DPD) technique has become a common mesoscopic method to understand the self-assembly behavior of polymers, surfactants and many other systems since its introduction in the early 1990s as a method to study the rheological behavior of polymers [74–83]. As a coarse grained simulation technique, DPD uses beads which represent clusters of atoms and deals with bead-bead interactions computed from atomistic simulations. This process allows performing simulations with length and time scales as long as micrometers and microseconds, respectively. In the DPD of macromolecules, polymers are represented by beads connected with linear harmonic springs.

The beads in DPD interact according to Newton’s equations of motion:

$$\frac{d\vec{r}_i}{dt} = \vec{v}_i, \quad \frac{d\vec{v}_i}{dt} = \vec{f}_i \quad (1.8)$$

where  $\vec{r}_i$ ,  $\vec{v}_i$ , and  $\vec{f}_i$  are the position vector, velocity, and force, acting on the particle  $i$ , respectively. All bead masses are assumed to be equal and set to unity for simplicity.

The force  $\vec{f}_i$  is the sum of three pairwise additive components such that:

$$\vec{f}_i = \sum_{j \neq i} (\vec{F}_{ij}^C + \vec{F}_{ij}^D + \vec{F}_{ij}^R) \quad (1.9)$$

where the summation is over all other particles  $j$  that are within a critical cutoff radius  $\vec{r}_c$  of bead  $i$ . This value is also set to unity for simplicity.  $\vec{F}_{ij}^C$  is the conservative force which is acting as a soft repulsion along the line connecting the center of beads  $i$  and  $j$ , and represented by:

$$\vec{F}_{ij}^C = \begin{cases} a_{ij}(1 - r_{ij})\hat{r}_{ij}, & (r_{ij} < 1) \\ 0, & (r_{ij} \geq 1) \end{cases} \quad (1.10)$$

where  $a_{ij}$  is a maximum repulsion between beads  $i$  and  $j$ ,  $\vec{r}_{ij} = \vec{r}_i - \vec{r}_j$ ,  $r_{ij} = |\vec{r}_{ij}|$ , and  $\hat{r}_{ij} = \vec{r}_{ij}/|\vec{r}_{ij}|$ .  $\vec{F}_{ij}^D$  is the dissipative force, which is proportional to the relative velocities of the beads  $i$  and  $j$  with respect to each other, acts so as to reduce their relative momentum. The random force  $\vec{F}_{ij}^R$  maintains the system temperature. The dissipative and random forces also act along the line of centers and conserve linear and angular momentum. In DPD, internal degrees of freedom of the clusters are integrated out as bead representations, and a momentum conserving stochastic thermostat of the pairwise dissipative and random forces is used. Therefore, the conservative soft repulsive force is the main factor that drives the system. Accordingly, the parameters  $a_{ij}$  are referred as bead-bead repulsion parameters, in other words, DPD interaction parameters, which fundamentally depend on the underlying atomistic interactions.

### 1.13 The Scope of the Study

Inspired by the water repellent behavior of the ever-clean Lotus leaves, remarkable effort has been presented to mimic the mesoscopically rough plant surface to achieve the similar behavior on artificial surfaces [84–94]. Although the beads in electrospinning are generally regarded as defects in the nanofiber production, we have reported that the roughness introduced by the beaded surface morphology leads to water repellency if the electrospayed polymer is hydrophobic [95]. The fractal structure of the beaded topography implied a very discontinuous contact line that allowed droplet movement

at relatively low tilt angles. However, starting with this study on superhydrophobic electrospayed surfaces, we have performed hundreds of experiments with various hydrophobic polymers and observed that these beaded topographies always exhibited contact angle hysteresis (although to a small extent, most of the time). In this study, it was demonstrated that the nanoscopically smooth nature of the micron size beads play an important role to obstruct the recession of contact lines.

In this thesis, a facile method to achieve perfect hydrophobicity ( $\theta_A$  and  $\theta_R$  both  $180^\circ$ ) on electrospayed superhydrophobic surfaces of a poly(styrene-*co*-perfluoroalkyl ethylacrylate) copolymer is described. The overall study consists of:

1. Formation of micron size beads due to fast evaporation of low boiling point good solvent from the electrospayed droplets
2. Formation of nanoparticles on the micron size beads via phase separation of the polymer drying from the high boiling point poor solvent trapped in the core of the droplets
3. Control of the nanoscale roughness distribution on the individual beads, and overall coating as well, by tuning the electrospaying process parameters
4. Achieving a dual scale (micron and nanometer) rough surface by partially coating the substrate

Bead formation is the most recognized outcome of polymer electrospaying. The bead sizes could be tuned by varying the polymer concentration in good solvents such as tetrahydrofuran and chloroform, and fairly low threshold sliding angles were measured on the coated surfaces. On the other hand, nanoscopically rough beads achieved through addition of high boiling point poor solvents, such as dimethylformamide and dimethyl sulfoxide, to the solutions were quite interesting. This topography is predicted to form by phase separation of the polymer during final drying of the beads from the high boiling point poor solvent. Eventually, electrospaying parameters were successfully controlled to achieve dual scale rough topographies, by partially coating the substrate with nanoscale rough bead hills. Threshold sliding angles, and therefore

contact angle hysteresis, were zero on these surfaces. Droplet videos recorded during a contact and release experiment with a conventional contact angle goniometer revealed that these surfaces have no affinity to water droplets. In addition, the adhesive forces between the droplets and surfaces were measured using a microbalance, and it was observed that the force of adhesion also was zero on the dual scale rough surfaces. This observations indicated that receding angles (advancing angles as well, according to zero hysteresis condition of Eq. (1.7) were  $180^\circ$  on these surfaces. It is claimed that among the previously described studies regarding superhydrophobic surfaces produced by electrospraying [96,97], this method is novel, particularly as a one to achieve perfectly hydrophobic surfaces.

In order to rationale the formation of different morphologies in the corresponding electrospraying, dissipative particle dynamics (DPD) technique was applied. The morphological behavior of the copolymer in THF and DMF was investigated via DPD simulations. In addition to computational work, dynamic light scattering measurements were performed to have insight about the hydrodynamic behavior of the polymer chains in the corresponding solvents. Analysis revealed that simulations and experimental results correlate well since both methods pointed out the self assembly of the copolymer in the poor solvent.

## Chapter 2

### Materials and Methods

#### 2.1 Materials

Styrene (technical) was purified by passing through an alumina column. Perfluoroalkyl ethylacrylate (PFA,  $\text{H}_2\text{CCHCO}_2(\text{CH}_2)_2(\text{CF}_2)_n\text{CF}_3$ ,  $n =$  mixture of 6, 8, and 10, Clariant Fluowet AC812), trichloro ethylene (TCE, Carlo Erba), tetrahydrofuran (THF, Merck), *N,N*-dimethylformamide (DMF, Merck), chloroform (Riedel), dimethyl sulfoxide (DMSO, Sigma-Aldrich), and ethanol (technical grade) were used as received. 2,2'-azobisisobutyronitrile (AIBN, Fluka) was recrystallized from methanol and stored at  $-20\text{ }^\circ\text{C}$  prior to use.

#### 2.2 Synthesis and Bulk Characterization of Poly(St-co-Perfluoroalkyl ethylacrylate)

Poly(St-co-PFA) random copolymer was synthesized as 10 mol % PFA. AIBN was used as the initiator and THF was used as solvent. Reaction was carried out by a free radical solution copolymerization at  $65\text{ }^\circ\text{C}$  for 5 days. Pure copolymer was achieved by first precipitating the solution in ethanol, then washing with ethanol several times and finally drying in a vacuum oven at  $55\text{ }^\circ\text{C}$  for 12 hours. Copolymer compositions were determined by  $^1\text{H-NMR}$  (500 MHz Varian Inova) peak integrations. Molecular weight and molecular weight distribution were determined by an Agilent Model 1100 gel permeation chromatograph. Molecular weights were calibrated using poly(methyl methacrylate) and polystyrene standards.

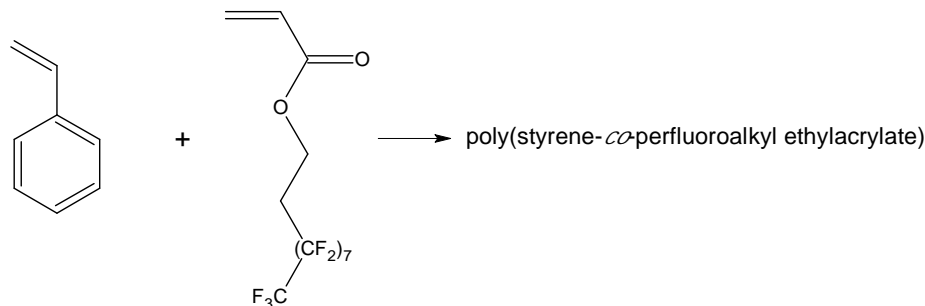


Figure 2.1: Synthesis of Poly(St-*co*-Perfluoroalkyl ethylacrylate).

### 2.3 Electro spraying of the Copolymer Solutions

Electrospraying was performed using a Gamma High Voltage ES30 power supply and a New Era NE-1000 syringe pump to control the solution feed rates. A schematic representation of the setup was given in Fig. 1.13(a). In all experiments, tip to ground distance was kept constant at 10 cm. Solutions were prepared by dissolving the copolymer in the corresponding solvent system and stirring at room temperature for at least 30 min.

### 2.4 Characterization of Surface Topographies

Surface morphologies of the smooth films were analyzed with a Multimode-Nanoscope III atomic force microscope (AFM) in the tapping mode and surface roughness was evaluated with the help of Nanoscope software. Surface morphology analysis of the electro sprayed films were performed with a LEO Supra VP35 FE-SEM after sputter deposition of a thin conductive carbon coating onto samples.

### 2.5 Wettability Analysis

Contact angle analyses of the samples were performed with a Krüss GmbH DSA 10 Mk 2 goniometer with DSA 1.8 software. In all of the measurements, freshly distilled ultra-pure Milipore water was used. Threshold sliding angle measurements were performed by first depositing a 10  $\mu\text{L}$  water droplet on a horizontal surface and then gently tilting

the surface with the help of a micrometer until the droplet started to move.

Hydrophobicity of the copolymer was determined using contact angle analysis on smooth copolymer films prepared by dip coating a 6 wt% TCE solution onto freshly cleaved mica surfaces at a rate of 2 mm/min. The force required to separate a droplet from a superhydrophobic surface was measured by the microbalance of a KSV Sigma 700 Force Tensiometer having a force resolution of 0.1  $\mu\text{N}$ . The superhydrophobic surface and the droplet were contacted and separated with a rate of 0.5 mm/min. For each surface, 4 consecutive measurements from 5 different regions of the surface were averaged.

## 2.6 Particle Size Measurements

Particle size analysis of the samples were performed by dynamic light scattering (DLS) technique with a Malvern Instruments Zetasizer Nano-ZS. DLS measures the dynamic fluctuations of scattered light intensity from the Brownian motion of the particles in a liquid media and performs a velocity distribution analysis, which can be correlated to a hydrodynamic diameter/radius via Stokes-Einstein equation. For the preparation of samples for each analysis, 3 mg polymer was transferred into a 15 g of corresponding liquid and stirred rigorously with a magnetic stirrer for 30 min. If performed additionally, an ultrasonicator was used to disperse the particles/chains in the liquid media. 1 mL of the dispersion is gently transferred into a quartz cuvette and a total of 90 measurements were averaged from 3 different batches that belong to the same dispersion.

## 2.7 Atomistic Simulations for DPD Parametrization

Solubility parameters,  $\delta$ , were calculated by atomistic simulations using the Amorphous Cell module of MATERIALS STUDIO following a geometry optimization of the beads. COMPASS 52 force field was used for both optimization and MD processes. A successive 1 ps equilibration step and 100 ps MD simulations were performed on simulation boxes containing 10 beads of the same type with a density of 1.0. For all non-bonded interactions, a cut-off radius,  $r_c$ , of 8.5 Å and periodic boundary conditions were applied



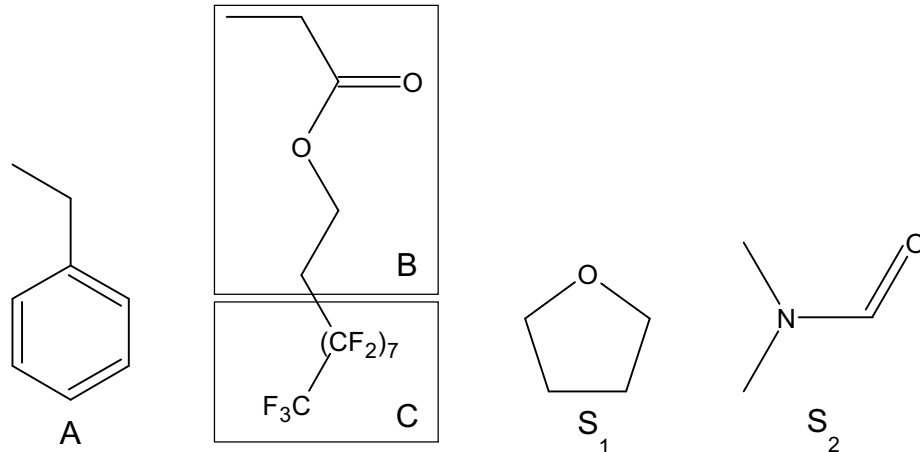


Figure 2.2: Partitioning of the beads for coarse-grained simulations.

in the canonical ensemble. Initial velocities were assigned from a Maxwell Boltzmann distribution such that total momentum in all directions equals to zero. Average molar volume of the beads,  $V_m$ , were calculated using the ACDLabs/ChemSketch 5.0 and the Hildebrand solubility parameters were determined according to Eq. (2.1), where  $\Delta E_v$  and  $CED$  correspond to molar energy of vaporization and cohesive energy density, respectively.

$$\delta = \left(\frac{\Delta E_v}{V_m}\right)^{1/2} = (CED)^{1/2} \quad (2.1)$$

## 2.8 Parametrization of Interactions for the Coarse-Grained DPD Methodology

DPD bead partitioning of the copolymer is shown in Fig. 2.2 as A, B and C stand for the styrene, ethyl acrylate and perfluoroalkyl segments, respectively. In addition, solvents THF and DMF are labelled as beads  $S_1$  and  $S_2$ , respectively, without any segmentation. Flory-Huggins interaction parameters,  $\chi_{ij}$ , were calculated according to Eq. (2.2) using the solubility parameters determined from atomistic simulations. The DPD interaction parameters,  $a_{ij}$  were calculated according to the linear relationship put forward by Groot [77] as  $a_{ii} = 25k_B T$  and  $a_{ij} \approx a_{ii} + 3.27\chi_{ij}$  for a box density,  $\rho$ , of 3 DPD units.

$$\chi_{ij} = \frac{V_m}{k_B T} (\delta_i - \delta_j)^2 \quad (2.2)$$

## 2.9 DPD Simulations

For DPD simulations, an oligomer chain architecture of A<sub>7</sub>(BD)A<sub>11</sub>(BD)A<sub>9</sub>(BD)A<sub>5</sub>(BD)A<sub>15</sub>(BD)A<sub>8</sub>(BD)A<sub>13</sub>(BD)A<sub>15</sub>(BD)A<sub>4</sub>(BD)A<sub>3</sub> was constructed according to the beads shown in Fig. 2.2. Cubic boxes having 10 x 10 x 10 $r_c^3$  volume are constructed with a density of  $\rho = 3$  DPD units where  $r_c$  is the cut-off radius. A harmonic spring constant of 4.0 was chosen between the beads. Temperature and bead masses were taken as unity for simplicity. Total number of all beads (including the solvents) were set to 3000. Simulations were carried out at a series of concentrations spanning 10-70 % of oligomer in the corresponding solvent systems. Equilibration of the oligomers and data collection were performed at 20000 and 100000 DPD steps, respectively.

# Chapter 3

## Results and Discussion

### 3.1 Bulk and Surface Properties of the Copolymer

Number average molecular weight and poly dispersity index of the copolymer were measured as 105,600 g/mol and 1.8, respectively. PFA concentration in the copolymer was calculated as 13 % by mole by  $^1\text{H-NMR}$ . AFM analysis revealed an average roughness of 0.6 nm on the surface of dip coated polymer films. This value is too small to affect the contact angles [98–100], thus any measurement would be a direct result of surface chemical groups.  $\theta_A$  was measured as  $118.5 \pm 0.5^\circ$  on this smooth surface. This relatively high value indicates the surface segregation of perfluoroalkyl groups on the outermost surface.

The selection of this polymer in this work has several reasons. In order to demonstrate that contact angle hysteresis on electrosprayed surfaces is governed by topography, we used the most hydrophobic polymer we could synthesize so that effect of surface chemistry would be minimum. It was not possible to electrospray a fully fluorinated homopolymer due to solubility problems, thus a copolymer of styrene and a perfluoroacrylate was a good selection for both considerations. 13 % fluorinated monomer ratio was the optimum composition because lower contents resulted lower  $\theta_A$  values whereas higher contents did not increase contact angles.

Table 3.1: Various parameters of the liquids used for electro spraying.

solvent	type	boiling point (°C)	surface tension (mN/m)
THF	good solvent	66	28.0
Chlorofom	good solvent	61	27.2
DMF	poor solvent	153	35.0
DMSO	poor solvent	189	43.7

## 3.2 A Foreword on the Wettability Measurements

On extremely hydrophobic surfaces, contact angles are close to  $180^\circ$  and precise measurement of contact angles is difficult [42, 44, 45]. Superhydrophobic surfaces we produce by electro spraying often exhibit extreme hydrophobicity but we can only perform contact angle analyses which are consistent within themselves. For instance, on the perfectly hydrophobic surfaces which will be described later in this work,  $\theta_A$  and  $\theta_R$  values measured with a conventional contact angle goniometer were always between  $160^\circ$  and  $170^\circ$ , being generally close to the latter with zero contact angle hysteresis. However, it was proved that these surfaces are indeed perfectly hydrophobic. Thus, contact angle measurements on these surfaces is controversial, and accordingly in this thesis, reporting  $\theta_A$  and  $\theta_R$  values was deliberately avoided but threshold sliding angles, which fundamentally become a function of mainly contact angle hysteresis for a constant droplet size according to Eq. (1.7), were used instead. This procedure indeed enables the measurement of shear hydrophobicity, commonly perceived as water repellency, and would not be sufficient to characterize the wettability of the surfaces completely [43]. Thus, the force required to separate a pendant superhydrophobic surface from a sessile droplet was also measured in order to compare the receding angles, in other words, the tensile hydrophobicity of a selection of surfaces.

## 3.3 Electro spraying the Copolymer in a Good Solvent

Electro spraying experiments started with three solutions of the copolymer in THF with concentrations 7, 4, and 1 wt%, which were electro sprayed using 8 kV applied voltage

and 2  $\mu\text{L}/\text{min}$  solution feed rate. SEM analysis revealed that all three surfaces were composed of dimpled beads having sizes at the micron scale, and average bead size increased with concentration, as shown in Fig. 3.1. Threshold sliding angles were  $9.6 \pm 2.5^\circ$ ,  $5.5 \pm 0.7^\circ$  and  $2.3 \pm 0.4^\circ$  for the surfaces from 7, 4 and 1 wt% concentrations, respectively. On these surfaces, triple interface occurs only on bead tops, thus continuity and amount of contact of the contact line decreases with smaller beads, resulting lower sliding angles. Further decrease of concentration to 0.7 and 0.4 wt% led to diminishing of roughness by the formation of plate-like beads, and sliding angles increased again. Bead formation did not occur by electro spraying of 0.1 wt% polymer solution and a slightly rough polymer film formed. Water droplets were pinned on this surface. Although a sliding angle value of  $2.3 \pm 0.4^\circ$  could be regarded as fairly low, these beaded surfaces would always exhibit some hysteresis due to the relatively smooth topography of the individual bead tops as stated earlier.

### **3.4 Electro spraying the Copolymer in a Poor Solvent**

DMF has become a conventional solvent for electro spraying various polymers not only due to its ability to dissolve common polymers, but also because of its high surface tension and low boiling point which provide the control of the process relatively easy. For the copolymer in this work, however, the solubility was 0.15 wt% in DMF, and achieving a decent coating for wettability measurements could take as long as 12 hours. Electro spraying the copolymer in this poor solvent yielded the surface shown in Fig. 3.2. This type of surface is not common in electro spraying of polymers and the nanoparticles do not seem to refer to the classical micron scale electro sprayed beads generally observed in the process. Possible reasons for the formation of this topography will be discussed in Section 3.9. Threshold sliding angle on this nanoscopically rough surface was measured as  $2.6 \pm 0.5^\circ$ .

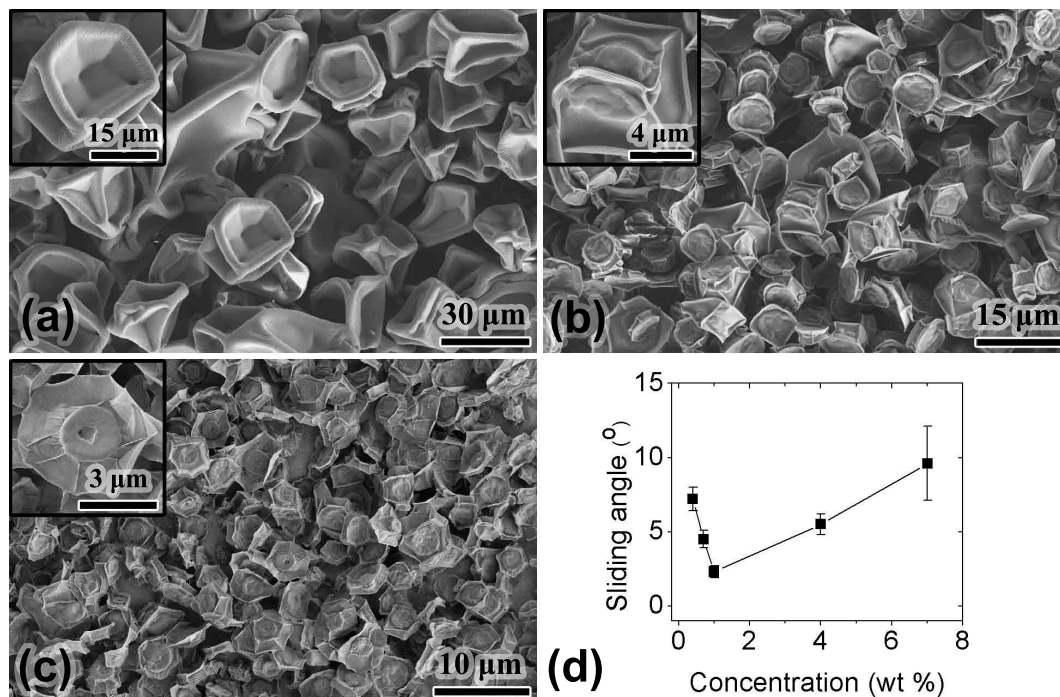


Figure 3.1: Typical SEM images of the electrospayed surfaces from solutions having (a) 7 wt%, (b) 1 wt%, and (c) 0.4 wt% polymer concentration in THF. Applied voltage and solution feed rate were 8 kV and 2  $\mu\text{L}/\text{min}$  for all samples, respectively. (d) Sliding angle vs. polymer concentration in THF for a 10  $\mu\text{L}$  water droplet.

### 3.5 Electrospaying the Copolymer in a Binary Good Solvent-Poor Solvent System

A threshold sliding angle of  $2.3^\circ$  might well be considered as relatively small for a 10  $\mu\text{L}$  droplet, yet it implies a positive contact angle hysteresis even if Eq. (1.7) would predict a small value. As described in Section 1.8, one method to reduce contact angle hysteresis is increasing the receding angle of the local protrusion tops [42] and achieving the *Lotus effect* which is commonly described in terms of *dual scale roughness*. Although it is difficult to make precise definitions related to roughness for complex topographies, dual scale roughness has become a common term to simply describe the existence of nanoscopic roughness on the micron scale rough topography as depicted in Fig. 3.3. The advantage of such topography is that amount of contact is reduced on the protrusion tops and the contact line is de-pinned (which is macroscopically observed as high re-

ceding angles), therefore receding can occur spontaneously. Previously, superhydrophobic surfaces were successfully prepared from various polymers via non-solvent induced phase separation which provided the formation of proper surface roughness [101–104]. These methods were based on casting a polymer solution on a substrate and preventing homogenous solidification with the help of liquid or vapor phase non-solvents, which however did not allow sufficient control of the roughness scales and resulted surfaces with contact angle hysteresis (except the one [101] for which there is no information about dynamic angles). Two other papers also describe the application of a similar method to electrospinning which led to formation of highly porous, micron diameter fibers having considerable amount of porosity [105,106]. Although these studies were not related to wettability, one would not expect zero contact angle hysteresis on such topographies due to the continuous nature of the micron fibers. Inspired by these studies, we performed experiments with non-solvents such as water and alcohols but always encountered immediate precipitation of the polymer even by small additions to the solutions. On the other hand, when poor solvents such as DMF and DMSO (polymer solubility < 0.15 wt%) were used instead, stable solutions at relatively high

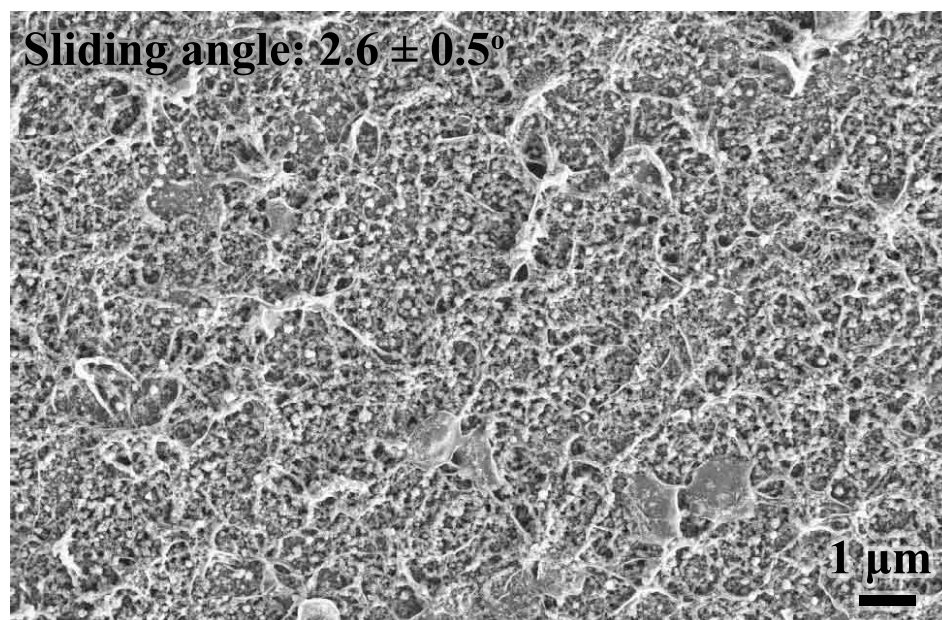


Figure 3.2: Typical SEM images of the electrospayed surfaces from solutions having 0.15 wt% polymer in DMF.

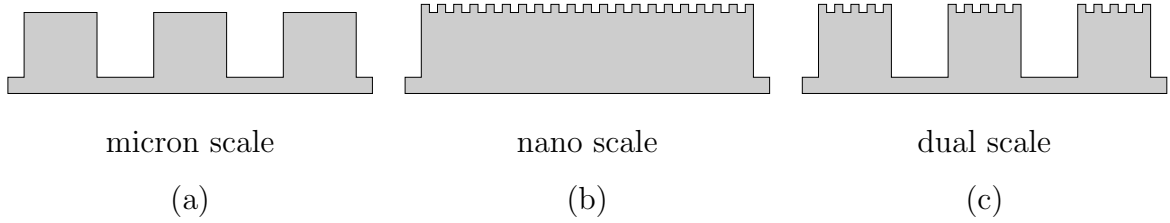


Figure 3.3: Depictions of different roughness scales related to wettability. (a) Micron scale roughness, (b) nano scale roughness, and (c) dual scale roughness.

poor solvent/good solvent ratios could be achieved. Accordingly, a 1 wt% solution of the copolymer was prepared in 75/25 (wt/wt) THF/DMF mixture and electrospayed at the same conditions as those employed for THF solutions (i.e. 8 kV applied voltage and 2  $\mu\text{L}/\text{min}$  feed rate). This process resulted a surface composed of flower-like beads having roughly 4  $\mu\text{m}$  diameter as shown in Fig. 3.4(a). Center of the beads was covered with about 100 nm size particles spread over a 2  $\mu\text{m}$  diameter circular area, and the remaining outer part was formed of relatively smooth films, resembling leaves. Formation of the nanoparticles on the center of the beads clearly implies a phase separation of the polymer in the poor solvent, induced by different evaporation rates of THF and DMF (Table 3.1). It is evident from the arrangement of these beads (nearly all the flowers face upwards) that unlike the electrospayings in THF, collapse of the skin layer and formation of the flower shape occur after the droplets reach the collecting screen. Otherwise, aerodynamic flow would force the beads to orient their edges perpendicular to the screen, so a more random distribution of bead placements, leaf crosssections and even bended leaves would be observed. Therefore, slower removal of DMF from the surface of droplets definitely leads to a relatively flexible, thin skin layer which can collapse uniformly when the droplet hits the grounded screen. Outer regions of this skin readily forms the thin leaf structure while the core is DMF rich and takes more time to dry completely by the diffusion of the solvent to the surface of the bead. Thus, the solidification of the core occurs substantially in the poor solvent environment and phase separation of the polymer due to concentration increment drives the formation of the nanoparticles. This process is depicted in Fig. 3.6(b). A similar process in fact occurs during electrospaying of the polymer in THF at very low



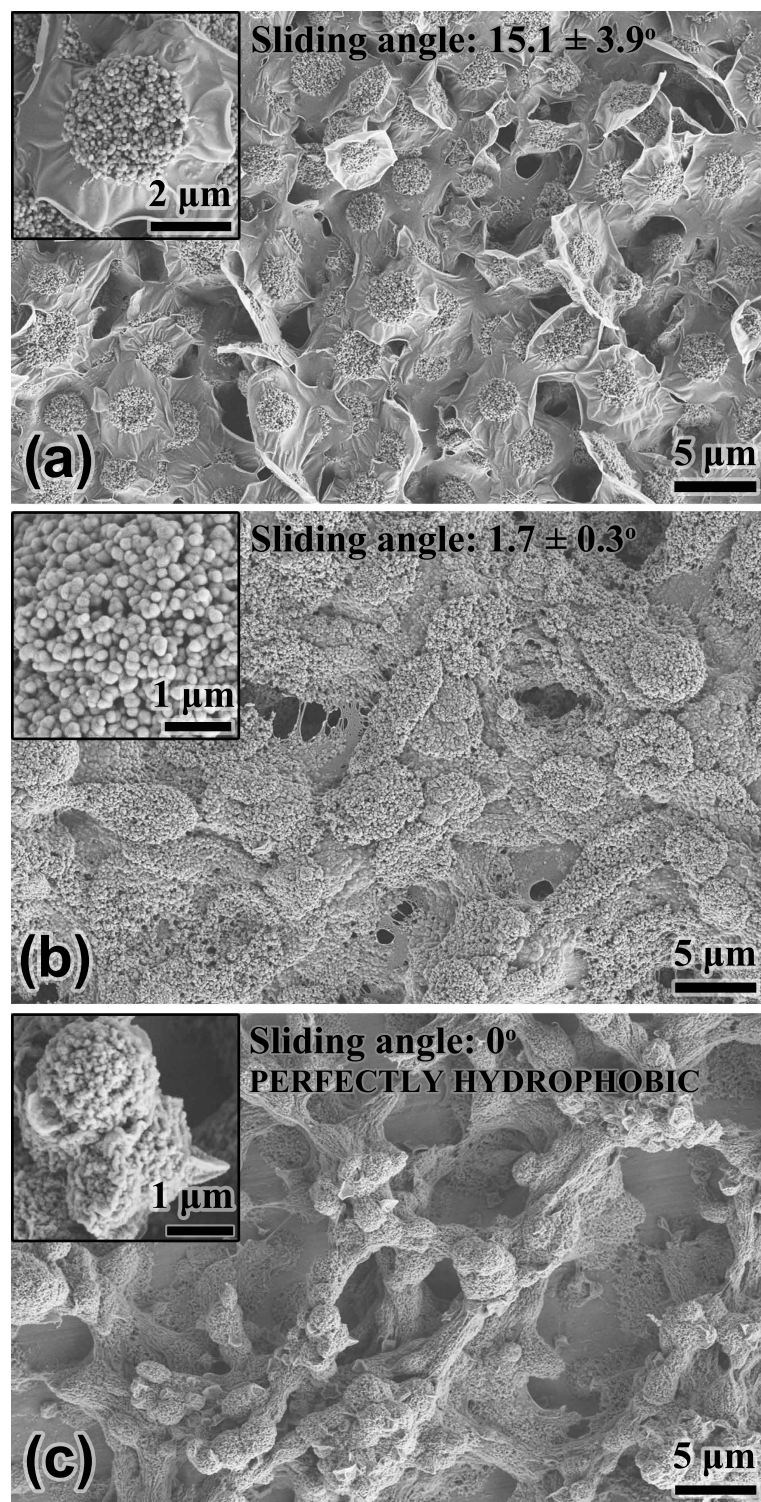


Figure 3.4: Typical SEM images of the electrospayed surfaces from 1 wt% polymer solutions in 75/25 (wt/wt) THF/DMF mixture. (a) 8 kV and 2  $\mu\text{L}/\text{min}$ , (b) 15 kV and 15  $\mu\text{L}/\text{min}$ , and (c) 15 kV and 15  $\mu\text{L}/\text{min}$  applied voltage and solution feed rate, respectively. Coating time is shorter (30 seconds) for (c).

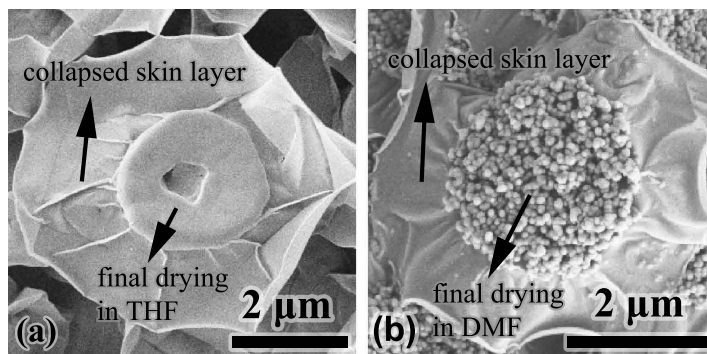


Figure 3.5: High magnification images of the flower-like structures shown in (a) Fig. 3.1(c), and (b) Fig. 3.4(a).

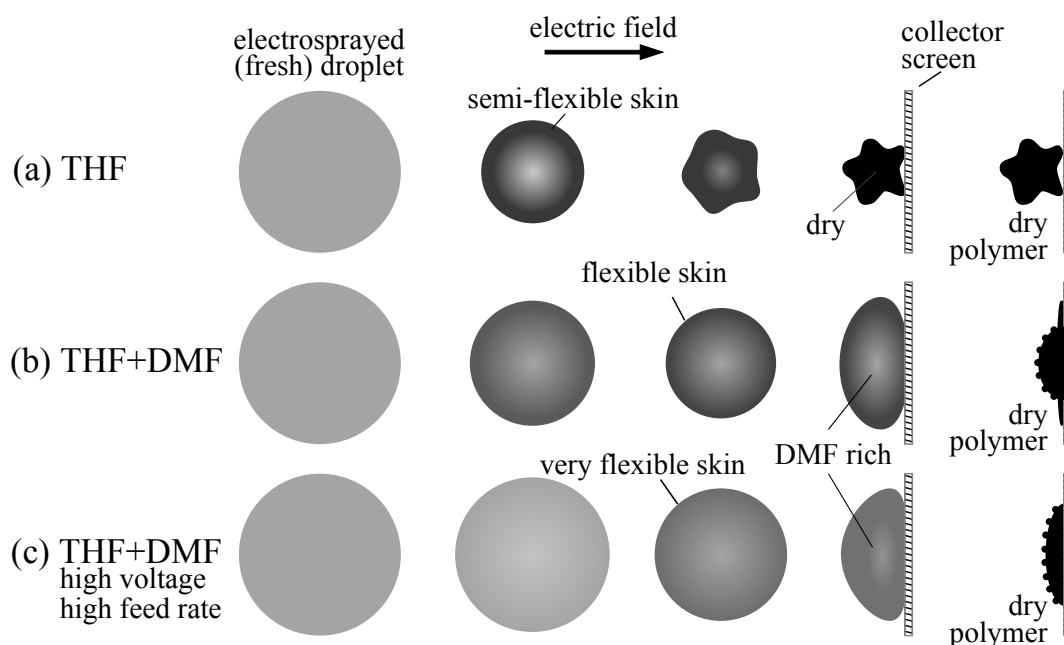


Figure 3.6: Schematic demonstration of bead formation during electrospinning of polymer solutions at different conditions. Light and dark regions represent solvent and polymer rich phases, respectively.

concentrations where the deficiency of polymer in the system leads to formation of a flexible skin which may collapse to form the leaf structure; however, the core is rich in the good solvent, therefore nanoscale roughness is not expected to occur. For a better comparison, high magnification images of the two flower-like structures are shown in Fig. 3.5. Threshold sliding angle on the surface composed of flower-like beads (Fig.

3.4(a)) was measured as  $15.1 \pm 3.9^\circ$ . This relatively high value is claimed to originate from the smooth nature of the leaf-like regions on which segments of the contact line is predicted to have high amount of contact due to continuity. In addition, two dimensional distribution of the beads (flowers) contributes to the energy barrier to receding due to the formation of a shorter contact line as a whole. Thus, removal of these leaf structures would obviously facilitate receding, and a method to achieve this must aim retarding the skin formation by slowing down the solvent evaporation and inducing a solidification in a predominantly poor solvent environment. This was accomplished by applying a higher voltage to speed up the droplets and a higher solution feed rate to increase the number of droplets generated per unit time so that they spend less time in the air and form a wet coating once they reach the collector. Electro spraying at 15 kV voltage and 15  $\mu\text{L}/\text{min}$  feed rate resulted a macroscopically wet coating which required additional 5-10 minutes to dry completely on the collector. SEM analysis of this coating showed that the surface was covered with about 100 nm particles everywhere as shown in Fig. 3.4(b). Traces of the droplets are visible as flat, interconnected beads. These morphologies reveal that in the course of spraying, since there is not sufficient time for drying, a very flexible, immature skin forms on the surface of the droplets, and upon hitting the screen, droplets collapse by forming a negligible or no leaf structure at all as depicted in Fig. 3.6(c). When many droplets are collected on the screen, they interconnect due to their rather wet nature. However, it is evident from the cluster of nanoparticles that an efficient integration of the droplets cannot realize presumably due to the existence of a skin although immature. Final evaporation of the poor solvent occurs as a concerted event among the droplets leaving a nano particle rich surface behind. Some broken loose connections due to the shrinkage of the polymer during drying are also visible. Sliding angle on this surface was  $1.7 \pm 0.3^\circ$ . Compared to the surfaces prepared by electro spraying THF solutions, nanoscopic roughness was achieved but the level of micron scale roughness was low this time due to the flat and interconnected nature of the beads on which length of the contact line is reduced. Electro spraying at higher voltages and solution feed rates all resulted similar surfaces having sliding angles between  $1^\circ$  and  $2^\circ$ .

### 3.6 The Route to Zero Hysteresis

The efforts to achieve dual scale roughness succeeded when the coating time was kept relatively short (30 seconds) so that only local interconnection of the beads occurs because of the uncoated regions of the aluminum substrate as shown in Fig. 3.4(c). The sliding angle on this surface was  $0^\circ$  where it was impossible to mobilize any droplet of varying sizes on horizontally leveled surfaces. On this surface a very lengthy, discontinuous contact line having quite scarce amount of contact with the solid is predicted. Electro spraying at higher voltages and solution feed rates with short coating times also resulted surfaces having similar topographies and zero sliding angles. This result is essentially a matter of topographic length scales and was witnessed long ago on photolithographic superhydrophobic surfaces on which increasing the spacing between the regular posts resulted remarkable increase in receding angles [31]. Water droplets benefit from the lengthy liquid-vapor interface between the protrusions of micron scale roughness, where the nanoscopic features contribute to the discontinuity of the contact on the protrusion tops and promote receding locally. The uncoated regions of the substrate cannot affect the results presented here at atmospheric pressures because any water intrusion would require a huge laplace pressure to overcome the negative capillary pressure driven by the hydrophobicity of the polymer and the mesoscale roughness. This is also to indicate that all of the surfaces described in this study are in composite wetting state.

To verify the claim regarding the effect of phase separation due to inhomogeneous drying in good solvent-poor solvent environment, other experiments were performed by changing the good and poor solvents. Replacing THF with another good solvent, chloroform, did not change the results remarkably. Electro spraying a 1 wt% copolymer in chloroform at 8 kV applied voltage and  $2 \mu\text{L}/\text{min}$  feed rate resulted micron scale beads as shown in Fig. 3.7(a), similar to those achieved from THF solutions. Sliding angle on this surface was  $3.4 \pm 0.3^\circ$ . When 75/25 (wt/wt)chloroform/DMF solution was employed instead and electro sprayed at 15 kV and  $15 \mu\text{L}/\text{min}$  by keeping the coating time short, a surface having a dual scale roughness as shown in Fig. 3.7(b) is achieved.

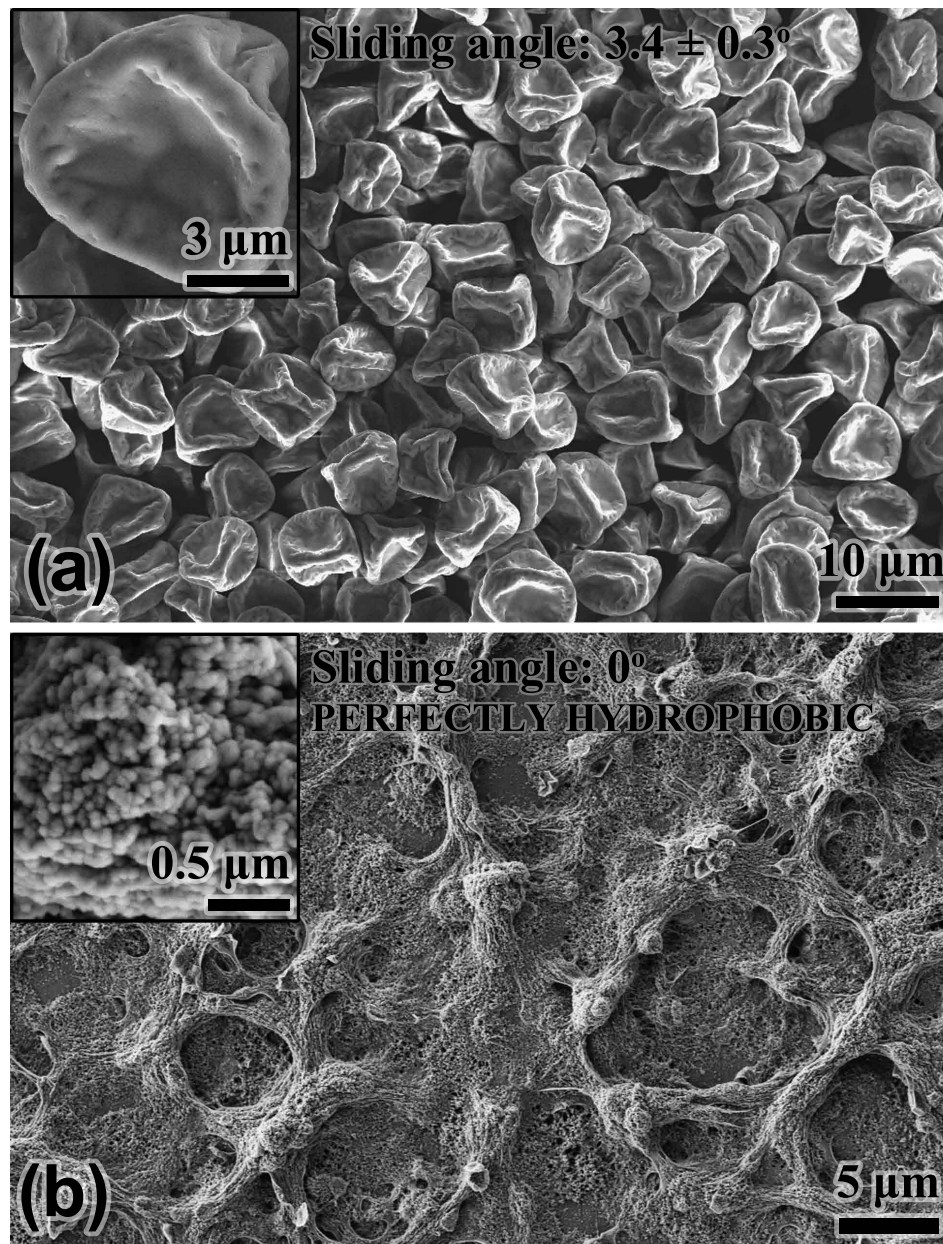


Figure 3.7: Typical SEM images of the electrospayed surfaces from 1 wt% polymer solutions in (a) Chloroform (8 kV applied voltage and  $2 \mu\text{L}/\text{min}$  solution feed rate), and (b) 75/25 (wt/wt) chloroform/DMF mixture (15 kV applied voltage,  $15 \mu\text{L}/\text{min}$  solution feed rate, 30 seconds coating time).

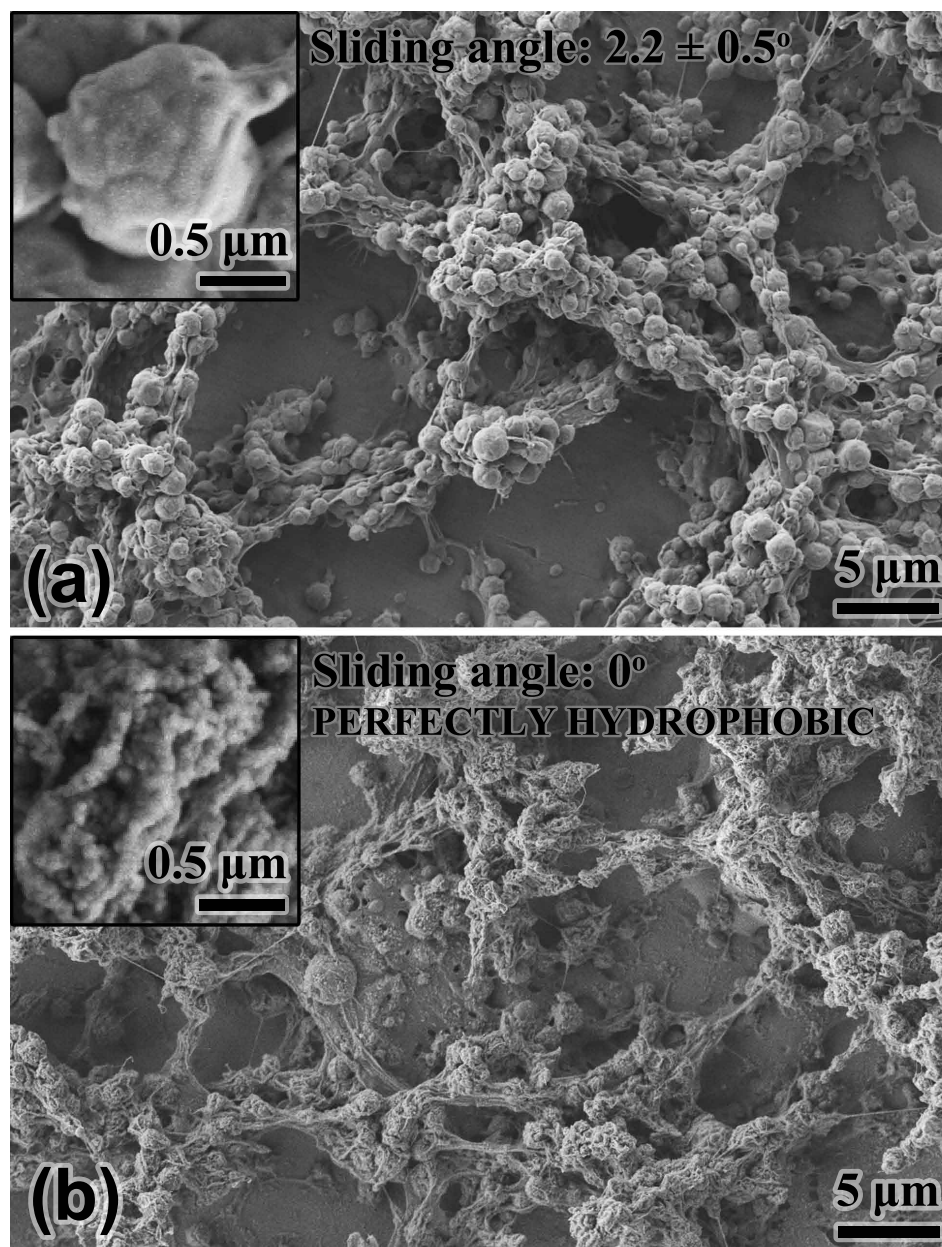


Figure 3.8: Typical SEM images of the electrospayed surfaces from 1 wt% polymer solutions in (a) 75/25, and (b) 50/50 (wt/wt) THF/DMSO mixture. Process parameters are 8 kV applied voltage, 2  $\mu\text{L}/\text{min}$  solution feed rate and 30 seconds coating time for both samples.

This surface is similar to the one shown in Fig. 3.4(c) and sliding angle on this surface was also  $0^\circ$ .

Replacing DMF with another poor solvent, DMSO, and electrospaying at 15 kV and

15  $\mu\text{L}/\text{min}$  by keeping the coating time 30 seconds, resulted a surface resembling the one shown in Fig. 3.4(c) in the micron scale, but with relatively smooth bead surfaces this time (Fig. 3.8(a)). Sliding angle on this surface was  $2.2 \pm 0.5^\circ$ . Increasing the DMSO mass ratio from 0.25 to 0.5 in the binary solvent system and electrospaying at same conditions resulted a zero hysteresis surface by the formation of nanoscale roughness on the beads as shown in Fig. 3.8(b). This experiment was in good accordance with the claim regarding the necessity of nanoscopic roughness on the micron scale features to achieve a zero hysteresis surface. In terms of the effect of the solvent ratios, a similar observation was also reported by Qi *et al.* [105] as the decrease in the poor solvent ratio of the solvent system gradually reduced the porosity of the electrospun microfibers.

### **3.7 Contact and Release Experiment: Proof of Perfect Hydrophobicity**

Finally, to characterize the tensile hydrophobicity of the surfaces reported so far, droplet videos recorded during a contact and release experiment were investigated. This process allowed the qualitative comparison of receding angles from the degree of distortion of the droplet shapes (more distortion indicates lower receding angles) [44, 45]. Experiments showed that nanoscopic (Fig. 3.4(b)) and micron scale (Fig. 3.8(a)) roughness dominated topographies stick to water slightly, as it is clear from the distortion of the spherical droplet shapes followed by surface tension driven vibration due to the sudden relaxation of the droplet to its thermodynamic shape at the vicinity of release from the surface. On the other hand, there was no evidence (no distortion and vibration) of adhesion when the droplets were released from the surfaces having dual scale roughness. Selected frames from this experiment are given in Figures 3.9-3.12. These results implied a  $180^\circ$  receding angle for the dual scale rough surfaces and thus, they were regarded as perfectly hydrophobic. Selected frames of contact and release experiments with other surfaces are given in Section A.1.



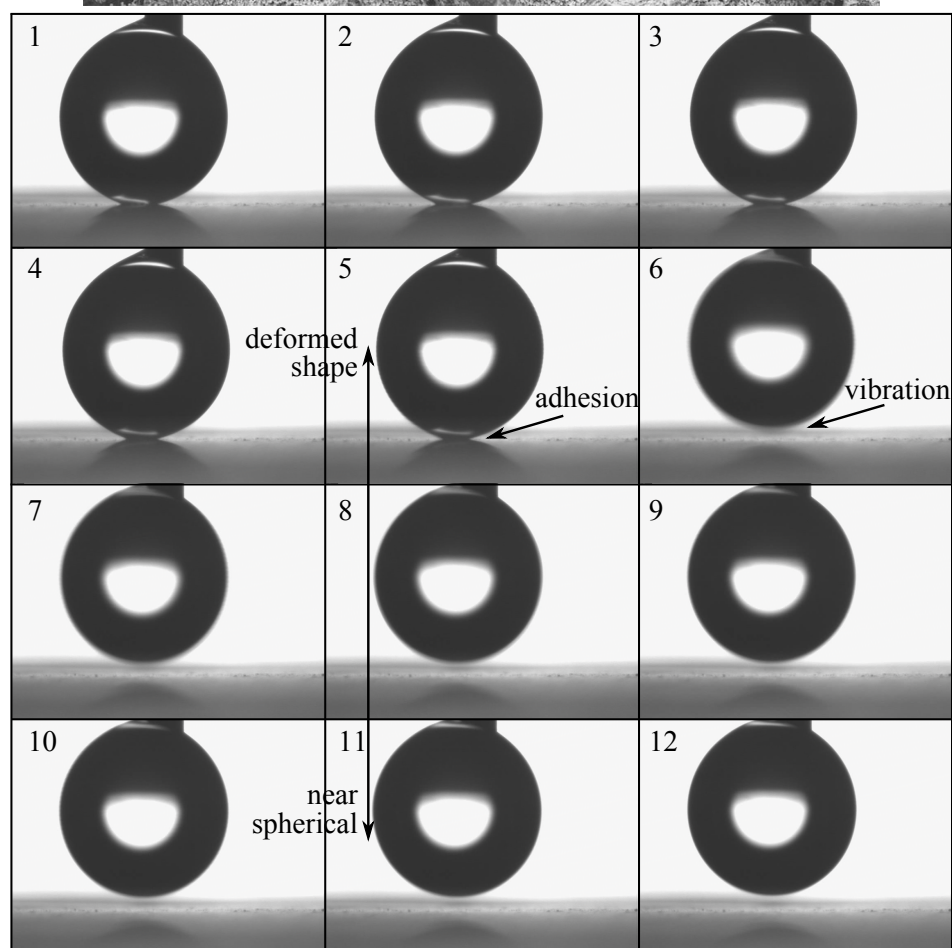
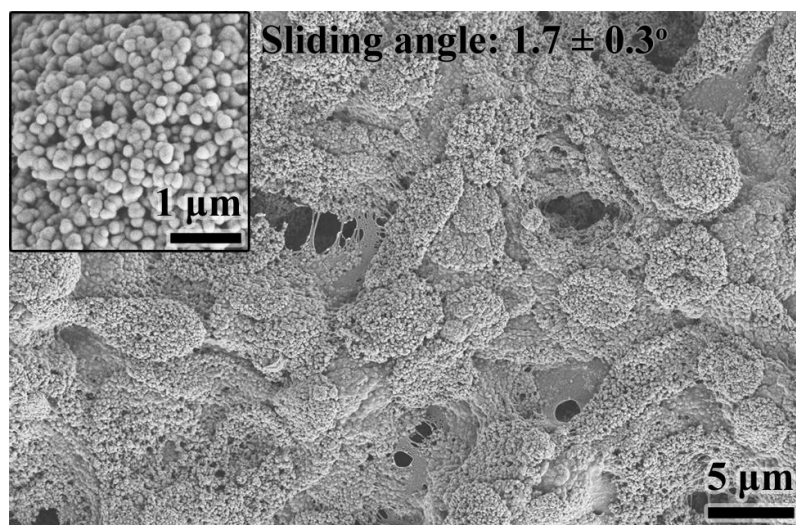


Figure 3.9: Selected frames of the contact and release experiment performed with the surface having nanoscale roughness dominated topography shown in Fig. 3.4(b).



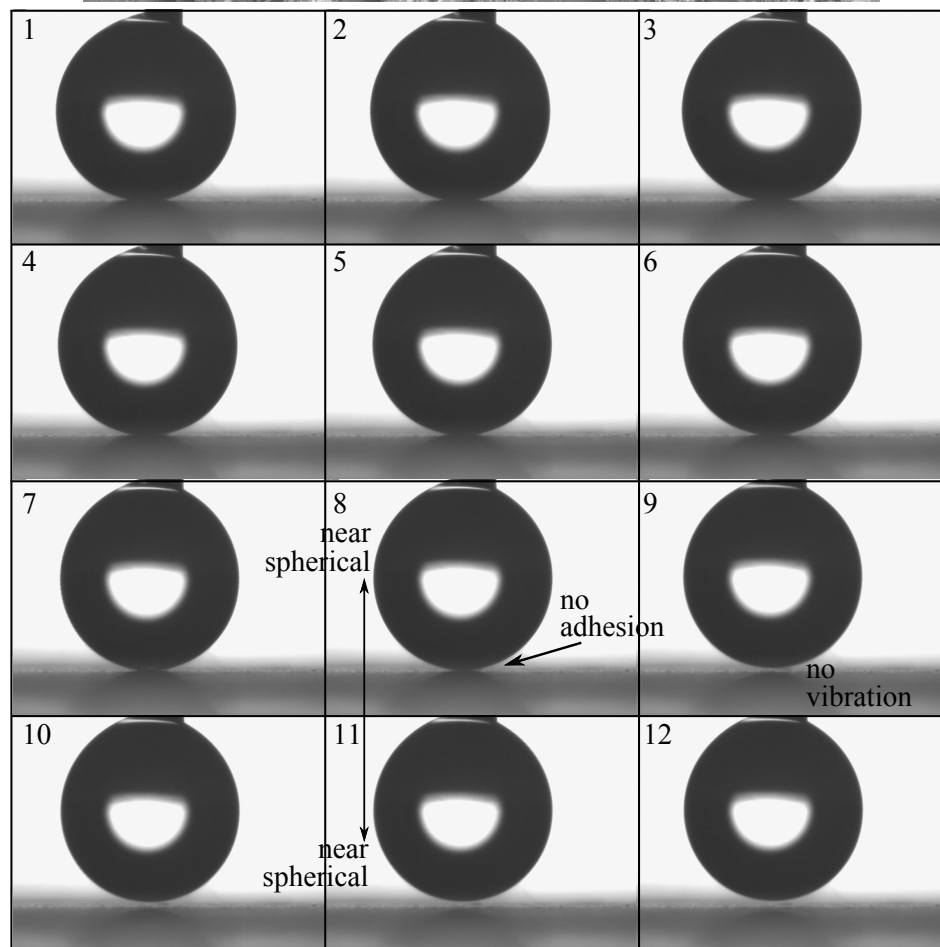
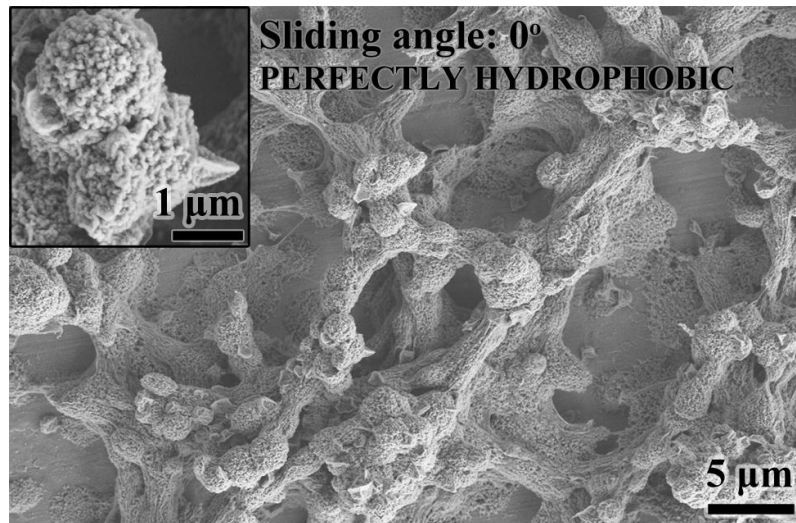


Figure 3.10: Selected frames of the contact and release experiment performed with the surface having dual scale rough topography shown in Fig. 3.4(c).

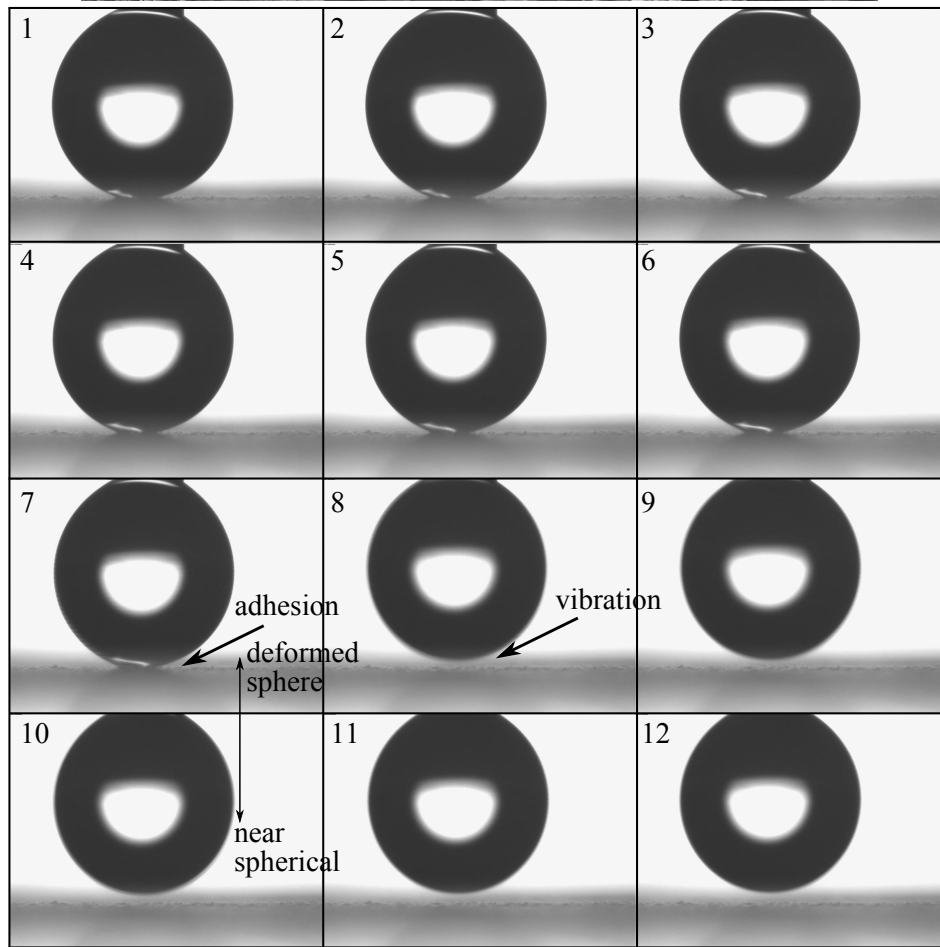
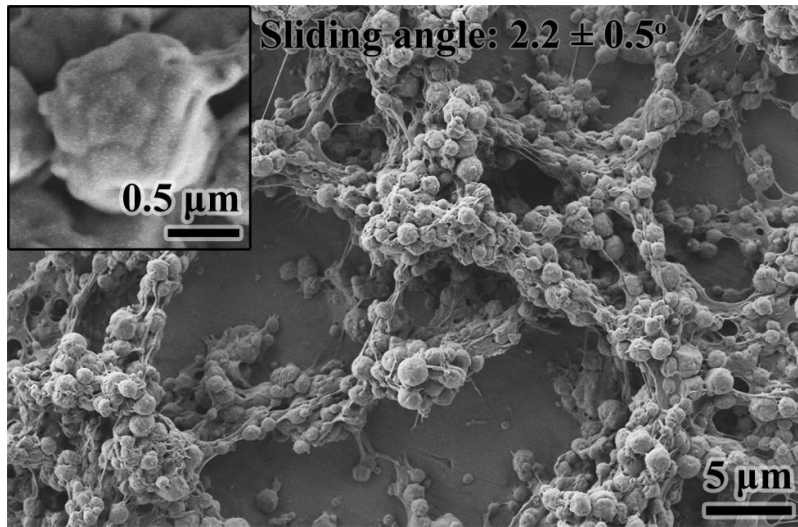


Figure 3.11: Selected frames of the contact and release experiment performed with the surface having micron scale roughness dominated topography shown in Fig. 3.8(a).

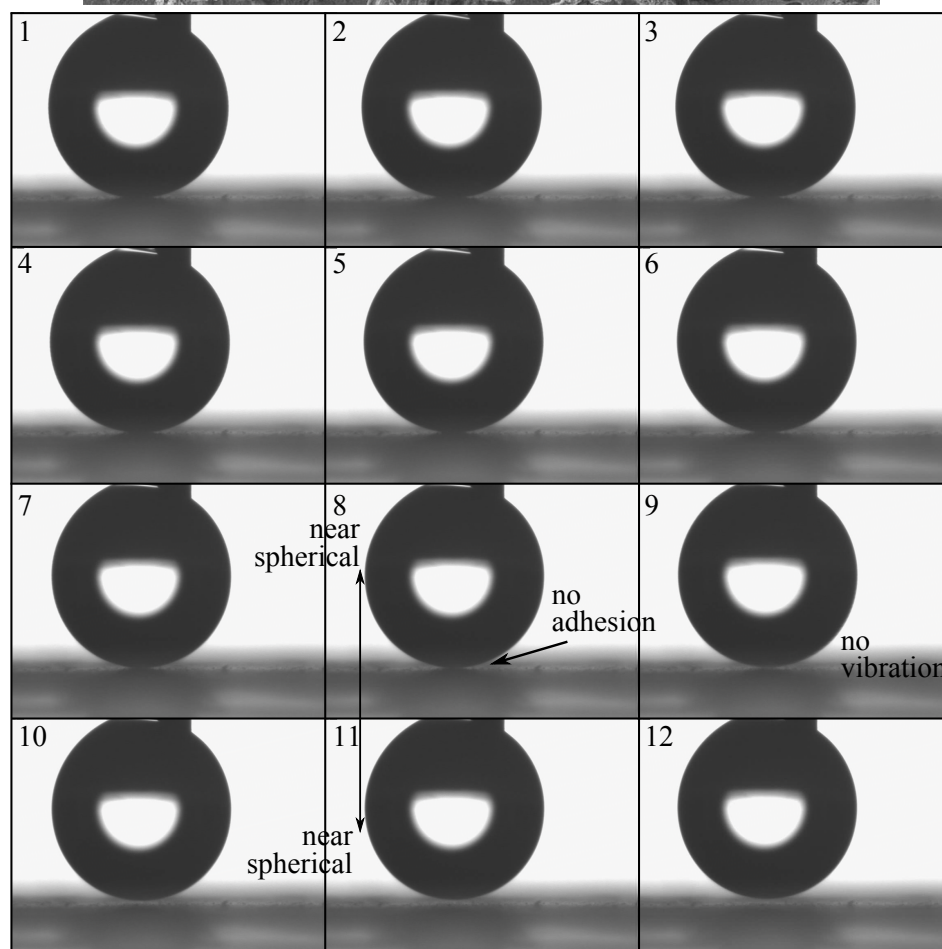
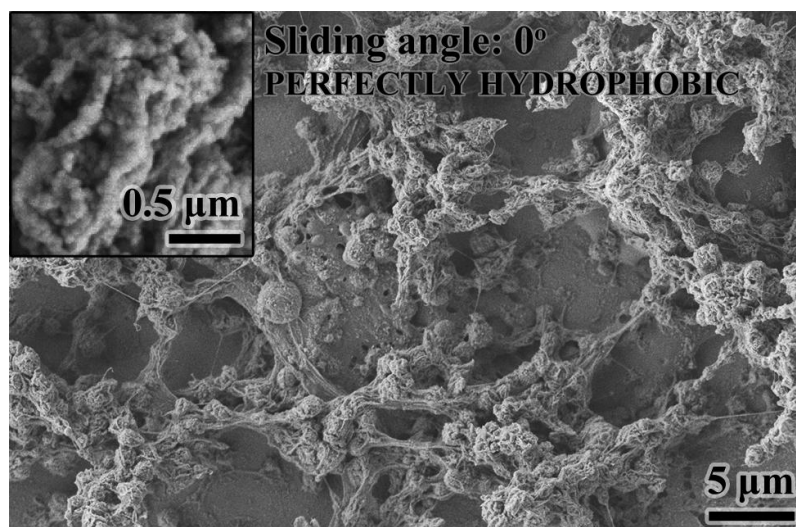


Figure 3.12: Selected frames of the contact and release experiment performed with the surface having micron scale roughness dominated topography shown in Fig. 3.8(b).



In addition, the adhesive forces between the droplets and surfaces were measured using a microbalance as previously described elsewhere [107,108] with a small difference in the experimental set-up and procedure where a pendant superhydrophobic surface is separated from a sessile droplet as depicted in Fig. 3.13. In this experiment, initially a  $60 \mu\text{L}$  sessile droplet was deposited on a polymer film having  $107^\circ/80^\circ \theta_A/\theta_R$ . Contact angle of this droplet was decreased by withdrawing  $20 \mu\text{L}$  water with a microsyringe so that the three phase contact line does not advance on the lower film surface easily when the droplet is pressed. The microbalance was zeroed after the superhydrophobic surface was attached to its probe. The sessile droplet was raised upwards and the position of the lower plate was automatically set to zero when the droplet and the surface were in contact for the first time. The droplet was pressed by raising the lower plate  $0.4 \text{ mm}$  (shown as  $-0.4 \text{ mm}$  distance in Fig. 3.14). Then, the force versus displacement was being recorded while the lower plate was lowered  $0.8 \text{ mm}$  and brought to  $0.4 \text{ mm}$  distance. The analysis performed with a selection of samples showed that the forces acting on the dual scale rough surfaces while the droplet was being released from the surface were zero, as shown in Fig. 3.14, indicating a zero work of adhesion. In addition, variations in the measured force at the vicinity of maximum pressure (i.e.  $-0.4 \text{ mm}$  distance) revealed that the structure of the roughness may also affect the compressibility of the droplets on the surfaces. For instance, it is possible that the air-liquid interface under a droplet is bent more efficiently towards the valleys on a micron scale rough surface than a predominantly nanoscale rough surface due to the difference in the distances between the protrusions. However, this claim definitely cannot be proved unless the advancing angles of these surfaces are measured precisely because differences in the advancing characteristics of the droplets would also affect the compressibility (i.e. a higher  $\theta_A$  would imply a higher Laplace pressure).

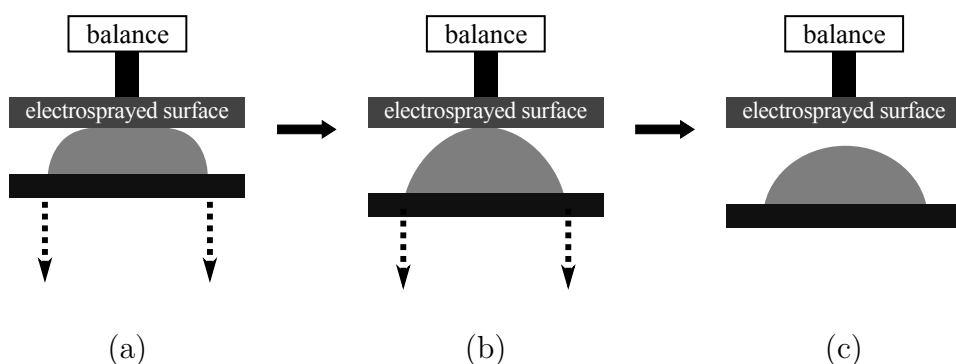


Figure 3.13: Pictorial presentation of the experiment performed to measure the adhesive forces during the release of a droplet from a superhydrophobic surface. (a) A previously pressed droplet is being released, (b) adhesion (if exist) causes deformation of the droplet from its thermodynamical shape, and (c) droplet and the surface are separated.

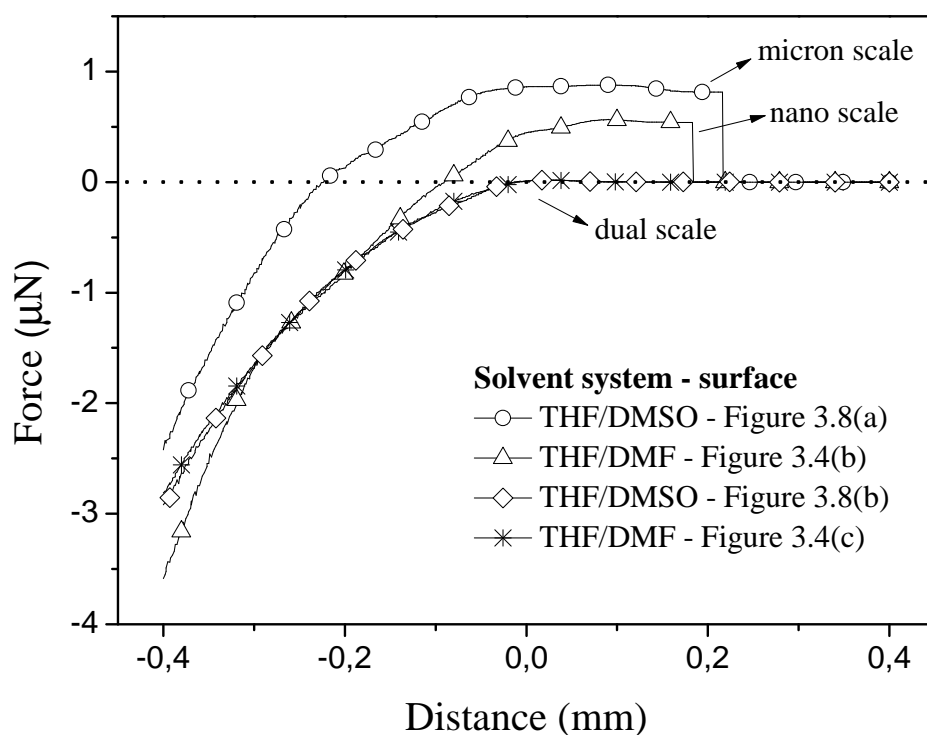


Figure 3.14: Force required to separate a superhydrophobic surface from a droplet for samples having micro, nano and dual scale roughness during the experiment depicted in Fig. 3.13. 0 mm distance refers to the position when the droplet and the surface were in contact for the first time. Negative and positive distances correspond to raising and lowering the lower plate from this 0 displacement, respectively.

### 3.8 Some Remarks on the Described Method

The selection of the particular polymer used in this work had several reasons as stated earlier. On the other hand, it was possible to produce similar surfaces with the same type of copolymers having less perfluoroacrylate content or different perfluoroalkyl group, and copolymers of the perfluoroacrylate with methyl methacrylate and glycidyl methacrylate. Electrospraying of these polymers from the binary solvent systems indicated in this work always resulted nano scale roughness on the micron size beads. We could also achieve perfect hydrophobicity with these polymers but the optimum process and solution conditions varied. For instance, for the copolymers of the fluoroacrylate with methyl methacrylate, lower solution feed rates are required during electrospraying because if the coating gets too wet, a film occurs instead of a rough surface, probably due to the higher solubility of the polymer in the poor solvent. Also, for the styrene-perfluoroacrylate copolymers, when *N*-methyl-2-pyrrolidone was used as the high boiling point poor solvent for instance, the whole surface of the beads were always covered with nano scale roughness, but we could not achieve perfectly hydrophobic surfaces since we somehow could not succeed in the formation of clustered beads (yet). Also, for the copolymers of the fluoroacrylate with acrylonitrile, DMF and DMSO are the good solvents, THF and chloroform are the poor solvents this time, and the beads do not exhibit nanoscale roughness when electrosprayed from the good solvent-poor solvent combinations of these solvents. These examples conclude that nanoscale roughness occur on the micron scale beads as long as the high boiling point liquid in the solution is the poor solvent; but finding the optimum electrospraying process and solution conditions which would result ‘islands of clustered beads separated from each other by uncoated regions’ is more challenging, and may or may not exist for some other selections of polymer and solvent systems. The perfluoroacrylate may have an important effect in determining the solubilities of the copolymers and facilitate the formation of nanoscale roughness. Examples of the surfaces in different systems are shown in Section A.2.

### 3.9 Computational Analysis

As the methodology required, the computational analysis started by calculating the Hildebrand solubility parameters,  $\delta$ , which is a good numerical reference for the degree of interaction between molecules.  $\delta$  can be used to predict whether a molecule is miscible with another such that close values of  $\delta$  imply good miscibility between the two molecules and vice versa.  $\delta$  is fundamentally equal to the square root of *cohesive energy density*, the expression in brackets in Eq. (2.1), which refers to the the energy required to remove unit volume of molecules from their nearest neighbors to infinite separation. Thus,  $\delta$  is an indicator of the degree of van der Waals forces holding the molecules together.  $\delta$  values calculated according to Eq. (2.1) for the DPD beads depicted in Fig. 3.15 are given in Table 3.2. Close values of  $\delta$  for the bead pairs A, B and  $S_1$  make them miscible with each other. The solubility value of bead C is distinct from all other beads, particularly from the bead  $S_2$ . These data are in good accordance with the solubility results we achieved experimentally where the copolymer is found to be rather soluble in THF (>30 wt%) but has very low solubility in DMF (0.15 wt%). Therefore, although it is apparent that the interaction between segments C and  $S_2$  is too weak, high ratio of the monomer styrene in the copolymer (87 mol% on the average) determines DMF as a poor solvent instead of a non-solvent.

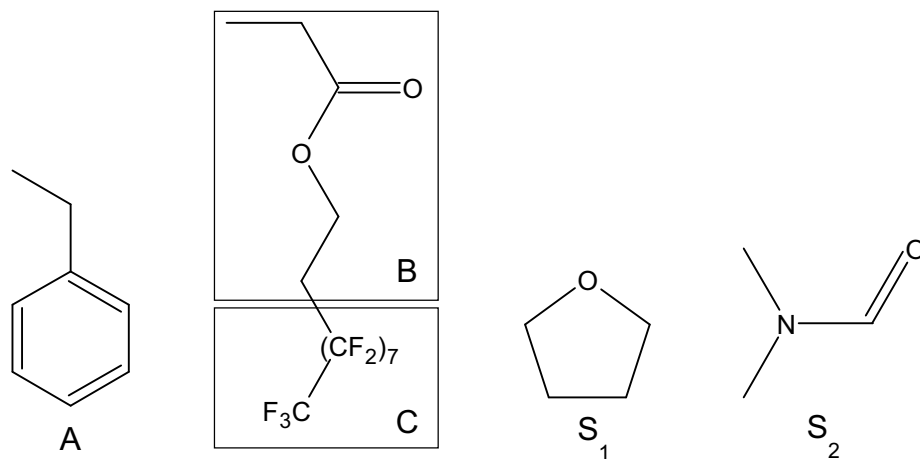


Figure 3.15: Partitioning of the beads for coarse-grained simulations. Replication of Fig. 2.2.

Table 3.2: Solubility parameters,  $\delta$  ( $(cal/cm^3)^{1/2}$ ), and molar volume  $V_m$  ( $cm^3/mol$ ) of the beads.

Property	A	B	C	S <sub>1</sub>	S <sub>2</sub>
$\delta$	7.99	9.33	3.92	9.31	12.29
$V_m$	115.3	109.6	166.4	79.7	83.0

The Flory-Huggins interaction parameter,  $\chi$ , is related to thermodynamics of mixing, and calculated from the Hildebrand solubility parameters according to Eq. (2.2). DPD interaction parameter,  $a$ , calculated from  $\chi$ , is a measure of repulsion between the clusters of atoms, i.e. beads. Both interaction parameters are listed in Table 3.3. We found that the interaction between beads A and S<sub>1</sub> is nearly neutral, and C and S<sub>1</sub> is repulsive. On the other hand, repulsion is moderate between A and S<sub>2</sub> but very strong between C and S<sub>2</sub>. These results already indicate a possible phase separation between the fluorinated segment and DMF, however, whether the overall, concerted behavior of the chains would yield a segregation or not is too early to comment without DPD simulations. Electrospinning is fundamentally a type of dry-spinning where the diffu-

Table 3.3: Flory-Huggins interaction parameters,  $\chi_{ij}$ , and DPD interaction parameters,  $a_{ij}$ .

	A	B	C	S <sub>1</sub>	S <sub>2</sub>
A	0.00 ( $\chi_{ij}$ ) 25.00 ( $a_{ij}$ )	0.29	4.10	0.21	3.09
B	25.95	0.00 ( $\chi_{ij}$ ) 25.00 ( $a_{ij}$ )	7.24	0.00	1.42
D	38.42	48.69	0.00 ( $\chi_{ij}$ ) 25.00 ( $a_{ij}$ )	3.45	14.75
S <sub>1</sub>	25.67	25.00	36.27	0.00 ( $\chi_{ij}$ ) 25.00 ( $a_{ij}$ )	1.22
S <sub>2</sub>	35.13	29.66	73.25	29.00	0.00 ( $\chi_{ij}$ ) 25.00 ( $a_{ij}$ )



sion of solvent to the atmosphere takes place while the solution travels rapidly from the spinneret towards the collector. In order to interpret the hydrodynamic changes that occur during this drying process, we performed simulations comprising various polymer concentrations from 10 to 70 mol% in THF and DMF. It is important to note that these simulations cannot represent the drying process that occur during electrospinning exactly since the achieved morphologies are of equilibrium conditions. A selection of the obtained mesoscopic morphologies is shown in Fig. 3.16. In dilute THF solutions, the polymer forms a relatively homogenous solution with the solvent THF. This homogeneity is maintained at high polymer concentrations (Fig. 3.16(a)). On the other hand, the polymer undergoes phase separation even at low concentrations in the simulations performed in DMF (Fig. 3.16(b)). Formation of spherical structures is observed in dilute solutions and the morphology changes into rod-like and lamellar geometries, respectively, with the increase in polymer concentration. Finally at high concentrations, the solvent is entrapped by the polymer as a distinct phase. It is important to understand the mechanism of the electrospinning process to establish a relation between the experimental and computational results. As mentioned previously, electrospinning involves drawing an electrically charged jet of polymer solution towards a grounded collector and formation of nano or microfibers upon elongation and thinning of this jet prior to solidification. When the solution viscosity is low, however, the deficiency of chain entanglements drives the solution jet to breaking up into spherical droplets which generally form micron size beads upon drying as shown in Fig. 1.15. Accordingly, the morphologies shown in Fig. 3.16(a) indicate that while the good solvent THF evaporates from the electrospayed droplets, the polymer chains entangle without phase separation. While the droplets disintegrate from the semidilute solution jet and travel towards the collecting screen, the entanglement concentration is crossed initially on the surface of the droplets, due to the fast evaporation of the solvent from this region. This event leads to the formation of a skin layer, and a concentration gradient from the center to the surface of the droplets. The skin cannot solidify completely until all the solvent diffuse from the core to the skin of the droplets. This solidification process occur in a cooperative environment, where the degree of interaction between the polymer and

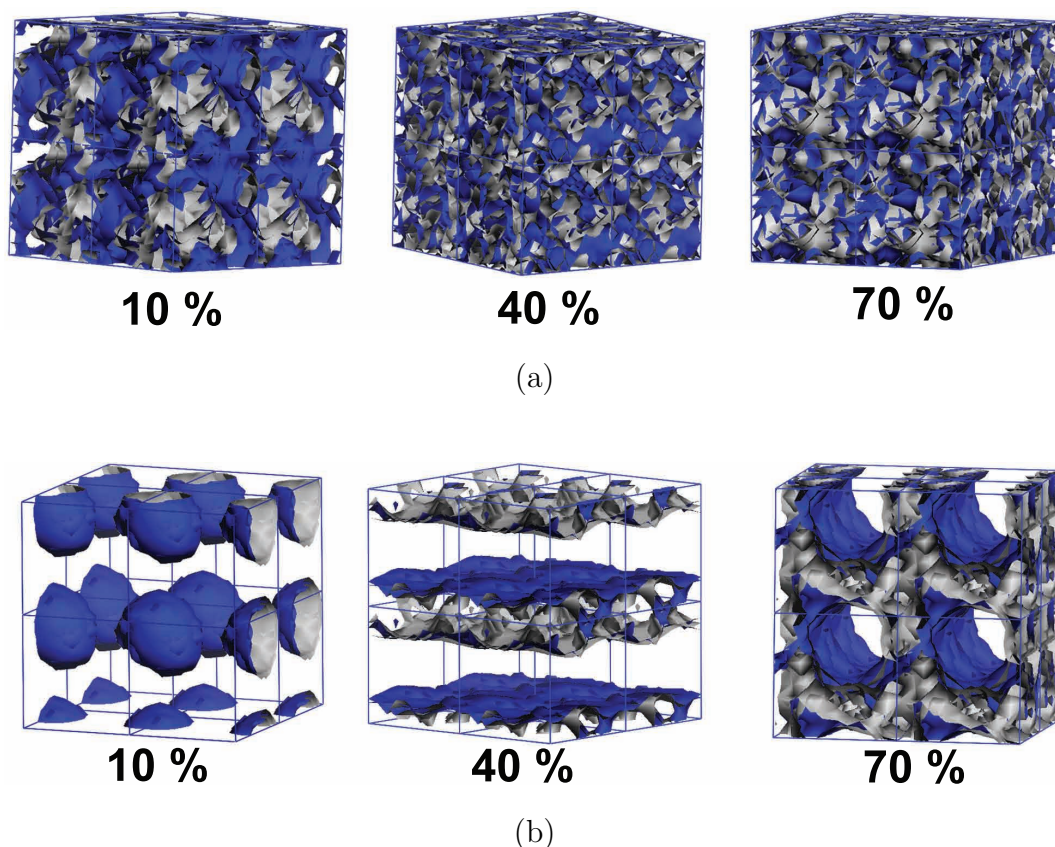


Figure 3.16: Mesoscopic morphologies of the copolymer at various concentrations in (a) THF, and (b) DMF.

solvent is preserved even at low concentrations of the solvent. This *homogenous drying* yields a smooth surface on the droplets, although the semi flexible skin may collapse in the course of solvent diffusion from the core.

The nanoscopically rough topography shown in Fig. 3.17(c) implies that the droplets disintegrated from the electrically driven jet cannot dry homogeneously. A number of studies report the formation of micron size beads by electrospaying of various polymers, including polystyrene, from DMF solutions [67,68]. Therefore, formation of a skin layer on the surface of the droplets is normally possible at the electrospaying process conditions indicated for the production of the surfaces in Fig. 3.17 although the boiling point of DMF is relatively high. On the other hand, there is no sign of a skin formation and the topography consists of mostly non-hierarchical nanoscale features in the Fig. 3.17(c). The 0.15 wt% DMF solution might be in a dilute regime, accompanied by a

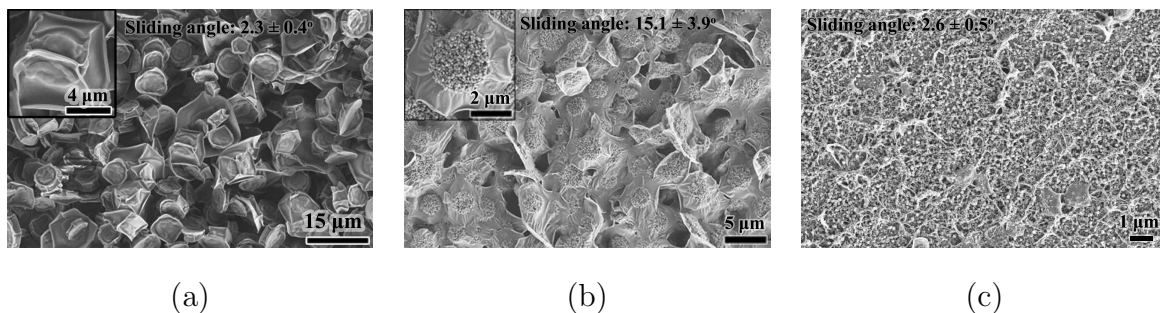


Figure 3.17: Typical SEM images of the electrospayed copolymer from (a) 1 wt% solution in THF (the surface shown in Fig. 3.1(b)), (b) 1 wt% solution in 75/25 (wt/wt) THF/DMF mixture (electrospayed at 8 kV and 2  $\mu\text{L}/\text{min}$ , the surface shown in Fig. 3.4(a)), and (c) 0.15 wt% solution in DMF.

phase separation as implied in Fig. 3.16(b), thus an efficient entanglement that occurs homogeneously all along the droplet surface cannot realize. Accordingly, the polymer chains start to segregate when the concentration exceeds the solubility limit upon evaporation of the solvent in the vicinity of droplet disintegration from the charged jet. The effective phase separation of the polymer in DMF at low concentrations demonstrated by DPD simulations inspired us to perform dynamic light scattering measurements in order to understand the hydrodynamic behavior of the real chains in the solvents. DLS measurements must be performed with dilute solutions in order to prevent multiple scattering from the particles. Accordingly, 0.02 wt% solutions of the polymer were prepared in the corresponding solvent systems. Fig. 3.18 shows the results of the analysis in THF, 50/50 THF/DMF, DMF and DMF after filtering the sample with a filter having 200 nm pore size. DLS of the polymer from THF and the binary solvent system revealed single peaks at around 10 nm hydrodynamic radius that refer to the radius of gyration of the unentangled polymer chains. The peak which belong to the sample in binary solvent system is slightly smaller than the one of THF solution. These results show that the combined effect of the binary solution is a lower quality solvent for the polymer compared to THF. Accordingly, the polymer coils contract and yield a slightly smaller hydrodynamic radius, as expected. DLS of the polymer in DMF, on the other hand, resulted particles having 265 nm radius on the average. Absence of a peak which would refer to radius of gyration of the unentangled chains was surprising. However, knowing

the fact that scattering intensity has a strong dependence on particle size (proportional to the sixth power of diameter), an additional DLS measurement was performed with the polymer in DMF after passing the solution from a filter having 200 nm diameter pores. This process provided the observation of the peak that belongs to the single chains at an average radius of 12.18 nm. Interestingly, the peak around 265 nm radius was still observable although with a considerable amount of decrease in the intensity. The summary of the overall results reveal that apparently, when the solid polymer is added into DMF, an efficient dissolution of the entangled chains cannot realize due to the preference of polymer-polymer self-interactions. The high DPD interaction values between beads A-S<sub>2</sub> and D-S<sub>2</sub> support this claim well. However, the question is how the 530 nm sized particles passed through 200 nm pores? One of the explanations of this observation might be that these particles are soft segregates which are able to squeeze into a smaller volume under pressure during the filtering process and relax to their thermodynamic shape afterwards. DMF is not a non-solvent for the polymer; therefore, a level of interaction must exist between the chains and the solvent although very weak. Accordingly, the poor solvent DMF might be providing a plasticizing effect for chain movement. Another answer might be that either disentangled or not, these particles break down under the high shear while passing through the filter pores, and their integrated shape is restored upon disappearance of the shear forces. In either case, the final shape, grouping or segregation of the chains are thermodynamically stabilized due to exposure of much less chains towards the solvent. On the other hand, for instance, experiments with methanol, a non-solvent for the polymer ( $\delta = 16.73$ ), resulted direct phase separation and precipitation of the polymer at 0.02 wt% concentration. Forcing the system to disentanglement by applying ultrasonication and heat (50 °C) could not prevent precipitation which disallowed DLS measurements. However, by filtering the dispersion with the 200 nm filter, we could perform DLS analysis and achieved the results shown in Fig. 3.19 where particles having 82 nm average hydrodynamic radius were observed. This result indicates that the segregated chains are hard particles in the non-solvent due to the inability of methanol molecules to diffuse into entangled polymer chains. Accordingly, neither the particles having diameter bigger than 200 nm can pass

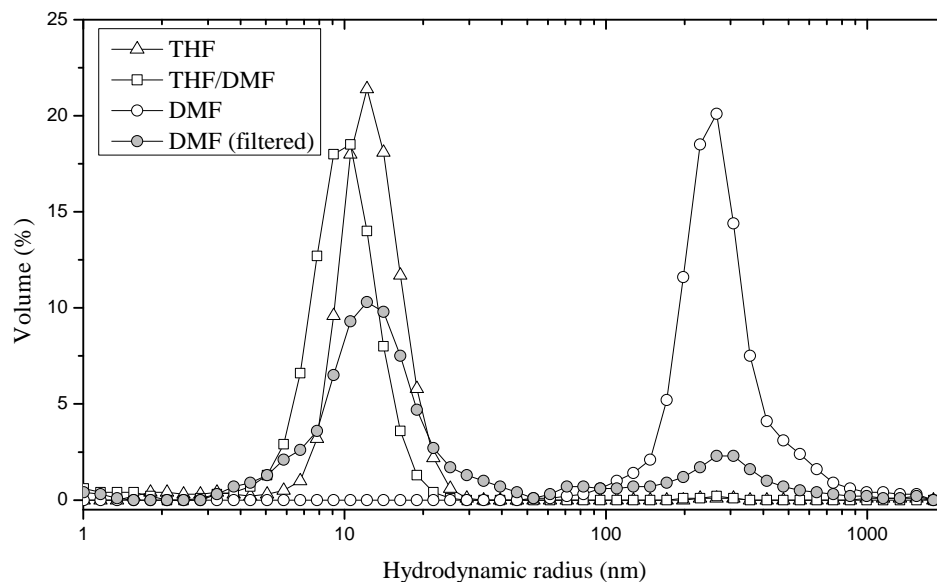


Figure 3.18: DLS analysis 0.02 wt% polymer in THF, DMF, DMF after passing the solution from a filter having 200 nm diameter pores, and THF/DMF 50/50.

through the pores, nor the individual chains are able to escape from the entangled state as implied by the absence of a peak that would refer to the radius of gyration of the chains.

DLS analysis showed that the binary solvent system is efficient to separate the entangled chains of the solid polymer. The difference in the boiling points of these solvents leads to fast evaporation of THF from the electrosprayed beads and entrapment of DMF in the core of the particles. Accordingly, we investigated the hydrodynamics of this process by allowing THF to evaporate from the solution (at room temperature and atmospheric pressures) leaving a predominantly DMF environment for the chains. The starting concentration was halved so that the final concentration after THF removal would be same with the DMF solution shown in Fig. 3.18 (i.e. 0.02 wt%). It was observed that the transparent solution adopts opaque character as THF evaporates with time. DLS analysis of this sample revealed about 553 nm radius particles in the solvent (Fig. 3.19). Stirring, heating or/and sonicating this dispersion did not change the results. In addition, no peaks were observed in the DLS analysis of this sample after filtration. Obviously, the hydrodynamics of mixing the solid polymer directly

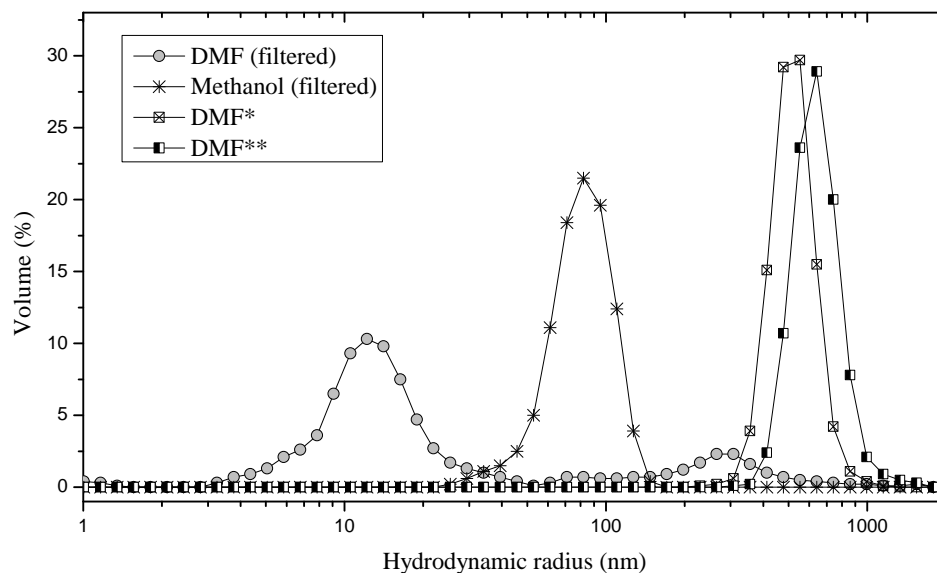


Figure 3.19: DLS analysis 0.02 wt% polymer in DMF after passing the solution from a filter having 200 nm diameter pores, methanol, DMF after evaporation of THF from THF/DMF 50/50 (DMF\*), and 0.04 wt% in DMF after evaporation of THF from THF/DMF (DMF\*\*).

with DMF and achieving a DMF dispersion through evaporation of THF from the binary solvent system are different. In the latter, polymer chains are forced to collapse from an expanded state which must lead to more complex, bigger segregates.

## Chapter 4

### Summary and Conclusions

To summarize, perfect hydrophobicity has been successfully achieved through dual scale roughness by polymer phase separation during electrospinning in good solvent-poor solvent mixtures. Surface morphologies were strongly affected by the solution and process parameters in electrospinning. Understanding of the bead formation mechanism provided us to control the parameters to achieve desired topographies. Use of good solvents led to formation of micron scale roughness, whereas incorporation of poor solvent into the solutions resulted nanoscale features on the micron scale beads due to phase separation of the polymer drying from the high boiling point poor solvent. High applied voltages and solution feed rates retarded the formation of skin layer on the bead surfaces due to insufficient time for drying on the way to the collecting screen, and surfaces having predominantly nanoscale roughness resulted through diminishing of bead shapes. Finally, when the coating time was kept short so that nanoscale rough beads accumulated as micron scale hills and were separated by valleys of uncoated regions, zero contact angle hysteresis realized. Force measurements between the droplets and surfaces showed that these dual scale rough surfaces have  $180^\circ$  receding angles, thus they were perfectly hydrophobic.

The method introduced in this thesis might be important from several aspects. As a whole, it comprises the fundamentals of polymer physics, solution processing (dry spinning) of polymers and wettability together to achieve perfectly hydrophobic polymer surfaces in a facile and versatile way. The surface topographies introduced by the corresponding method are unique in the electrospinning literature. Relationship between

electrospraying (solution and process) parameters and final bead structures would bring new perspective to the understanding of various bead morphology and topographies. In addition, the results are in good accordance with the current understanding of the wetting phenomena, and particularly support the explanations of the effect of different roughness scales on contact angle hysteresis and receding angles in terms of three phase contact line structures.

The conclusion of both DPD and DLS analysis is that there is no effective preference for the interaction between the solvent and the polymer as a whole in THF, but polymer-polymer interactions are favored in the poor solvent DMF. This result explains the structural evolution of the dual scale topographies. Fast evaporation of THF from the surface of droplets leads to the formation of a skin layer, while the high boiling point DMF is trapped in the core. This leads to a phase separation of the polymer, which in turn leads to the formation of nanoscopic roughness from the individual aggregates in the middle of the beads while the trapped solvent diffuses to the surface and evaporate.

A simulation that represents the hydrodynamics of the drying process well must indeed start from a semidilute unentangled region. In addition, DLS measurements at a region where chains are in a dilute regime would not give exact information about the hydrodynamics of the chains in the corresponding solvents during electrospraying (0.15 and 0.02 wt% concentrations of the polymer in DMF for electrospraying and DLS analysis, respectively, are in fact comparable). On the other hand, the scope of this study was not to find a method which would demonstrate the the hydrodynamics of morphology formation in electrospraying, but to gain fundamental information that would allow to elucidate the corresponding experimental results from a physical point of view. In this sense, we believe both DPD simulations and DLS analysis have yielded very useful data.



# Appendix A

## Appendix

### **A.1 Contact and Release Experiments Performed with Other Surfaces**

Selected frames of the contact and release experiments performed with surfaces electrospayed from 1 and 7 wt% copolymer in THF are shown in Fig. A.1 and Fig. A.2. Selected frames of the contact and release experiments performed with surfaces electrospayed from the binary 75/25 (wt/wt) THF/DMF solvent using 8 kV applied voltage and 2  $\mu\text{L}/\text{min}$  solution feed rate is shown in Fig. A.3.

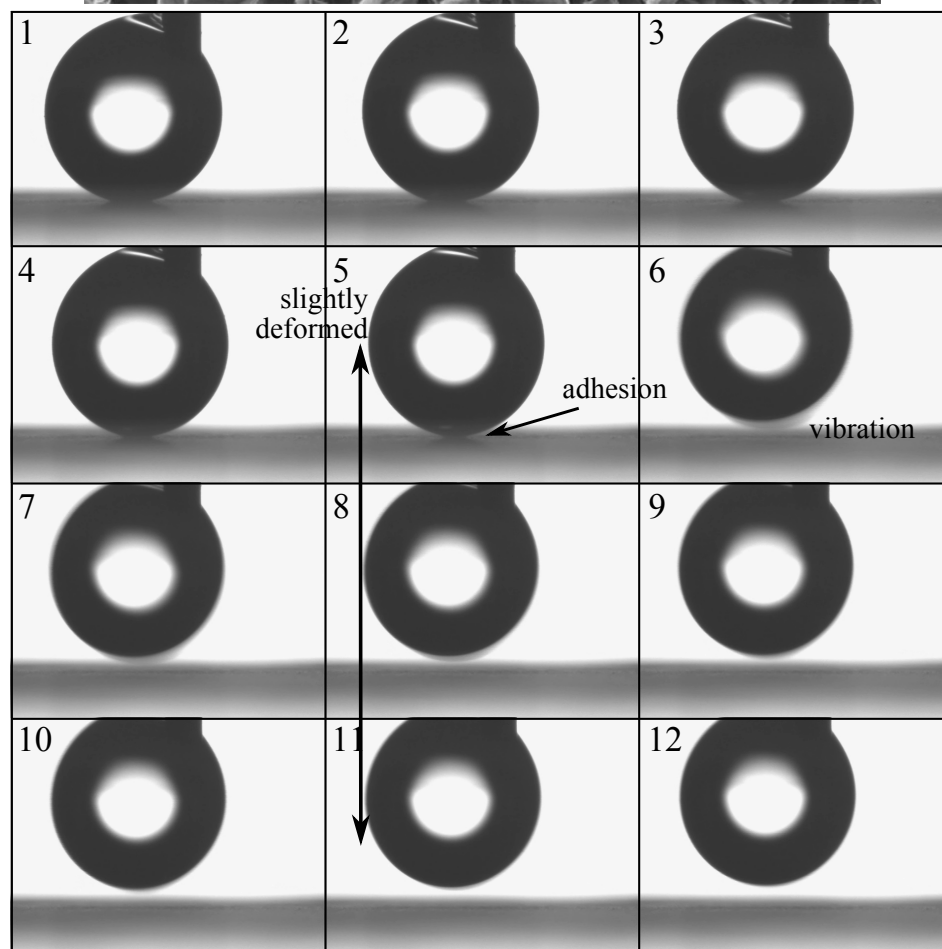
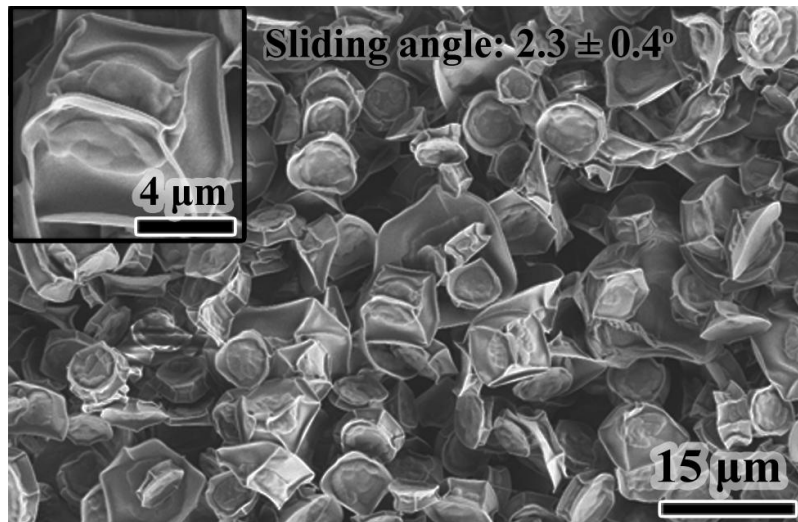


Figure A.1: Selected frames of the contact and release experiment performed with the surface electrospayed from 1 wt% copolymer in THF. The SEM micrograph is the replication of Fig. 3.1(b).

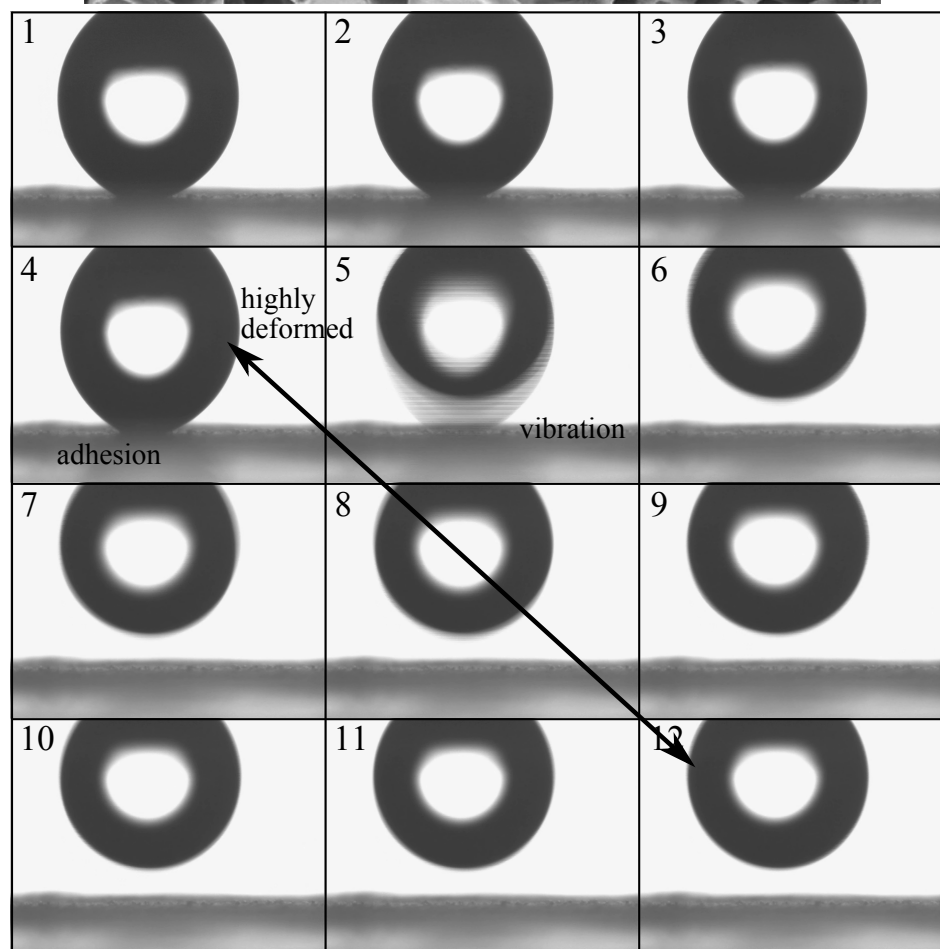
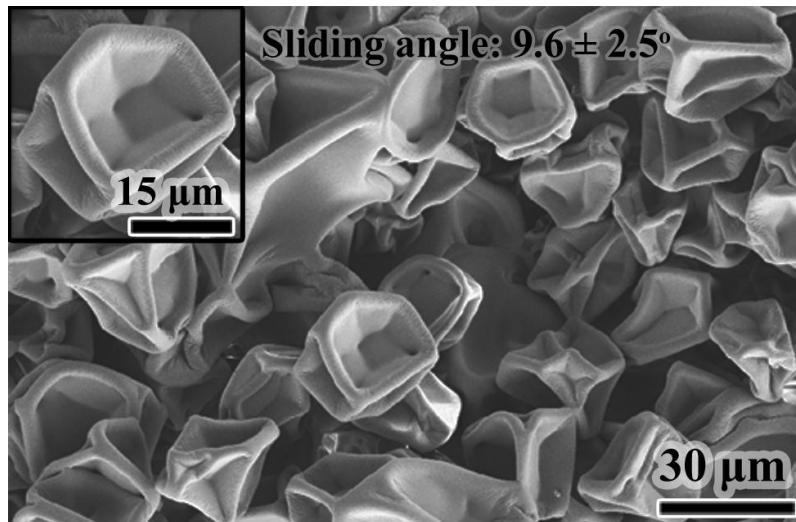


Figure A.2: Selected frames of the contact and release experiment performed with the surface electrospayed from 1 wt% copolymer in THF. The SEM micrograph is the replication of Fig. 3.1(a).

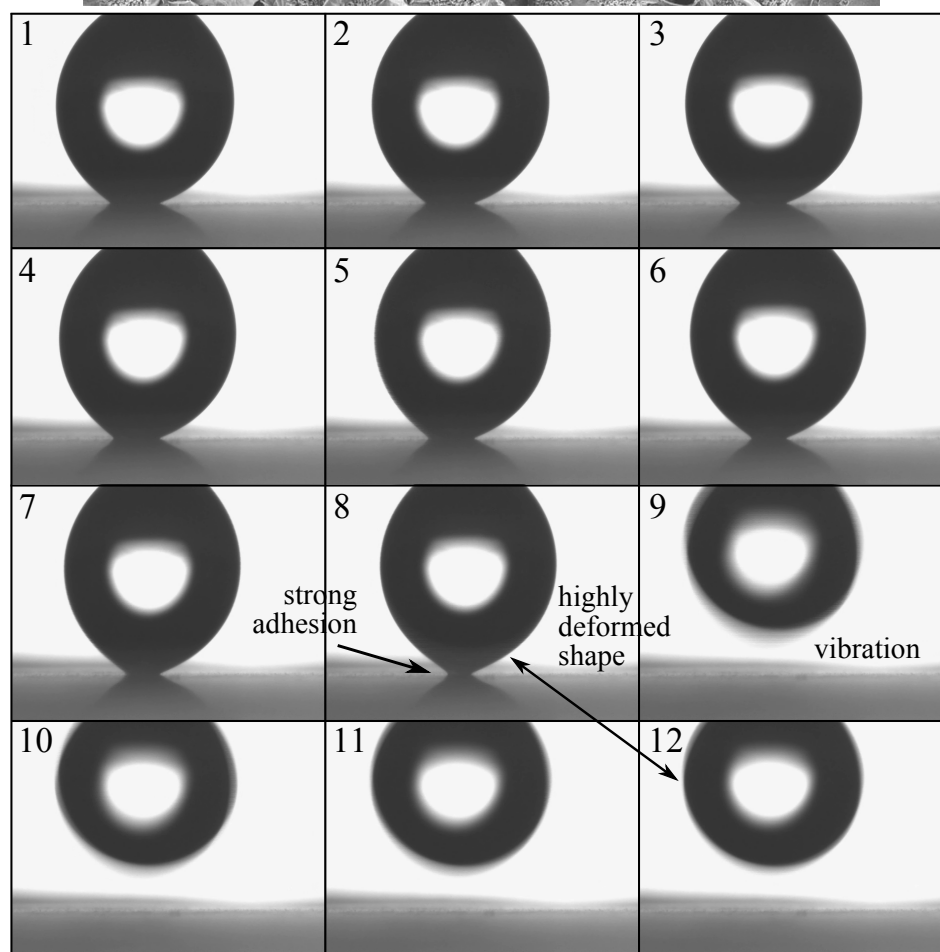
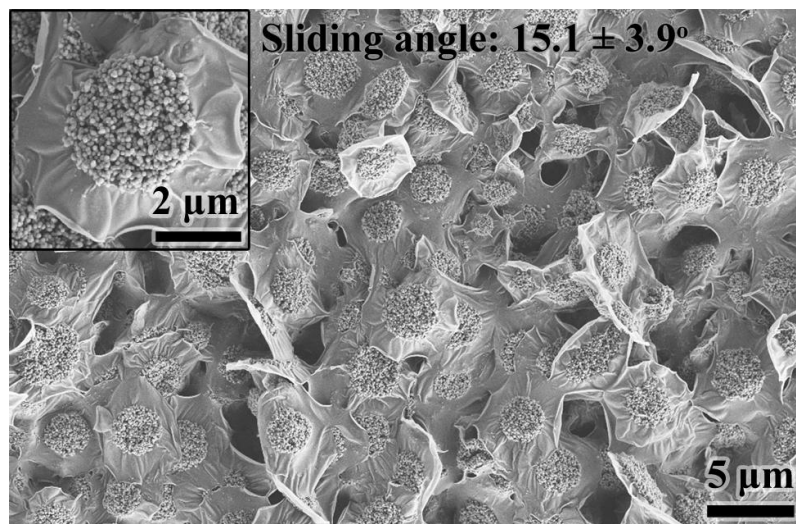


Figure A.3: Selected frames of the contact and release experiment performed with the surface electrospayed from 1 wt% copolymer in 75/25 (w/w) THF/DMF at 8 kV applied voltage and 2  $\mu\text{L}/\text{min}$  solution feed rate. The SEM micrograph is the replication of Fig. 3.4(a).

## A.2 Examples of Surfaces from Other Polymers or Systems

This section comprises SEM micrographs and wettability measurement results of example surfaces:

- Fig. A.4: Electrospaying the poly(st-co-PFA) used in this work at higher concentration, applied voltage and solution feed rate than those shown in Fig. 3.4(b) and (c), and achievement of a perfectly hydrophobic surface by coating the substrate partially.
- Fig. A.5: A surface similar to the one shown in Fig. 3.4(a), achieved by electrospaying a copolymer of methyl methacrylate (MMA) and perfluoroalkyl ethylacrylate (5 mol% in the chain) in 50/50 (wt/wt) THF/DMF solution at 8 kV applied voltage and 2  $\mu\text{L}/\text{min}$  solution feed rate.
- Fig. A.6: A perfectly hydrophobic surface from a partial coating of electrospayed 2 wt% poly(MMA-co-PFA) 50/50 (wt/wt) THF/DMF solution at 15 kV applied voltage and 15  $\mu\text{L}/\text{min}$  solution feed rate.
- Fig. A.7: A surface achieved by electrospaying the poly(st-co-PFA) from 1.5 wt% solution in 50/50 (wt/wt) THF/*N*-methyl-2-pyrrolidone binary solvent.

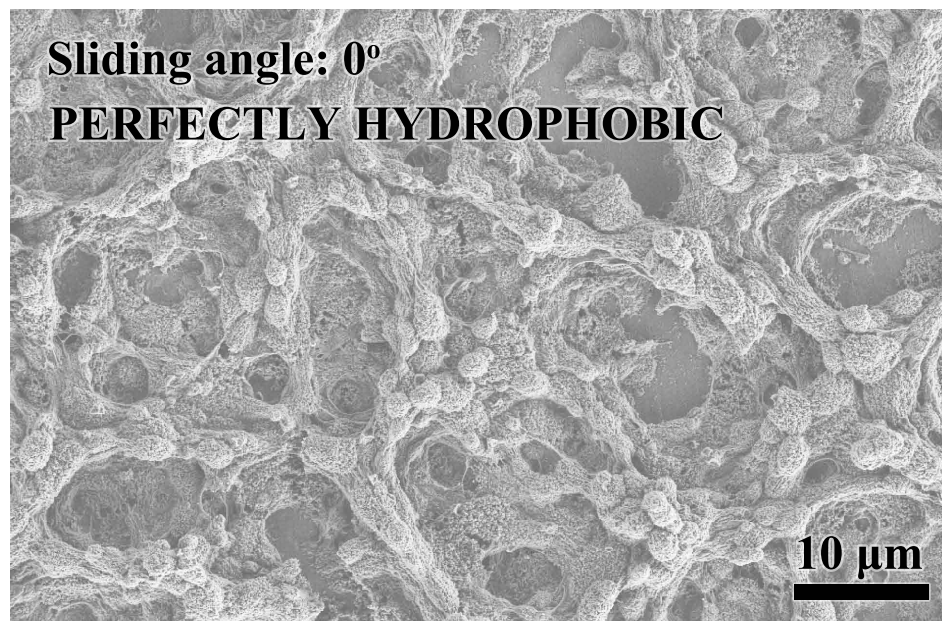


Figure A.4: Typical SEM image of the electrospayed surfaces from 2 wt% poly(st-co-PFA) solutions in 75/25 (wt/wt) THF/DMF mixture (22 kV applied voltage and 25  $\mu\text{L}/\text{min}$  solution feed rate).

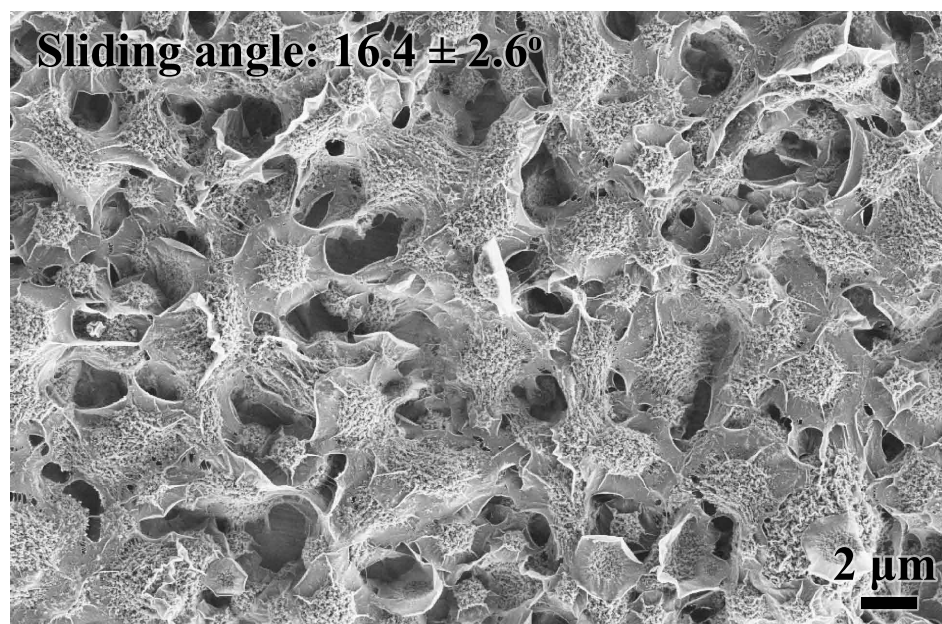


Figure A.5: Typical SEM image of the electrospayed surfaces from 2 wt% poly(MMA-co-PFA) solutions in 50/50 (wt/wt) THF/DMF mixture (8 kV applied voltage and 2  $\mu\text{L}/\text{min}$  solution feed rate).

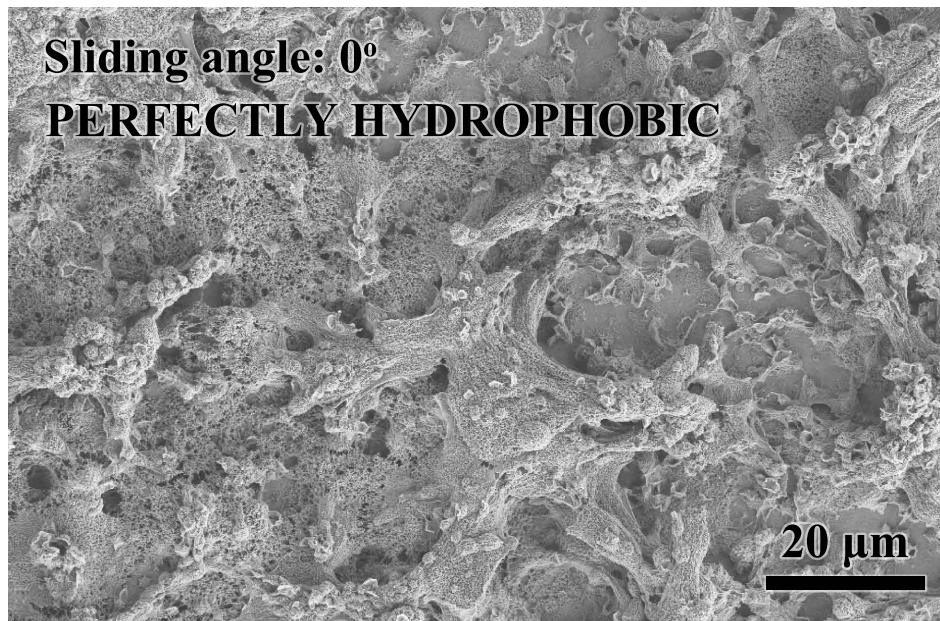


Figure A.6: Typical SEM image of the electrospayed surfaces from 2 wt% poly(MMA-*co*-PFA) solutions in 50/50 (wt/wt) THF/DMF mixture (15 kV applied voltage and 15  $\mu\text{L}/\text{min}$  solution feed rate).



Figure A.7: Typical SEM image of the electrospayed surfaces from 1.5 wt% poly(st-*co*-PFA) solutions in 50/50 (wt/wt) THF/NMP mixture (8 kV applied voltage and 0.5  $\mu\text{L}/\text{min}$  solution feed rate).

# Bibliography

- [1] W. Norde, *Colloids and Interfaces in Life Sciences*. CRC Press, 2003.
- [2] T. Young, “An essay on the cohesion of fluids,” *Philosophical Transactions of the Royal Society of London*, vol. 95, pp. 65–87, 1805.
- [3] K. T. Powell, C. Cheng, K. L. Wooley, A. Singh, and M. W. Urban, “Complex amphiphilic networks derived from diamine-terminated poly(ethylene glycol) and benzylic chloride-functionalized hyperbranched fluoropolymers,” *Journal of Polymer Science Part A: Polymer Chemistry*, vol. 44, pp. 4782–4794, 2006.
- [4] G. D. Fu, E. T. Kang, and K. G. Neoh, “Three-dimensionally ordered porous membranes prepared via self-assembly and reverse micelle formation from well-defined amphiphilic block copolymers,” *Langmuir*, vol. 21, pp. 3619–3624, 2005.
- [5] T. L. Bucholz and Y.-L. Loo, “Phase behavior of near-monodisperse semifluorinated diblock copolymers by atom transfer radical polymerization,” *Macromolecules*, vol. 39, pp. 6075–6080, 2006.
- [6] K. T. Powell, C. Cheng, and K. L. Wooley, “Complex amphiphilic hyperbranched fluoropolymers by atom transfer radical self-condensing vinyl (co)polymerization,” *Macromolecules*, vol. 40, pp. 4509–4515, 2007.
- [7] P. Graham, M. Stone, A. Thorpe, T. G. Nevell, and J. Tsibouklis, “Fluoropolymers with very low surface energy characteristics,” *Journal of Fluorine Chemistry*, vol. 104, pp. 29–36, 2000.



- [8] R. D. V. de Grampel, W. Ming, A. Gildenpfennig, W. J. H. van Gennip, J. Laven, J. W. Niemantsverdriet, H. H. Brongersma, G. de With, and R. van der Linde, "The outermost atomic layer of thin films of fluorinated polymethacrylates," *Langmuir*, vol. 20, pp. 6344–6351, 2004.
- [9] T. Hayakawa, J. G. Wang, M. L. Xiang, X. F. Li, M. Ueda, C. K. Ober, J. Genzer, E. Sivaniah, E. J. Kramer, and D. A. Fischer, "Effect of changing molecular end groups on surface properties: Synthesis and characterization of poly(styrene-*b*-semifluorinated isoprene) block copolymers with  $-CF_2H$  end groups," *Macromolecules*, vol. 33, pp. 8012–8019, 2000.
- [10] T. Nishino, Y. Urushihara, M. Meguro, and K. Nakamae, "Surface properties and structures of diblock and random copolymers with perfluoroalkyl side chains," *Journal of Colloid and Interface Science*, vol. 279, pp. 364–369, 2004.
- [11] I. J. Park, S. B. Lee, and C. K. Choi, "Surface properties of the fluorine-containing graft copolymer of poly((perfluoroalkyl)ethyl methacrylate)-*g*-poly(methyl methacrylate)," *Macromolecules*, vol. 31, pp. 7555–7558, 1998.
- [12] S. Saidi, F. Guittard, C. Guimon, and S. Geribaldi, "Low surface energy perfluorooctylalkyl acrylate copolymers for surface modification of PET," *Macromolecular Chemistry and Physics*, vol. 206, pp. 1098–1105, 2005.
- [13] S. Saidi, F. Guittard, C. Guimon, and S. Geribaldi, "Fluorinated acrylic polymers: Surface properties and XPS investigations," *Journal of Applied Polymer Science*, vol. 99, pp. 821–827, 2006.
- [14] J. Tsibouklis, M. Stone, A. A. Thorpe, P. Graham, T. G. Nevell, and R. J. Ewen, "Surface energy characteristics of polymer film structures: A further insight into the molecular design requirements," *Langmuir*, vol. 15, pp. 7076–7079, 1999.
- [15] J. Tsibouklis, P. Graham, P. J. Eaton, J. R. Smith, T. G. Nevell, J. D. Smart, and R. J. Ewen, "Poly(perfluoroalkyl methacrylate) film structures: Surface or-

- ganization phenomena, surface energy determinations, and force of adhesion measurements,” *Macromolecules*, vol. 33, pp. 8460–8465, 2000.
- [16] J. Tsibouklis and T. G. Nevell, “Ultra-low surface energy polymers: The molecular design requirements,” *Advanced Materials*, vol. 15, pp. 647–650, 2003.
- [17] J. Wang and C. K. Ober, “Self-organizing materials with low surface energy: The synthesis and solid-state properties of semifluorinated side-chain ionenes,” *Macromolecules*, vol. 30, pp. 7560–7567, 1997.
- [18] J. G. Wang, G. P. Mao, C. K. Ober, and E. J. Kramer, “Liquid crystalline, semifluorinated side group block copolymers with stable low energy surfaces: Synthesis, liquid crystalline structure, and critical surface tension,” *Macromolecules*, vol. 30, pp. 1906–1914, 1997.
- [19] R. H. Dettre and R. E. Johnson Jr., “Surface properties of polymers: I. The surface tensions of some molten polyethylenes,” *Journal of Colloid and Interface Science*, vol. 21, pp. 367 – 377, 1966.
- [20] R. H. Dettre and R. E. Johnson Jr., “Surface tensions of perfluoroalkanes and polytetrafluoroethylene,” *Journal of Colloid and Interface Science*, vol. 31, pp. 568 – 569, 1969.
- [21] X. F. Li, L. Andruzzi, E. Chiellini, G. Galli, C. K. Ober, A. Hexemer, E. J. Kramer, and D. A. Fischer, “Semifluorinated aromatic side-group polystyrene-based block copolymers: Bulk structure and surface orientation studies,” *Macromolecules*, vol. 35, pp. 8078–8087, 2002.
- [22] J. Genzer, E. Sivaniah, E. J. Kramer, J. G. Wang, H. Korner, M. L. Xiang, K. Char, C. K. Ober, B. M. DeKoven, R. A. Bubeck, M. K. Chaudhury, S. Sambasivan, and D. A. Fischer, “The orientation of semifluorinated alkanes attached to polymers at the surface of polymer films,” *Macromolecules*, vol. 33, pp. 1882–1887, 2000.

- [23] L. Gao and T. J. McCarthy, “An attempt to correct the faulty intuition perpetuated by the Wenzel and Cassie “laws”,” *Langmuir*, vol. 25, pp. 7249–7255, 2009.
- [24] R. N. Wenzel, “Resistance of solid surfaces to wetting by water,” *Industrial & Engineering Chemistry*, vol. 28, pp. 988–994, 1936.
- [25] A. B. D. Cassie and S. Baxter, “Wettability of porous surfaces,” *Transactions of the Faraday Society*, vol. 40, pp. 546–551, 1944.
- [26] A. Lafuma and D. Quere, “Superhydrophobic states,” *Nature Materials*, vol. 2, pp. 457–460, 2003.
- [27] C. Ishino, K. Okumura, and D. Quere, “Wetting transitions on rough surfaces,” *Europhysics Letters*, vol. 68, pp. 419–425, 2004.
- [28] L. C. Gao and T. J. McCarthy, “How Wenzel and Cassie were wrong,” *Langmuir*, vol. 23, pp. 3762–3765, 2007.
- [29] W. Chen, A. Y. Fadeev, M. C. Hsieh, D. Oner, J. Youngblood, and T. J. McCarthy, “Ultrahydrophobic and ultralyophobic surfaces: Some comments and examples,” *Langmuir*, vol. 15, pp. 3395–3399, 1999.
- [30] J. P. Youngblood and T. J. McCarthy, “Ultrahydrophobic polymer surfaces prepared by simultaneous ablation of polypropylene and sputtering of poly(tetrafluoroethylene) using radio frequency plasma,” *Macromolecules*, vol. 32, pp. 6800–6806, 1999.
- [31] D. Oner and T. J. McCarthy, “Ultrahydrophobic surfaces. Effects of topography length scales on wettability,” *Langmuir*, vol. 16, pp. 7777–7782, 2000.
- [32] L. C. Gao and T. J. McCarthy, “Contact angle hysteresis explained,” *Langmuir*, vol. 22, pp. 6234–6237, 2006.

- [33] C. G. L. Furnidge, “Studies at phase interfaces. I. The sliding of liquid drops on solid surfaces and a theory for spray retention,” *Journal of Colloid Science*, vol. 17, pp. 309–324, 1962.
- [34] R. Truesdell, A. Mammoli, P. Vorobieff, F. van Swol, and C. J. Brinker, “Drag reduction on a patterned superhydrophobic surface,” *Physical Review Letters*, vol. 97, p. 044504, 2006.
- [35] J. Ou, B. Perot, and J. P. Rothstein, “Laminar drag reduction in microchannels using ultrahydrophobic surfaces,” *Physics of Fluids*, vol. 16, pp. 4635–4643, 2004.
- [36] C. Lee, C.-H. Choi, and C.-J. C. Kim, “Structured surfaces for a giant liquid slip,” *Physical Review Letters*, vol. 101, p. 064501, 2008.
- [37] R. N. Govardhan, G. S. Srinivas, A. Asthana, and M. S. Bobji, “Time dependence of effective slip on textured hydrophobic surfaces,” *Physics of Fluids*, vol. 21, p. 052001, 2009.
- [38] J. P. Rothstein, “Slip on superhydrophobic surfaces,” *Annual Review of Fluid Mechanics*, vol. 42, pp. 89–109, 2010.
- [39] R. S. Voronov, D. V. Papavassiliou, and L. L. Lee, “Review of fluid slip over superhydrophobic surfaces and its dependence on the contact angle,” *Industrial & Engineering Chemistry Research*, vol. 47, pp. 2455–2477, 2008.
- [40] C. Choi and C. Kim, “Large slip of aqueous liquid flow over a nanoengineered superhydrophobic surface,” *Physical Review Letters*, vol. 96, 2006.
- [41] W. Barthlott and C. Neinhuis, “Purity of the sacred lotus, or escape from contamination in biological surfaces,” *Planta*, vol. 202, pp. 1–8, 1997.
- [42] L. C. Gao and T. J. McCarthy, “The “Lotus effect” explained: Two reasons why two length scales of topography are important,” *Langmuir*, vol. 22, pp. 2966–2967, 2006.

- [43] L. Gao and T. J. McCarthy, “Teflon is hydrophilic. Comments on definitions of hydrophobic, shear versus tensile hydrophobicity, and wettability characterization,” *Langmuir*, vol. 24, pp. 9183–9188, 2008.
- [44] L. Gao and T. J. McCarthy, “A perfectly hydrophobic surface ( $\theta_a/\theta_r=180^\circ/180^\circ$ ),” *Journal of the American Chemical Society*, vol. 128, pp. 9052–9053, 2006.
- [45] L. Gao and T. J. McCarthy, “A commercially available perfectly hydrophobic material ( $\theta_a/\theta_r=180^\circ/180^\circ$ ),” *Langmuir*, vol. 23, pp. 9125–9127, 2007.
- [46] S.-G. Park, S. Y. Lee, S. G. Jang, and S.-M. Yang, “Perfectly hydrophobic surfaces with patterned nanoneedles of controllable features,” *Langmuir*, vol. 26, pp. 5295–5299, 2010.
- [47] J. Doshi and D. H. Reneker, “Electrospinning process and applications of electrospun fibers,” *Journal of Electrostatics*, vol. 35, pp. 151–160, 1995.
- [48] D. H. Reneker and I. Chun, “Nanometre diameter fibres of polymer, produced by electrospinning,” *Nanotechnology*, vol. 7, p. 216, 1996.
- [49] Z.-M. Huang, Y.-Z. Zhang, M. Kotaki, and S. Ramakrishna, “A review on polymer nanofibers by electrospinning and their applications in nanocomposites,” *Composites Science and Technology*, vol. 63, pp. 2223–2253, 2003.
- [50] D. Han and A. J. Steckl, “Superhydrophobic and oleophobic fibers by coaxial electrospinning,” *Langmuir*, vol. 25, pp. 9454–9462, 2009.
- [51] J. Zheng, A. He, J. Li, J. Xu, and C. C. Han, “Studies on the controlled morphology and wettability of polystyrene surfaces by electrospinning or electrospraying,” *Polymer*, vol. 47, pp. 7095–7102, 2006.
- [52] A. Singh, L. Steely, and H. R. Allcock, “Poly[bis(2,2,2-trifluoroethoxy)phosphazene] superhydrophobic nanofibers,” *Langmuir*, vol. 21, pp. 11 604–11 607, 2005.

- [53] T. Ogawa, B. Ding, Y. Sone, and S. Shiratori, "Super-hydrophobic surfaces of layer-by-layer structured film-coated electrospun nanofibrous membranes," *Nanotechnology*, vol. 18, p. 165607, 2007.
- [54] Y. Miyauchi, B. Ding, and S. Shiratori, "Fabrication of a silver-ragwort-leaf-like super-hydrophobic micro/nanoporous fibrous mat surface by electrospinning," *Nanotechnology*, vol. 17, p. 5151, 2006.
- [55] M. Ma, Y. Mao, M. Gupta, K. K. Gleason, and G. C. Rutledge, "Superhydrophobic fabrics produced by electrospinning and chemical vapor deposition," *Macromolecules*, vol. 38, pp. 9742–9748, 2005.
- [56] M. Ma, R. M. Hill, and G. C. Rutledge, "A review of recent results on superhydrophobic materials based on micro- and nanofibers," *Journal of Adhesion Science and Technology*, vol. 22, pp. 1799–1817, 2008.
- [57] M. Ma, R. M. Hill, J. L. Lowery, S. V. Fridrikh, and G. C. Rutledge, "Electrospun poly(styrene-block-dimethylsiloxane) block copolymer fibers exhibiting superhydrophobicity," *Langmuir*, vol. 21, pp. 5549–5554, 2005.
- [58] M. Ma, M. Gupta, Z. Li, L. Zhai, K. Gleason, R. Cohen, M. Rubner, and G. Rutledge, "Decorated electrospun fibers exhibiting superhydrophobicity," *Advanced Materials*, vol. 19, pp. 255–259, 2007.
- [59] X. Lu, J. Zhou, Y. Zhao, Y. Qiu, and J. Li, "Room temperature ionic liquid based polystyrene nanofibers with superhydrophobicity and conductivity produced by electrospinning," *Chemistry of Materials*, vol. 20, pp. 3420–3424, 2008.
- [60] J.-M. Lim, G.-R. Yi, J. H. Moon, C.-J. Heo, and S.-M. Yang, "Superhydrophobic films of electrospun fibers with multiple-scale surface morphology," *Langmuir*, vol. 23, pp. 7981–7989, 2007.
- [61] S. J. Hardman, N. Muhamad-Sarih, H. J. Riggs, R. L. Thompson, J. Rigby, W. N. A. Bergius, and L. R. Hutchings, "Electrospinning superhydrophobic fibers

- using surface segregating end-functionalized polymer additives,” *Macromolecules*, vol. 44, pp. 6461–6470, 2011.
- [62] S. Agarwal, S. Horst, and M. Bognitzki, “Electrospinning of fluorinated polymers: Formation of superhydrophobic surfaces,” *Macromolecular Materials and Engineering*, vol. 291, pp. 592–601, 2006.
- [63] P. Gupta, C. Elkins, T. E. Long, and G. L. Wilkes, “Electrospinning of linear homopolymers of poly(methyl methacrylate): Exploring relationships between fiber formation, viscosity, molecular weight and concentration in a good solvent,” *Polymer*, vol. 46, pp. 4799–4810, 2005.
- [64] S. L. Shenoy, W. D. Bates, H. L. Frisch, and G. E. Wnek, “Role of chain entanglements on fiber formation during electrospinning of polymer solutions: Good solvent, non-specific polymer-polymer interaction limit,” *Polymer*, vol. 46, pp. 3372–3384, 2005.
- [65] H. Fong, I. Chun, and D. Reneker, “Beaded nanofibers formed during electrospinning,” *Polymer*, vol. 40, pp. 4585–4592, 1999.
- [66] A. M. Ganan-Calvo, “The surface charge in electrospraying: Its nature and its universal scaling laws,” *Journal of Aerosol Science*, vol. 30, pp. 863–872, 1999.
- [67] G. Eda and S. Shivkumar, “Bead structure variations during electrospinning of polystyrene,” *Journal of Materials Science*, vol. 41, pp. 5704–5708, 2006.
- [68] D. Fantini, M. Zanetti, and L. Costa, “Polystyrene microspheres and nanospheres produced by electrospray,” *Macromolecular Rapid Communications*, vol. 27, pp. 2038–2042, 2006.
- [69] J. Liu and S. Kumar, “Microscopic polymer cups by electrospinning,” *Polymer*, vol. 46, pp. 3211–3214, 2005.
- [70] J. Liu, A. Rasheed, H. Dong, W. W. Carr, M. D. Dadmun, and S. Kumar, “Electrospun micro- and nanostructured polymer particles,” *Macromolecular Chemistry and Physics*, vol. 209, pp. 2390–2398, 2008.

- [71] C. H. Park and J. Lee, “Electrosprayed polymer particles: Effect of the solvent properties,” *Journal of Applied Polymer Science*, vol. 114, pp. 430–437, 2009.
- [72] H. Wang, Q. Liu, Q. Yang, Y. Li, W. Wang, L. Sun, C. Zhang, and Y. Li, “Electrospun poly(methyl methacrylate) nanofibers and microparticles,” *Journal of Materials Science*, vol. 45, pp. 1032–1038, 2010.
- [73] K. Lee, H. Kim, H. Bang, Y. Jung, and S. Lee, “The change of bead morphology formed on electrospun polystyrene fibers,” *Polymer*, vol. 44, pp. 4029–4034, 2003.
- [74] C. Zhong and D. Liu, “Understanding multicompartment micelles using dissipative particle dynamics simulation,” *Macromolecular Theory and Simulations*, vol. 16, pp. 141–157, 2007.
- [75] A. A. Gavrilov, Y. V. Kudryavtsev, P. G. Khalatur, and A. V. Chertovich, “Microphase separation in regular and random copolymer melts by DPD simulations,” *Chemical Physics Letters*, vol. 503, pp. 277 – 282, 2011.
- [76] H. Can, G. Kacar, and C. Atilgan, “Surfactant formation efficiency of fluorocarbon-hydrocarbon oligomers in supercritical CO<sub>2</sub>,” *The Journal of Chemical Physics*, vol. 131, p. 124701, 2009.
- [77] R. D. Groot and T. J. Madden, “Dynamic simulation of diblock copolymer microphase separation,” *The Journal of Chemical Physics*, vol. 108, pp. 8713–8724, 1998.
- [78] H. Sun, G. Xu, Y. Li, and Y. Chen, “Mesoscopic simulation of the aggregation behavior of fluorinated surfactant in aqueous solution,” *Journal of Fluorine Chemistry*, vol. 127, pp. 187 – 192, 2006.
- [79] Y. Kong, C. W. Manke, W. G. Madden, and A. G. Schlijper, “Effect of solvent quality on the conformation and relaxation of polymers via dissipative particle dynamics,” *The Journal of Chemical Physics*, vol. 107, pp. 592–602, 1997.



- [80] Y. Zhang, G. Ji, F. Zhao, Z. Gong, D. Wei, L. Chen, and W. Li, “Mesoscopic simulation of aggregate behaviour of fluoropolymers in the TATB-based PBX,” *Molecular Simulation*, vol. 37, pp. 237–242, 2011.
- [81] D. Wu, S. J. Paddison, J. A. Elliott, and S. J. Hamrock, “Mesoscale modeling of hydrated morphologies of 3m perfluorosulfonic acid-based fuel cell electrolytes,” *Langmuir*, vol. 26, pp. 14 308–14 315, 2010.
- [82] G. Kacar, C. Atilgan, and A. S. Ozen, “Mapping and reverse-mapping of the morphologies for a molecular understanding of the self-assembly of fluorinated block copolymers,” *The Journal of Physical Chemistry C*, vol. 114, pp. 370–382, 2010.
- [83] J. C. Shelley and M. Y. Shelley, “Computer simulation of surfactant solutions,” *Current Opinion in Colloid and Interface Science*, vol. 5, pp. 101 – 110, 2000.
- [84] X. J. Feng and L. Jiang, “Design and creation of superwetting/antiwetting surfaces,” *Advanced Materials*, vol. 18, pp. 3063–3078, 2006.
- [85] X.-M. Li, D. Reinhoudt, and M. Crego-Calama, “What do we need for a superhydrophobic surface? A review on the recent progress in the preparation of superhydrophobic surfaces,” *Chemical Society Reviews*, vol. 36, pp. 1350–1368, 2007.
- [86] J. Genzer and K. Efimenko, “Recent developments in superhydrophobic surfaces and their relevance to marine fouling: A review,” *Biofouling*, vol. 22, pp. 339–360, 2006.
- [87] M. Ma and R. M. Hill, “Superhydrophobic surfaces,” *Current Opinion in Colloid & Interface Science*, vol. 11, pp. 193–202, 2006.
- [88] P. Roach, N. J. Shirtcliffe, and M. I. Newton, “Progress in superhydrophobic surface development,” *Soft Matter*, vol. 4, pp. 224–240, 2008.

- [89] X. Zhang, F. Shi, J. Niu, Y. Jiang, and Z. Wang, "Superhydrophobic surfaces: From structural control to functional application," *Journal of Materials Chemistry*, vol. 18, pp. 621–633, 2008.
- [90] X. Liu, Y. Liang, F. Zhou, and W. Liu, "Extreme wettability and tunable adhesion: Biomimicking beyond nature?" *Soft Matter*, vol. 8, pp. 2070–2086, 2012.
- [91] Y. Y. Yan, N. Gao, and W. Barthlott, "Mimicking natural superhydrophobic surfaces and grasping the wetting process: A review on recent progress in preparing superhydrophobic surfaces," *Advances In Colloid and Interface Science*, vol. 169, pp. 80–105, 2011.
- [92] X. Yao, Y. Song, and L. Jiang, "Applications of bio-inspired special wettable surfaces," *Advanced Materials*, vol. 23, pp. 719–734, 2011.
- [93] Z. Guo, W. Liu, and B.-L. Su, "Superhydrophobic surfaces: From natural to biomimetic to functional," *Journal of Colloid and Interface Science*, vol. 353, pp. 335–355, 2011.
- [94] B. Bhushan and Y. C. Jung, "Natural and biomimetic artificial surfaces for superhydrophobicity, self-cleaning, low adhesion, and drag reduction," *Progress in Materials Science*, vol. 56, pp. 1–108, 2011.
- [95] K. Acatay, E. Simsek, C. Ow-Yang, and Y. Z. Menceloglu, "Tunable, superhydrophobically stable polymeric surfaces by electrospinning," *Angewandte Chemie-International Edition*, vol. 43, pp. 5210–5213, 2004.
- [96] I. Sas, R. E. Gorga, J. A. Joines, and K. A. Thoney, "Literature review on superhydrophobic self-cleaning surfaces produced by electrospinning," *Journal of Polymer Science Part B: Polymer Physics*, vol. 50, pp. 824–845, 2012.
- [97] X. Wang, B. Ding, J. Yu, and M. Wang, "Engineering biomimetic superhydrophobic surfaces of electrospun nanomaterials," *Nano Today*, vol. 6, pp. 510–530, 2011.

- [98] A. W. Neumann and R. J. Good, “Thermodynamics of contact angles. I. Heterogeneous solid surfaces,” *Journal of Colloid and Interface Science*, vol. 38, pp. 341–358, 1972.
- [99] C. Huh and S. Mason, “Effects of surface roughness on wetting (theoretical),” *Journal of Colloid and Interface Science*, vol. 60, pp. 11–38, 1977.
- [100] C. W. Extrand, “Contact angles and their hysteresis as a measure of liquid-solid adhesion,” *Langmuir*, vol. 20, pp. 4017–4021, 2004.
- [101] H. Y. Erbil, A. L. Demirel, Y. Avci, and O. Mert, “Transformation of a simple plastic into a superhydrophobic surface,” *Science*, vol. 299, pp. 1377–1380, 2003.
- [102] Z. Yuan, H. Chen, J. Tang, X. Chen, D. Zhao, and Z. Wang, “Facile method to fabricate stable superhydrophobic polystyrene surface by adding ethanol,” *Surface and Coatings Technology*, vol. 201, pp. 7138–7142, 2007.
- [103] N. Zhao, J. Xu, Q. Xie, L. Weng, X. Guo, X. Zhang, and L. Shi, “Fabrication of biomimetic superhydrophobic coating with a micro-nano-binary structure,” *Macromolecular Rapid Communications*, vol. 26, pp. 1075–1080, 2005.
- [104] X. Lu, C. Zhang, and Y. Han, “Low-density polyethylene superhydrophobic surface by control of its crystallization behavior,” *Macromolecular Rapid Communications*, vol. 25, pp. 1606–1610, 2004.
- [105] Z. Qi, H. Yu, Y. Chen, and M. Zhu, “Highly porous fibers prepared by electrospinning a ternary system of nonsolvent/solvent/poly(L-lactic acid),” *Materials Letters*, vol. 63, pp. 415–418, 2009.
- [106] Y. Yang, A. Centrone, L. Chen, F. Simeon, T. A. Hatton, and G. C. Rutledge, “Highly porous electrospun polyvinylidene fluoride (PVDF)-based carbon fiber,” *Carbon*, vol. 49, pp. 3395–3403, 2011.
- [107] M. Jin, X. Feng, L. Feng, T. Sun, J. Zhai, T. Li, and L. Jiang, “Superhydrophobic aligned polystyrene nanotube films with high adhesive force,” *Advanced Materials*, vol. 17, pp. 1977–1981, 2005.

- [108] M. Jin, X. Feng, J. Xi, J. Zhai, K. Cho, L. Feng, and L. Jiang, “Super-hydrophobic pdms surface with ultra-low adhesive force,” *Macromolecular Rapid Communications*, vol. 26, pp. 1805–1809, 2005.